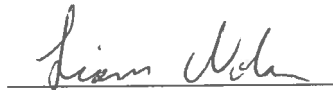# A MICROFLUIDIC MODEL OF PULMONARY AIRWAY REOPENING IN ASYMMETRIC BIFURCATING NETWORKS

AN ABSTRACT

SUBMITTED ON THE FIRST DAY OF MAY 2015

TO THE DEPARTMENT OF BIOMEDICAL ENGINEERING

IN PARTIAL FULLFILLMENT OF THE REQUIREMENTS

OF THE SCHOOL OF SCIENCE AND ENGINEERING

OF TULANE UNIVERSITY

FOR THE DEGREE OF

MASTER OF SCIENCE

BY

Liam P. Nolan

Approved: _____

Donald Gaver, Ph. D.
Director

_____

Bruce Gibb, Ph. D.

_____

Eiichiro Yamaguchi, Ph. D.

Abstract

Traumatic events such as gastric aspiration, near drowning, severe pneumonia, etc. damage the epithelial cells lining in the pulmonary airways, which can lead to a multitude of other problems including pulmonary surfactant (or lung surfactant) inactivation by leaked serum proteins. In severe cases, this damage may progress to acute respiratory distress syndrome (ARDS) that requires mechanical ventilation treatments in intensive care unit, resulting in a mortality rate of 30 % out of 200,000 in the United States. These ventilation treatments can cause further damage if done incorrectly, causing ventilator induced lung injury (VILI).

In this study, we designed and created an asymmetric bifurcating pulmonary model by creating a standardized geometry, and then systematically changing three parameters (daughter channel width, carina tip location, and daughter channel length) in order to observe their effects on the reopening profile with different solutions. We have found that pulmonary surfactant has the ability to balance the bubble propagation in asymmetric daughter sections. We hypothesize that the combination of surfactant's molecular mobility and proper flow patterns generate sharp concentration gradients along the air-liquid interface impose additional resistance to balance the bubble propagations. Understanding this phenomenon could lead to more uniform lung airway reopening and ultimately help develop a ventilation pattern capable of limiting VILI that can be caused by the required treatment of ARDS.

A MICROFLUIDIC MODEL OF PULMONARY AIRWAY REOPENING IN

ASYMMETRIC BIFURCATING NETWORKS

A THESIS

SUBMITTED ON THE FIRST DAY OF MAY 2015

TO THE DEPARTMENT OF BIOMEDICAL ENGINEERING
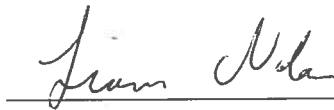
IN PARTIAL FULLFILLMENT OF THE REQUIREMENTS

OF THE SCHOOL OF SCIENCE AND ENGINEERING

OF TULANE UNIVERSITY

FOR THE DEGREE OF

MASTER OF SCIENCE

BY

_____

Liam P. Nolan

Approved: _____
                          Donald Gaver, Ph. D.
                                    Director

_____
                          Bruce Gibb, Ph. D

_____
                          Eiichiro Yamaguchi, Ph. D.

Acknowledgements

Contents

List of Figures

List of Tables

Chapter 1: Introduction

Traumatic events such as gastric aspiration, near drowning, severe pneumonia, etc. will damage the epithelial cells lining the pulmonary airways, which can lead to a multitude of other problems including pulmonary surfactant inactivation by leaked serum proteins. In severe cases, this damage may progress to acute respiratory distress syndrome (ARDS), that requires mechanical ventilation treatments in the intensive care unit, resulting a mortality rate of 30 % out of 200,000 cases in the Unites States (Yamaguchi et al. 2014).

In healthy lungs, pulmonary surfactant reduces the energy required for the inhalation/exhalation cycle by lowering the surface tension of the lining liquid layer inside the pulmonary capillary airways. The lowered surface tension also contributes to keep capillary airway networks open during the exhalation period, helping it uniformly distribute inhaled oxygen without creating local pressure accumulation points. Therefore, mechanical ventilation is a necessary life sustaining intervention that assists the breathing of patients whose pulmonary surfactant has lost its protective function due to the leaked proteins and airway collapse during exhalation. Even though the forced airway re-opening of the surfactant deactivated lung has a high risk of developing ventilation-induced lung injury (VILI), leading the patient to progressive failure stages of ARDS treatment, it is currently the only available option that will keep the patient alive.

In past years, our laboratory contributed to improve mechanical ventilation treatment by approaching multiple aspects of protective airway re-opening strategies,

such as: computer simulation of airway re-opening in rigid and flexible straight tubes, in-vitro experiments of epithelial cell damage from various flow patterns with and without lung surfactant, and flow visualizations of the re-opening phenomena with various shapes of micro-channels and solutions. We have successfully modeled (Figure 1) that indicates that the pressure gradient, not stress, near the tip of a passing air-bubble has a strong correlation to the degree of epithelial damage; therefore, the relationship between bubble tip velocity and surfactant accumulation on the air-liquid interface is key to understanding lung injury prevention. The surfactant experimental results indicate (Figure 2i) that protein-based lung surfactant can alter surface tension dynamically and that the flow visualization confirmed the existence of surfactant converging/diverging points as well as circulating flow patterns in the liquid sub-layer near the tip (Figure 2ii). Our next step is to extend the accumulated knowledge from the study of a straight tube to a branched capillary network, which is more physiologically relevant to the human lung, in order to understand the controllability of airway reopening through mechanical ventilation. Our previous study on symmetrical Y-shape bifurcation suggests (Yamaguchi et al. 2014) that the unique dynamic property of lung surfactant plays an important role to stabilize the penetrating speed of the air-liquid interface, which may result in even or controllable reopening throughout a multi-generational branching network of airways.

3
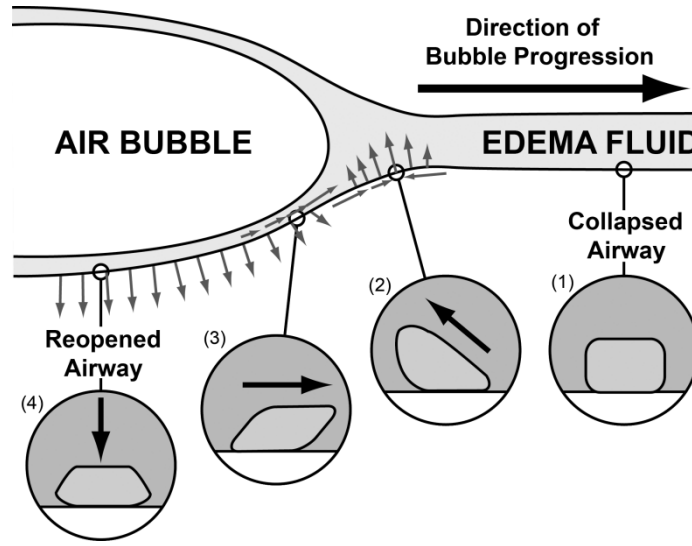
Figure 1 - "Cell dance" that occurrs during reopening of airway. This shows that it is the pressure gradient near the bubble tip that is responsible for the amoutn of cell damage during airway reopening(Gaver et al. 1996)**.**
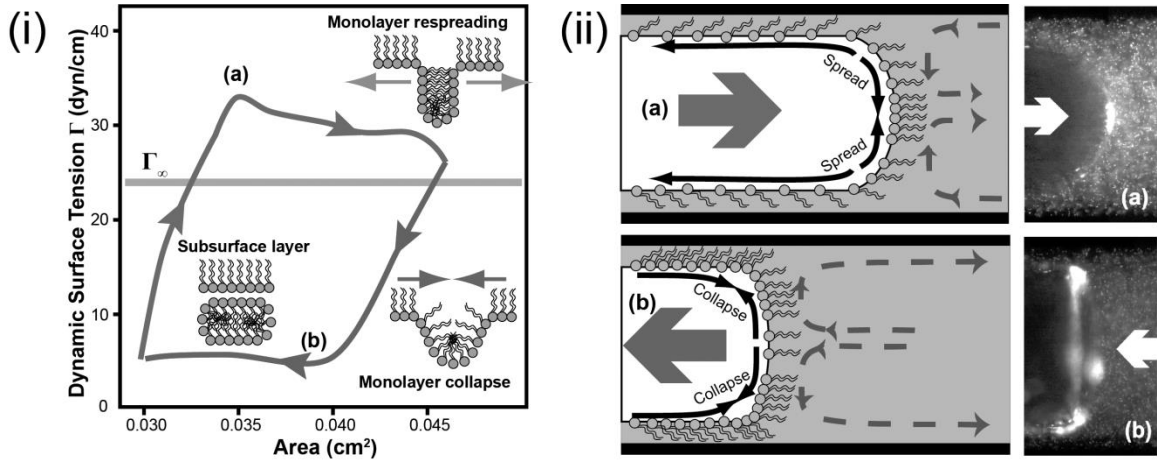
Figure 2 – (i) Pulmonary surfactant loop that occurs during the change in surface area. (ii) Flow visualization confirmed existence of surfactant converging/diverging points as well as circulating flow patterns in the liquid sub-layer near the tip (Yamaguchi et al. 2012)**.**

In this report, we present an experimental investigation of a semi-infinite bubble penetration through a fluid occluded asymmetric Y-shaped bifurcation model of

pulmonary airways as a simulated airway reopening process near a bifurcation point. We aim to characterize and quantify the role of lung surfactant as a stabilizer of bubble progression and to investigate the impact of surfactant's dynamic properties on various asymmetric bifurcation geometries. The following specific aims were completed in order to accomplish these goals:

1) Designing of asymmetric microfluidic models of single generation airway networks that are physiologically relevant to the human lung.

2) Manufacturing of a micro-size bifurcation channel apparatus for the flow visualization experiment.

3) Flow visualization of penetration of semi-infinite air-bubble tip through fluid occluded asymmetric bifurcation channels using micro-scale particle image velocimetry (μ-PIV).

4) Obtaining instantaneous bubble progression velocity throughout the bifurcation process in order to examine the stability and profile of the simulated airway reopening.

5) Characterization of the influence of different geometrical parameters (daughter channel radius, length, and carina tip location) in bifurcations on the reopening profile in single branching networks.

Chapter 2: Background

In this chapter, we will discuss the details of several interrelated areas of focus related to this current objective: 1) morphology of the healthy lung; 2) healthy pulmonary surfactant function and its dysfunction with ARDS; 3) microfluidics and its applicability to the current study; 4) measurement of microscale flow fields through particle image velocimetry (PIV).

2.1 Lung and Airway Morphology

Until the early 1960's, the size and number of airways and alveoli were reported in such a large range that any estimate provided only limited benefit. The estimated number of alveoli ranged from 150 million to 1.8 billion between 1880 and 1922 (Willson 1922). In a 1963 monograph, Ewald Weibel presented a new systematic method of measuring and quantifying the structure of the entire lung. This model provided important morphometric relationships of the lung that remain unchanged today.

Weibel's analysis of the airways of the lung led to two models: Model A assumes there is a symmetric bifurcation at each generation, and Model B allows for an asymmetric branching pattern at each bifurcation (Weibel 1963). Figure 3 shows the symmetric and asymmetric branching patterns represented in Models A and B. In Model A, the ratio of parent diameter to daughter diameter is found to be ~1.2-1.5. The average airway length between bifurcations is three times the diameter of the airway. These branching patterns will be important for the model design of our studies.
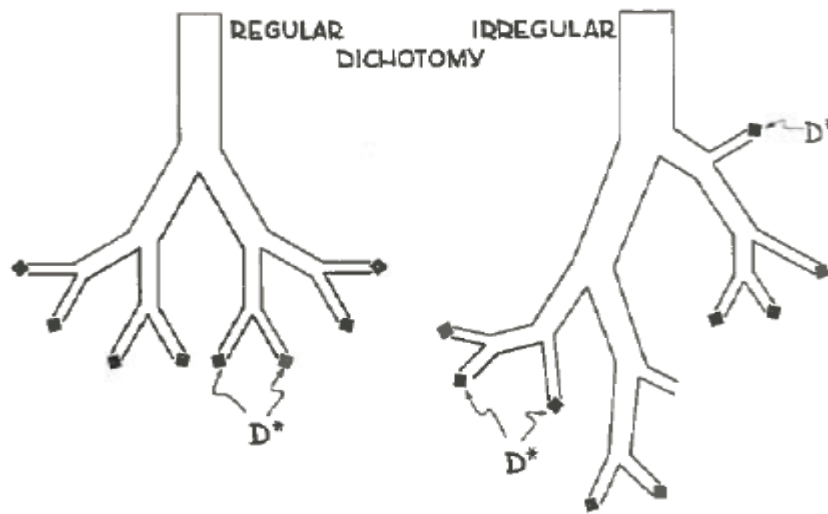
Figure 3 - Regular (left) and irregular (right) dichotomies of airway branching (Weibel 1963)**.**

The airways of the lung form a branching pattern beginning at the trachea and bifurcate down an average of 23 generations, ending in the terminal bronchioles and the alveoli where gas exchange occurs. This study will focus on terminal bronchioles, specifically generations 17-23. Table 1 displays the dimensions for each generation in Model A.

Table 1 - Dimensions of human Model A (Weibel 1963)

Generation z	Number per generation $n(z)$	Diameter $d(z)$ cm	Length $l(z)$ cm	Total crossection $S(z)$ cm^2	Total volume $V(z)$ cm^3	Accumul. volume $\sum_{i=0}^{z} V(i)$ cm^3
0	1	1.8	12.0	2.54	30.50	30.5
1	2	1.22	4.76	2.33	11.25	41.8
2	4	0.83	1.90	2.13	3.97	45.8
3	8	0.56	0.76	2.00	1.52	47.2
4	16	0.45	1.27	2.48	3.46	50.7
5	32	0.35	1.07	3.11	3.30	54.0
6	64	0.28	0.90	3.96	3.53	57.5
7	128	0.23	0.76	5.10	3.85	61.4
8	256	0,186	0.64	6.95	4.45	65.8
9	512	0.154	0.54	9.56	5.17	71.0
10	1024	0.130	0.46	13.4	6.21	77.2
11	2048	0.109	0.39	19.6	7.56	84.8
12	4096	0.095	0.33	28.8	9.82	94.6
13	8192	0.082	0.27	44.5	12.45	106.0
14	16384	0.074	0.23	69.4	16.40	123.4
15	32768	0.066	0.20	113.0	21.70	145.1
16	65536	0.060	0.165	180.0	29.70	174.8
17	131072	0.054	0.141	300.0	41.80	216.6
18	262144	0.050	0.117	534.0	61.10	277.7
19	524288	0.047	0.099	944.0	93.20	370.9
20	1048576	0.045	0.083	1600.0	139.50	510.4
21	2097152	0.043	0.070	3220.0	224.30	734.7
22	4194304	0.041	0.059	5880.0	350.00	1084.7
23*	8388608	0.041	0.050*	11800.0	591.00	1675.0

* Adjusted for complete generation.

Table XI.3. *Dimensions of Respiratory Zone of Human Airway Model "A"*

Generation z	Fraction of surface alveolated $\eta(z)$	Number of alveoli per duct	Number of alveoli per generation	Air-tissue interface $I_{A-T}(z)$ cm^2	Capillary volume $V_O(z)$ cm^3	Tissue-blood interface $I_{T-B}(z)$ cm^2
0	0.0					
...						
16	0.0					
17	0.12	5	$0.6 \cdot 10^6$	$0.16 \cdot 10^4$	0.28	$0.14 \cdot 10^4$
18	0.25	8	$2.0 \cdot 10^6$	$0.54 \cdot 10^4$	0.97	$0.47 \cdot 10^4$
19	0.50	12	$6.0 \cdot 10^6$	$1.62 \cdot 10^4$	2.90	$1.40 \cdot 10^4$
20	1.00	20	$21.0 \cdot 10^6$	$5.70 \cdot 10^4$	9.80	$4.90 \cdot 10^4$
21	1.00	20	$41.5 \cdot 10^6$	$11.30 \cdot 10^4$	19.60	$9.70 \cdot 10^4$
22	1.00	20	$84.0 \cdot 10^6$	$22.70 \cdot 10^4$	39.20	$19.60 \cdot 10^4$
23*	1.00	17*	$143.0 \cdot 10^6$	$38.60 \cdot 10^4$	67.20	$33.40 \cdot 10^4$

* Adjusted for complete 23rd generation.

Following Weibel's model, Horsfield and Cumming explored the asymmetric nature of the human lung. These studies provided evidence to the degree of asymmetries that can be found in the human lungs. These examinations also concluded that many conducting airways are actually elliptical, rather than circular, and that the parent branch has an expansion region prior to splitting into two daughter channels (Horsfield et al. 1971).

In 1992, Hammersley and Olson presented data that would further expand the scale models for flow research from measurements of airway casts (Hammersley & Olson 1992). They found that as the airways progress distally, variations decline. Therefore lower generations should have more uniform geometries. Figure 4 shows the components of the characteristic bifurcation. This bifurcation model is composed of parent diameter D_o, parent length L, daughter diameter D_2, angulation, and radius of curvature. The major regions in this model are the parent channel, elliptical region, carinal region, and daughter channels.
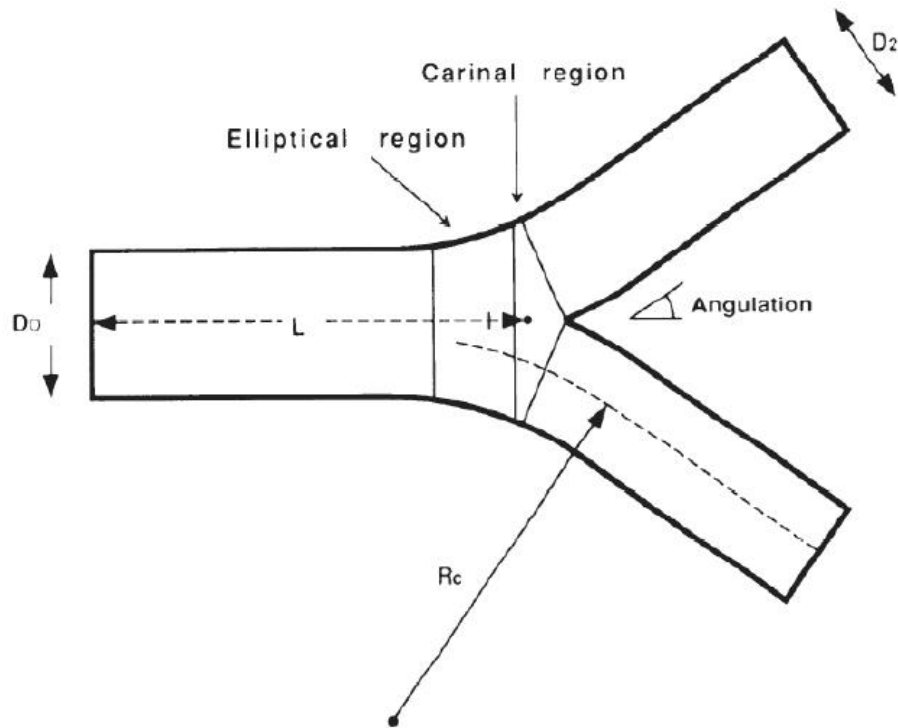
Figure 4 - Major components and regions of airway bifurcation: parent diameter (D_o), daughter diameter (D_2), length (L), branch angulation, and radius of curvature (R_c) (Hammersley & Olson 1992)**.**

The ratios of the geometries in the airways were found to be fairly consistent across generations in the conducting region of the lung. L/D is the length to diameter ratio and was found to be ~ 2-3, and the radius of curvature to diameter ratio was found be vary from ~2-10. Angulation data shows that the branching angles expand as airways get smaller (Hammersley & Olson 1992).

The dimensions, airflow velocity, and dimensionless parameters for convective and diffusive airflow through the inflating lung are presented in Table 2. Orders 3-7

came directly from measurements of airway casts, while extrapolation provides the data all the way to the terminal bronchiole of order 16 (Hammersley & Olson 1992). This information provides the rationale for the conditions in our model.

Table 2 - Dimensions, inspiration mean velocity, and associated dimensionless parameters describing flow for the trachea through the terminal bronchiole (Hammersley & Olson 1992)**.**

Location	Order	Diameter, cm	Distance to Alveoli, cm	Mean Velocity, cm/s	Reynolds No.	Dean No.	Peclet No.
Trachea	0	1.8	31.1	250	2,400	3,000	1,250
Primary bronchi	1	1.3	19.1	240	1,670	3,000	505
Lobar bronchi	2	0.94	14.9	229	1,500	2,300	344
	3	0.72	11.9	224	860	1,200	262
Segmental bronchi	4	0.57	9.5	127	390	600	117
	5	0.45		121	300	500	88
	6	0.36		71	150	250	38
	7	0.30		63	100	180	31
	8	0.24		61	80	150	24
	9	0.20		36	40	70	12
Bronchiole	10	0.16	2.8	35	30	60	9
	11	0.13		18	12	50	4
	12	0.11		16	9	40	3
	13	0.09		15	7	30	2
	14	0.074		8	3	12	1
	15	0.061		8	2.5	10	0.8
Terminal bronchiole	16	0.050	0.7	7	2	8	0.6

Flow rate = 500 ml/s. [Adapted from Olson (8).]

Table 2 shows that the mean velocity in terminal airways (generation 16) of their model is 7cm/s when one is inhaling at a flow rate of 500ml/s. This is a typical peak inspiratory airflow (PIF). When at rest the body's PIF is typically around 500ml/s, and can exceed 4L/s if the body is put under a heavy work load (Coyne et al. 2006). PIF during stable mechanical ventilation is 930±50ml/s (Ntoumenopoulos et al. 2011). In 2004, Frijlink and De Boer, continued the work of Hammersley and Olson, and measured the speed of airway transport in the 23rd generation to be 0.5 mm/s during healthy lung function (Frijlink & De Boer 2004). This is the velocity that we will use in our model.

2.2 Pulmonary Surfactant and ARDS

Once the morphology of the human lung is understood, it is necessary to understand how surfactant aids the breathing process and how detrimental it can be if it does not work properly.

The Young-Laplace relationship characterizes pressure drop across a spherical bubble of radius R:

$$\Delta P = \frac{2\gamma}{R} \tag{1}$$

where γ is the surface tension of the interface. This relationship shows that the pressure required to maintain a bubble is directly proportional to the surface tension. The importance of this to the pulmonary system is shown with the examination of connected spheres (alveoli) with a common pressure and a constant surface tension, as shown in Figure 5.
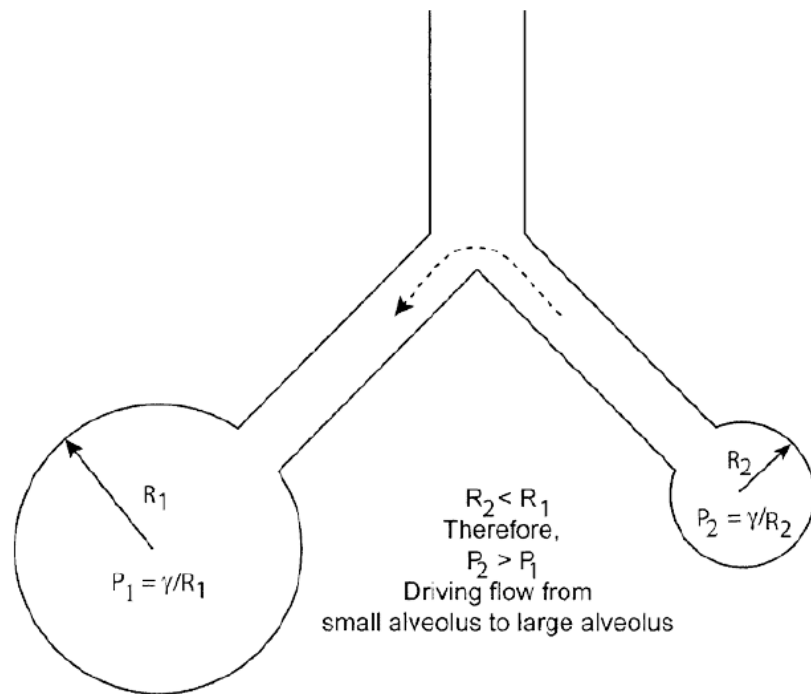
Figure 5 - Connected alveoli illustrating the driving force of collapsing the smaller alveolus in the case of constant surface tension. Surfactant allows for the smaller alveolus to have a lower surface tension preventing collapse (Gaver III et al. 2006)**.**

The constant surface tension case shown in Figure 5 depicts the importance of variable surface tension within the lungs. Here two alveoli of different sizes (R_1 and R_2) are presented with the same pressure and the constant surface tension leads to the smaller alveolus to collapse and the larger one to become over distended. Fortunately, the surface tension of pulmonary surfactant varies as a function of compressive area. The surface tension drops as the area of the interface reduces, allowing for equal pressure between two different sized alveoli, eliminating alveolar collapse and over distention.

14

Lung surfactant lowers the equilibrium surface tension γ_{eq} of the fluid lining from that of water (72dyn/cm) to approximately 30dyn/cm. Figure 6 shows the dynamic behavior of the surface tension of pulmonary surfactant as the interface area changes. Additionally, with interface compression, the surface tension can reach near zero values. A good surfactant provides both a low equilibrium surface tension and an even lower dynamic interfacial tension which minimizes the work of breathing, stabilizes alveoli against atelectasis during expiration, prevents excess liquid from accumulating in the lung, and ensures uniform inflation on inspiration (Zasadzinski et al. 2010).
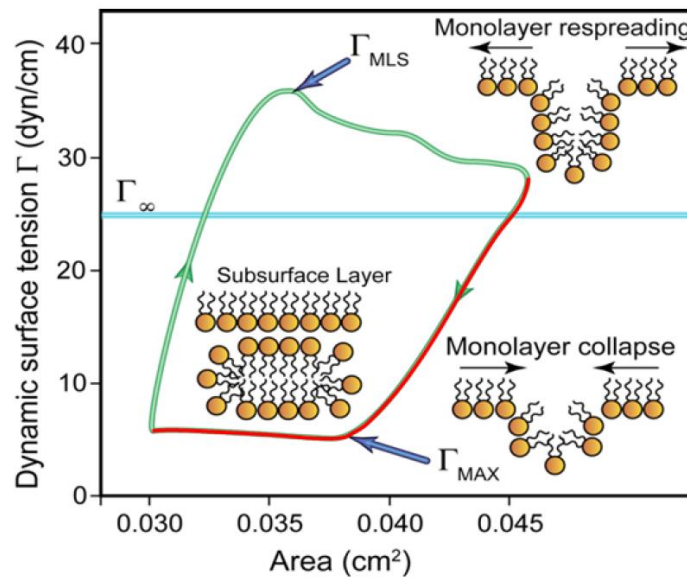
Figure 6 - Isotherm of surfactant showing the change in surface tension as the interface is cycled and the change in surface concentration (Γ). As the area is reduced (red), the surface concentration increases to Γ_{max} and stays high through compression. As as spreading begins (green), the surface concentration rises to Γ_{mls} with monolayer respreading. The blue line representss Γ_{∞}, the equilibrium surface concentration (Krueger & Gaver III 2000)**.**

When lungs are affected by ARDS, surfactant loses these protective properties. The epithelial lining of the airways is composed of flat type I and cuboidal type II cells. Type I cells line 90% of the alveolar surface area and are easily injured. The remaining 10% of the surface area consists of type II cells. These cells produce surfactant, facilitate ion transport and differentiate into type I cells after injury. Epithelial injury can contribute to alveolar flooding and injury to type II cells by disrupting normal epithelial fluid transport and impacting the removal of edema fluid from alveolar space (Ware & Matthay 2000). The breakdown of the epithelial alveolar lining allows serum proteins to infiltrate the alveolar space, and functioning pulmonary surfactant proteins are inactivated and washed away. The damage compromises the epithelial cell monolayer, which further reduces surfactant production by type II cells, which then leads to increased permeability of edema fluid from airspaces resulting in a self-perpetuating feedback loop (Gaver III et al. 2006). This feedback loop eventually results in ARDS. Figure 7 shows the components of a healthy alveolus as well as the changes found with ARDS.
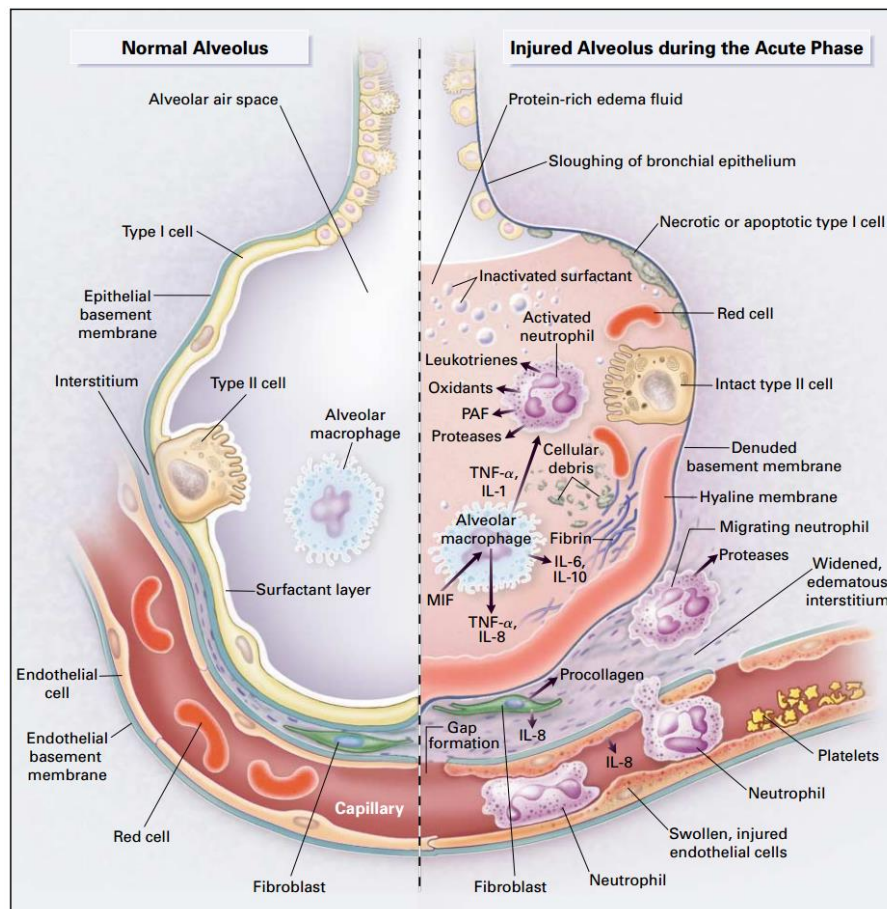
Figure 7 – Normal alveolus (left side) and injured alveolus during ARDS (right side). The normal alveolus is entirely lined with epithelial cells and a surfactant layer creating a complete boundary layer between the airspace and the capillaries. The injured alveolus has fewer healthy epithelial cells lining it with more necrotic or apoptotic type I cells. The blood-airspace barrier is broken down and serum proteins infiltrate the airspace deactivating the surfactant (Ware & Matthay 2000)**.**

Treating ARDS requires a delicate balance, as it is necessary for the body to continue respiration; however, the necessary mechanical ventilation can lead to injury of its own. Optimal ventilation protocols rely upon a strategy of preventing the collapse and reopening of compliant airways and alveoli while simultaneously avoiding over distention. Further damage to the lung caused by the ventilator is called ventilator

induced lung injury (VILI). To attempt to combat VILI, numerous ventilation techniques have been developed. For example, altering mechanical ventilation tidal volumes from the standard 12ml/kg of body weight to 6ml/kg of body weight resulted in a 22% reduction in mortality rate (Ware & Matthay 2000). Another study has also shown that increasing frequency of ventilation and reducing tidal volumes of mechanical ventilation improved oxygenation and survival rates (Derdak et al. 2002).

Airway collapse is characterized by two main mechanisms, meniscus formation and compliant collapse; closure can occur when fluid accumulates or when highly compliant airways collapse. Figure 8 shows the differences between the two alternative mechanisms of airway closure. With meniscus formation, the unstable lining fluid leads to a fluid plug formation in a rigid airway. Alternatively, with compliant collapse, the walls of the airway come together, forming an occlusion.
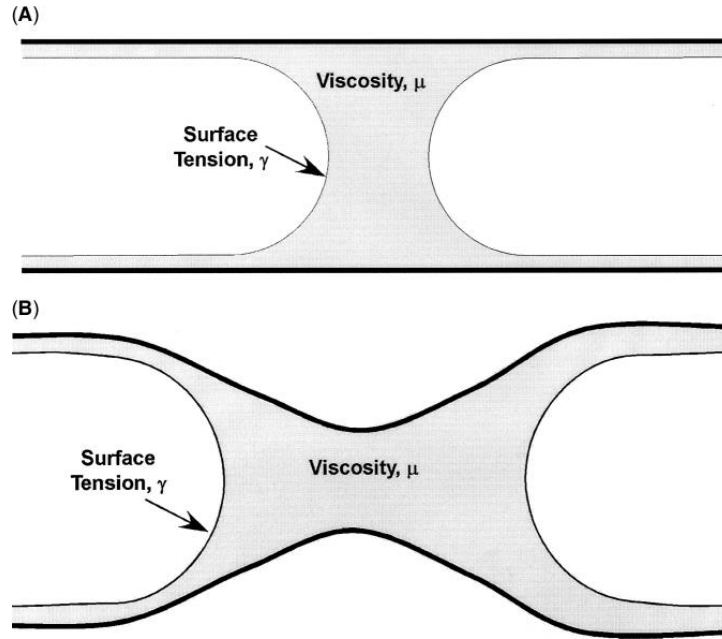
Figure 8 - Two Mechanisms of airway collapse: (A) meniscus formation, (B) compliant collapse (Gaver III et al. 2006)**.**

The yield pressure required to reopen a collapsed airway with constant surface tension is proportional to the surface tension at the air-liquid interface and the radius, characterized by the relationship:

$$P_{yield} \sim \frac{8\gamma}{R} \tag{2}$$

where γ is the surface tension at the interface and R is the interfacial radius (Gaver et al. 1990). Using this approximation, the yield pressure for reopening bronchioles in adults with normal surfactant function is $P_{yield} \sim 5cm\ H_2O$, which is low enough to avoid damage to the cells lining the airway. However, the pressure to open an occluded airway in an adult with ARDS is $P_{yield} \sim 15-20cm\ H_2O$, and for premature infants with surfactant

deficiency it is P_{yield} ~50cm H_2O. These pressures are exerted globally on the lung and are the basis for further damage in patients with surfactant inactivation and/or deficiency (Gaver III et al. 2006).

2.3 Microfluidics and Microfabrication Techniques

After understanding the morphology of the lung, and the importance of ARDS, we must choose a method that is capable of creating a pulmonary model of pulmonary airways on the scale of terminal airways. We have chosen to use microfabrication. Microfabrication is a process used to construct physical objects with dimensions in the micrometer to millimeter range. It takes advantage of established semiconductor fabrication processes, used to make integrated circuits, and augments these with processes specially developed for microfabrication (Voldman et al. 1999). Since microfabrication techniques can create channels with such a wide variety of sizes, the different sizes of channels have been classified based on their hydraulic diameters. Table 3 displays the various classifications of channels and their applications.

Table 3 - Channel classification scheme (Kandlikar et al. 2006)**.**

Classification	Gas flow (Air)	Liquid flow	System	Application
Conventional channels			PIV	
Mini-channels (3 mm – 200 μm)	Continuum flow $Kn>0.001$	Continuum flow	**Mini-PIV**	Adult Human Respiratory Airway
Micro-channels (200 μm – 10 μm)	Slip flow $0.1>Kn>0.001$		Micro-PIV	MEMS, TAS & Biodevices
Transitional micro-channels				
Transitional channels	Transition flow $10>Kn>0.1$			
Transitional nano-channel (0.1 μm)				
Nano-channels	Free molecular flow $Kn>10$			

Hydraulic diameter — *Large* ↑ / *Small* ↓

Although the above criteria are developed mainly from gas flow considerations, they are recommended for both liquid as well as two phase flow applications to provide uniformity in channel classifications. Even though no fundamental change occurs in the single phase liquid and gas flows or two-phase flows in channels up to 200μm, the manufacturing techniques and operational considerations for cleanliness become extremely important for channels below 200μm (Kandlikar & Grande 2003). Since our model will imitate terminal airways, the features of our model will vary between 140-250μm. Because of this, careful consideration had to be taken when choosing the fabrication technique because the features of our model are near this 200μm cut-off for operational cleanliness and exist in between the microchannel and minichannel classification. Soft Lithography and PDMS replica molding processes meet the stated

requirements and allow for the production of microfluidic channels with depths as high as 150μm; therefore, they were selected to create our model. The length scale also compares to the approximate dimensions of the terminal bronchioles. The steps involved in soft lithography with PDMS replica molding include rapid prototyping, contact photolithography, replica molding, sealing, and surface treatment.

Rapid prototyping begins with creating a device in a computer-aided design (CAD) program. A high resolution printer then prints a negative of the channel design, and this transparency serves as a photomask during contact printing.

Contact photolithography is a process where the entire pattern of a photomask can be projected onto a thin film of photoresist at the same time. This process creates a negative of the designed channel on what is called a master wafer. State of the art photolithographic techniques are capable of mass-producing patterned structures on thin films of photoresist with feature sizes as small as ~250nm, and can create full designs that are 10 centimeters in size (Xia & Whitesides 1998a). Other forms of photolithography such as soft X-ray lithography, e-beam writing, focused-ion beam writing, and proximal-probe lithography have been used to create features as small as 100nm, but their development into economical methods for mass-production of nanostructures still requires substantial effort (Xia & Whitesides 1998a).

Once a master wafer is fabricated, channels are formed in PDMS by replica molding. Replica molding is simply the casting of prepolymer against a master wafer and generating a negative replica of the master in PDMS. PDMS is chosen for this step

because it is transparent, which allows for easy flow visualization, and can be made to have acceptable wetting properties.

Molding provides a PDMS replica that contains three walls, and sealing the mold to a test slide provides the fourth. Sealing occurs two ways: reversible, and irreversible. We will irreversibly seal our surfaces by exposing both surfaces to oxygen plasma.

Once the channel is sealed, the surface of the channel must be treated because unmodified PDMS presents a hydrophobic surface. Channels in hydrophobic PDMS are difficult to wet with aqueous solutions, are prone to adsorption of other hydrophobic species, and easily nucleate bubbles. Exposure to plasma oxidation, however, renders the surface hydrophilic because of the presence of silanol groups on the walls of the channel provides ionizable groups (McDonald et al. 2000). Once the channel sealed, if it is filled with a silane solution, the walls will become permanently hydrophilic. Once the surface has been treated, the channel is cured for 8 hours to finish curing the PDMS and let to sit for another 12 hours. The PDMS finishes curing after bonding is finished because this allows for a stronger bond between the replica mold and the test slide (Bhattacharya et al. 2005). This microfabrication technique is further explored in section 3.1.2.

2.4 Particle Image Velocimetry

The reopening model of a semi-infinite air bubble penetrating a fluid occluded tube is an example of a biphasic flow. Therefore, the behavior near the interface between air and liquid cannot be simply modeled with traditional fluid mechanic equations. This increased complexity has been the basis of a number of investigations to characterize

fluid profile near the interface. Micro particle velocimetry (μ-PIV) has been used to characterize the flow fields surrounding a migrating semi-infinite bubble as it progresses through a capillary tube (Smith 2009; Yamaguchi et al. 2012).

μ-PIV provides the *accurate, quantitative measurement of fluid velocity vectors at a very large number of points simultaneously* (Adrian 2005). In order to achieve this, the fluid is seeded with fluorescent microparticles and excitation light is pulsed successively with a known time delay (Δt) in order to excite the fluorescent particle, and the fluorescence of each pulse is imaged. From the particle images with a known Δt, the position of each image can be interrogated to form a two dimensional velocity profile of the fluid flow.

Averaging of repeated trials allows for estimation of the location of the air-liquid interface, though it is not capable of accurately determining large deformations during Δt. It is for this reason that before accurate measurements can be taken with the PIV system, various parameters must be set. These parameters include interrogation window size, flow rate of the syringe pump, Δt, image acquisition rate, and number of images. How the values for these parameters are selected will be discussed in 3.2.3.

A previous study done in our laboratory used two separate image locations in order to measure the flow fields surrounding the progressing bubble tip near the bifurcation and to monitor the flow-rate of the bubble propagation (Yamaguchi et al. 2014). The observation window setting for this technique can be seen in Figure 9a, b. This technique has since been improved so that only one image acquisition location is

required. In order for the image to take both required measurements, the position seen in Figure 9bi was shifted slightly to the left. This way the bubble can be observed as it reaches the carina tip, and horizontal downstream velocities can be easily measured. An image of the channel in the new position can be seen in Figure 9c.
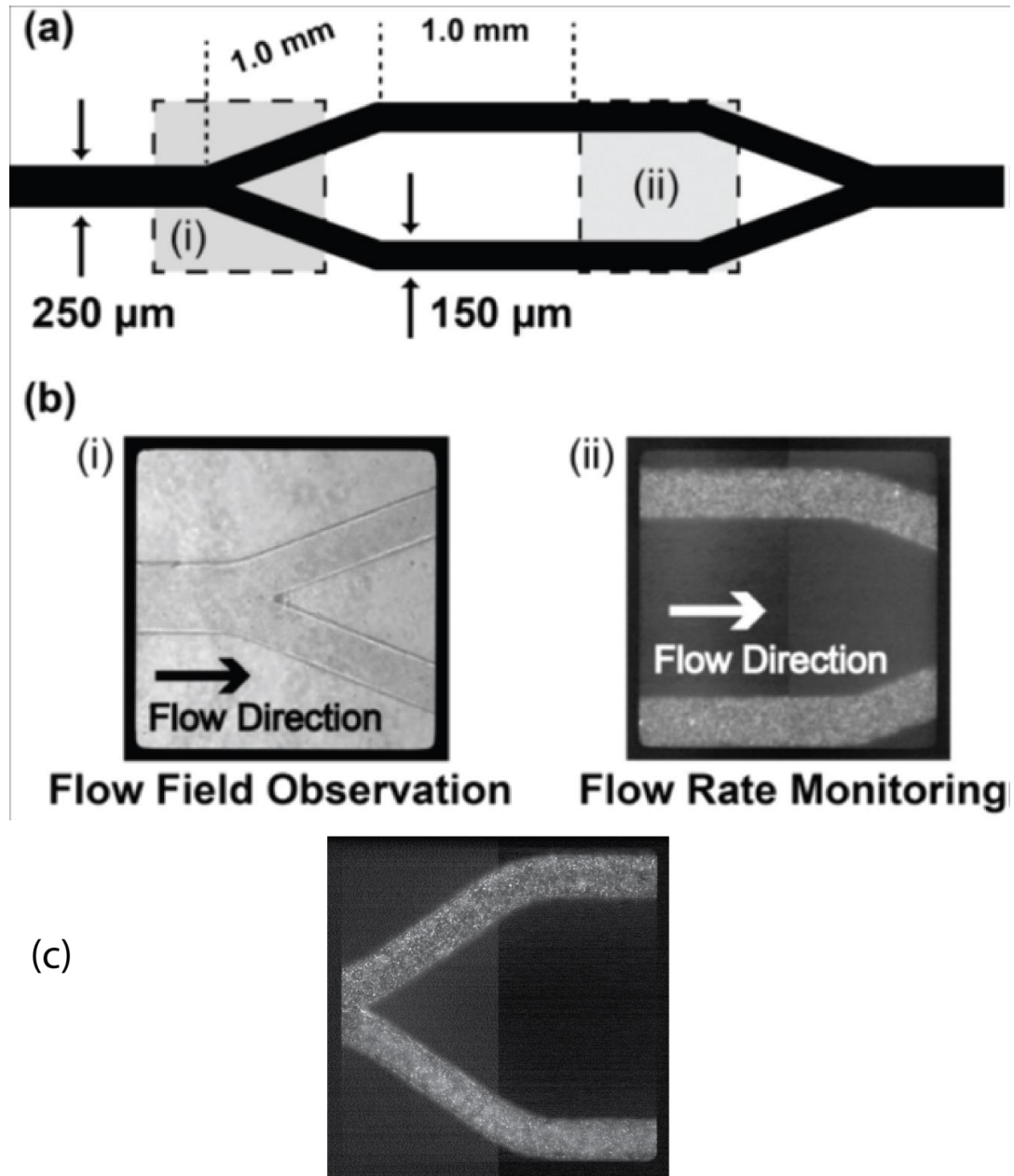
Flow Field Observation and Flow Rate Monitoring

Figure 9 – (a) Schematic of the microfluidic bifurcation channel design. (bi) A sample image of the observation window near the bifurcation where the μ-PIV/Shadowgraph measurements of the flow fields surrounding the progressing bubble tip were taken. (bii) An image of the downstream daughter channels where the flow-rate monitoring of the bubble propagation was performed by using μ-PIV. (c) An image of the adjusted image location that allows for acquisition of both flow fields near bubble tip and down-stream flow rate.

Chapter 3: Materials and Methods

3.1 Microfluidic Studies

3.1.1 Model Parameters

The first step in our microfabrication process is to create a model using morphologically relevant parameters, and then to draw these designs using computer aided design (CAD). The model created for this study was developed within a set of constrains from the fabrication techniques as well as constraints designed to mimic the biological nature of the model.

The systematic constraints were due to the limitations of soft lithography. For features with simple geometries, soft lithography was found to have a maximum useable thickness of 150μm. Once the height of the channels surpasses 150μm, the accuracy of the channel geometry is no longer reliable (Microchem 2015).

The physiological constraints of this study were developed from previous studies of the morphology of the pulmonary airways and their bifurcations. Many models of the lung that have been created over the past 50 years are based from Weibel's symmetric Model A (Weibel 1963). The model for our study, however, is a combination of Weibel's symmetric model A, and the physical models of the smaller airways (Hammersley & Olson 1992) in order to accurately portray the asymmetries that occur naturally in the morphology of the human lung.

Based on the bifurcation model developed by (Lee et al. 2008), lung bifurcations

can be characterized by 11 parameters for i=both left and right (also shown in Figure 10):

- Parent Radius ($\mathbf{R_p}$)

- Length of Parent straight segment ($\mathbf{L_{p,s}}$)

- Radii of Daughter Branches ($\mathbf{R_{di}}$)

- Length of daughter straight segments ($\mathbf{L_{di,s}}$)

- Subtended angles ($\boldsymbol{\beta_i}$)

- Radii of curvature of daughters ($\mathbf{R^*_i}$)

- Radius of curvature of carina ridge ($\mathbf{r_c}$)
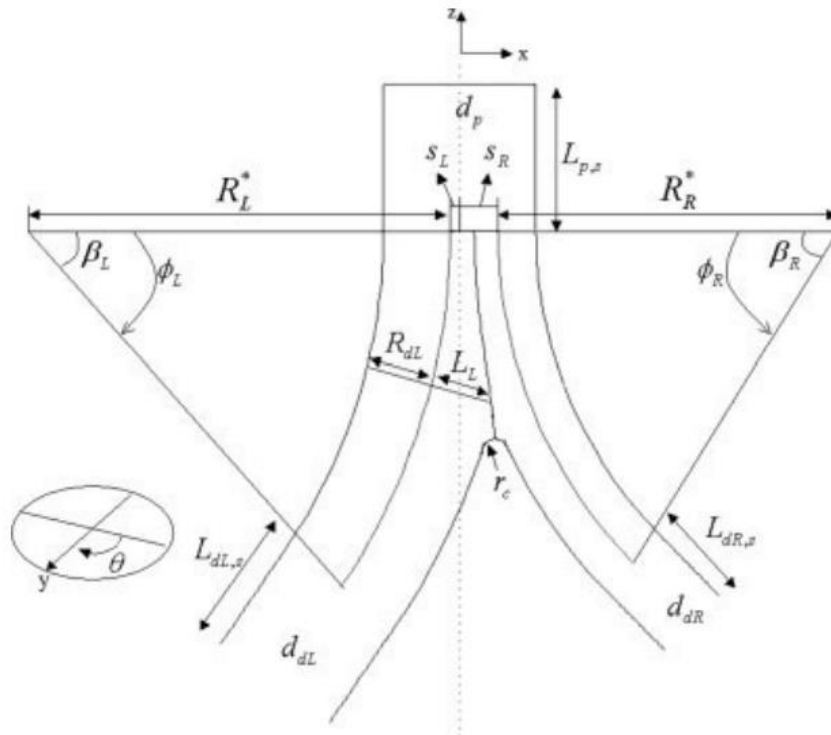
Figure 10 - Schematic representation of the parameters to generate mathematical model of asymmetric airway bifurcation. From Lee et al. 2008

The microfluidic model that we developed uses the two dimensional model shown in Figure 10 as a basis for microchannels with a rectangular cross-section. We used a two dimensional model because soft lithography uses a two dimensional image for projection printing in which the image is reduced and projected onto a thin film of photoresist (Xia & Whitesides 1998b).

First, a standardized geometry was produced to allow for changes in the transition zone to be attributed to one parameter. The standard set of parameters was based on average morphometric data and ratios that appear throughout the literature on airway structure. The average ratio of parent to daughter diameters of the conducting airways is approximately 1.26 (Hammersley & Olson 1992). This ratio was maintained throughout the model utilizing the 150μm thickness available. The parent diameter was held constant at 250μm, and the average width of the two daughter channels was held constant at 150μm. The ratio of radius of curvature of the daughter branch to the diameter of the daughter branch is $2 \leq (\frac{R}{D_d}) \leq 6$ for small airways (Kleinstreuer et al. 2008). The radius of curvature of the daughter channel was held constant at 525μm (R/D_d=3.5). Finally, the ratio of the carinal radius of curvature to the daughter diameter (r_c/D_d) is 0.1, and the angle of branching was set to 35°, which was determined to be the ideal angle for minimal resistance (Horsfield & Cumming 1967). Once the standardized geometry is set, different parameters will be altered in order to measure their influence on the reopening profile. An image of our standardized model can be seen in Figure 11.
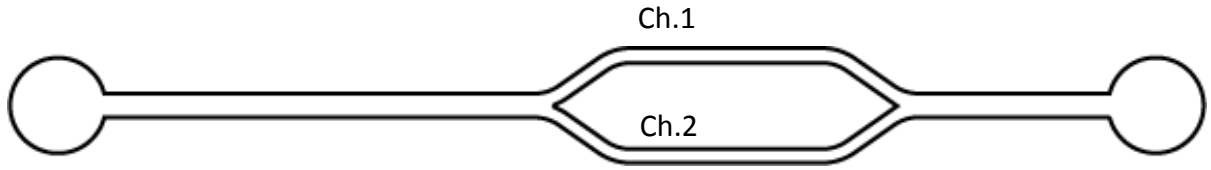
Figure 11 - Model with standardized parameters.

There are three different types of pressures involved in the reopening of a bifurcating channel. The first is capillary pressure drop (P_{Cap}) which occurs at the air-liquid interface. The second one is hydraulic pressure (P_{Hyd}) which is related to the flow of the remaining liquid downstream. The final pressure that is involved is the end pressure; however, in our model the end pressures are equal. Therefore:

$$\Delta P_{Cap1} + \Delta P_{Hyd1} = \Delta P_{Cap2} + \Delta P_{Hyd2} \tag{3}$$

Each one of these pressures is represented in Figure 12. **The overall goal of this study is to reopen an asymmetric channel uniformly with the help of pulmonary surfactant.**

In Pattern A, the two daughter channels have different heights, and the same lengths. This means that both daughter channels will have different capillary and hydraulic pressure drops between daughter channels since

$$\Delta P_{cap} \sim \gamma / H \tag{4}$$

$$P_{hyd} = \frac{12\mu Q}{H^3 D} L(t) \tag{5}$$

P_{cap} reflects the Laplace pressure drop and P_{hyd} is the Channel Poisseuille pressure drop that exists in the column of fluid of length L(t), as described in Figure 12. The three H_1/H_2 ratios used in this study are $H_1/H_2 =160/140$, $H_1/H_2 =155/145$, $H_1/H_2 =152/148$. **The goal of this pattern is to determine how a combination of different capillary and hydraulic pressures between daughter channels will affect the bifurcation's reopening profile.**

In Pattern B the two daughter channels have the same channel width, but different channel lengths. Therefore, both daughter channels will have the same capillary pressure drops, but different hydraulic pressure drops. In order to create the same maximum velocity ratio between daughter channels as in the first asymmetric model, we used

$$\frac{u_{\max 1}}{u_{\max 2}} = (\frac{D_{h1}}{D_{h2}})^2 \frac{L_2}{L_1} \tag{6}$$

Where D_h is hydraulic diameter, $\frac{D_{h1}}{D_{h2}}=1$, and L is total length of daughter channel section. Therefore in order to keep $\frac{u_{max1}}{u_{max2}}$ the same in the second pattern, the ratios $L_2/L_1=1.143$, $L_2/L_1=1.069$, and $L_2/L_1=1.027$ were used. **The goal of this pattern is to determine how the hydraulic pressure difference between daughter channels will affect the bifurcation's reopening profile.**
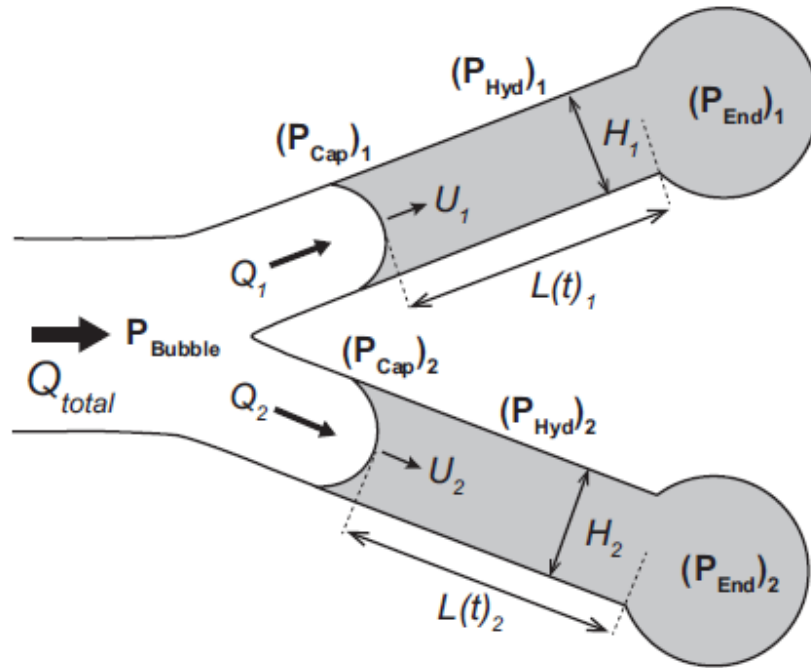
Figure 12 - Schematic diagram of flows, pressures and lengths that exist in the bifurcating channel. In our system, $(P_{end})_1 = (P_{end})_2$. From (Yamaguchi et al. 2014)

Finally, in pattern 3 the carina tip was varied in order to investigate the effect of the surfactant distribution between daughter channels on the reopening profile. In a previous study (Yamaguchi et al. 2012), it was determined that as a semi-infinite bubble propagates forward, surfactant builds up at the front tip (as seen in Figure 13). Moving the carina tip will force this accumulation of surfactant to enter one of the two daughter channels. If this accumulation has an effect on the symmetry of reopening, it will help to determine how much of an effect different concentration of surfactant can have on airway reopening. Accordingly, the carina tip was offset by $\pm 10\mu m$, $\pm 5\mu m$, $\pm 2\mu m$. **The goal of this pattern is to determine how a local change at the carina tip can affect the**

bifurcation's reopening profile. All of the parameters for each model are visible in

Table 4, and the nomenclature for each design is explained in Figure 14. The carina tip

location in each pattern can be seen in Figure 15.
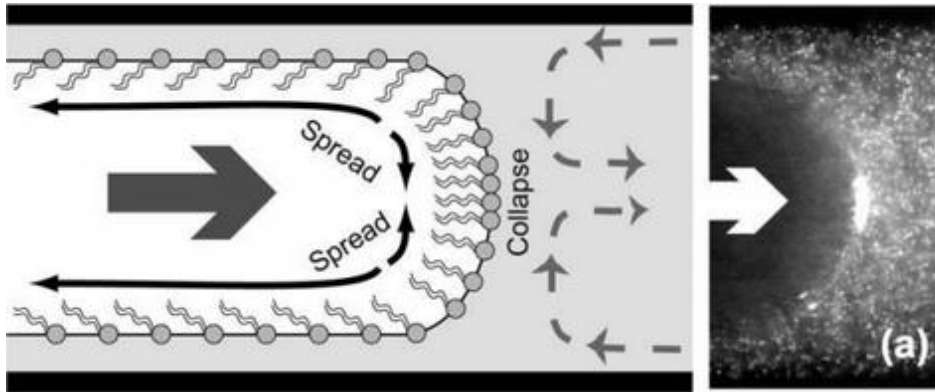
Figure 13 - Prediction schemes of lung surfactant spread patterns during forward progressing mean motion of bubble tip. From(Yamaguchi et al. 2012)**.**

Table 4 - Parameters of bifurcation for asymmetric models.

Model	Parent Diameter Dp(μm)	Daughter Diameter Dd(μm)	Daughter Branch Radius of Curvature R (μm)	Daughter Length 1/Daughter length 2	Carina tip Radius of Curvature rc (μm)	Branching Angle (°)	Carina tip offset (μm)
αA₁	250	160	525	1	15	35	-10
αA₂		140	525			35	
αB₁	250	160	525	1	15	35	+10
αB₂		140	525			35	
αC₂	250	150	525	1.143	15	35	0
αC₂		150	525			35	
αD₁	250	160	525	1	15	35	0
αD₂		140	525			35	
βA₁	250	155	525	1	15	35	-5
βA₂		145	525			35	
βB₂	250	155	525	1	15	35	+5
βB₂		145	525			35	
βC₂	250	150	525	1.069	15	35	0
βC₂		150	525			35	
γA₁	250	152	525	1	15	35	-2
γA₂		148	525			35	
γB₁	250	152	525	1	15	35	+2
γB₂		148	525			35	
γC₁	250	150	525	1.027	15	35	0
γC₂		150	525			35	

α A 1
(i)   (ii)   (iii)

(i) Asymmetric Width of Daughter Channels with Same Length

    α: 160/140
    β: 155/145
    γ: 152/148

(ii) Carina Tip Position (see Figure 15)

    A: straight extension of asymmetric daughter
          channel (below parent channel center line)
    B: tip is adusted to mirror carina tip across
          parent channel center line
    C: assigned to asymmetric length design with same
          daughter channel cross section
    D: tip is adjusted to the centerline of parent section

(iii) Position in Model

    0: Parent Channel
    1: Top Daughter Channel
    2: Bottom Daughter Channel
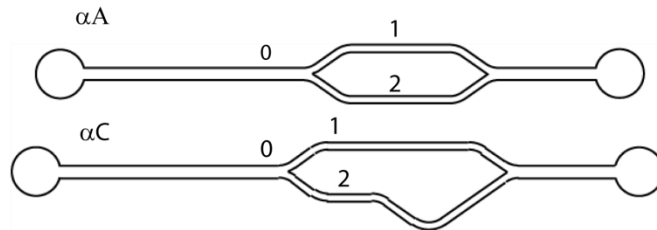
Figure 14 - Nomenclature of each model. (i) denotes the ratio of daughter channel widths. (ii) denotes carina tip location, and whether or not daughter channels have same length. (iii) denotes position in model.
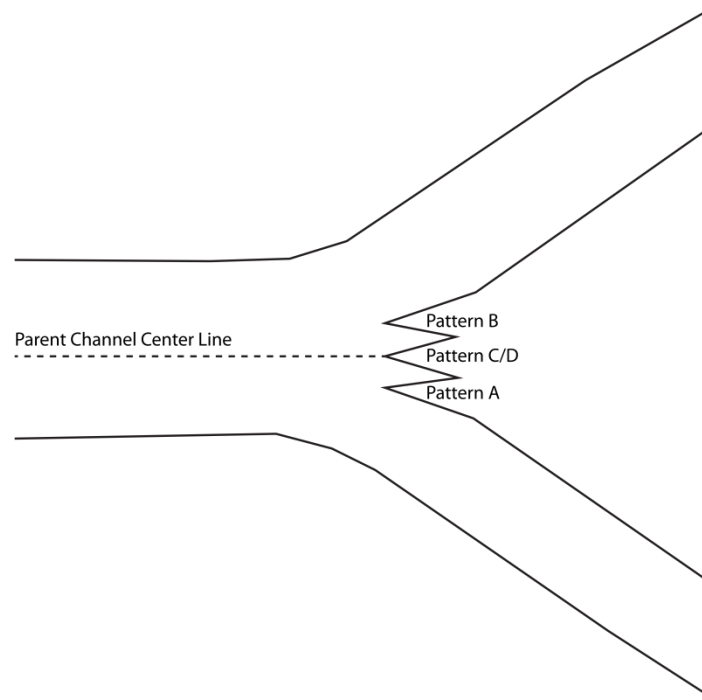
Figure 15 - Carina tip location for each Pattern. Pattern A: tip is below parent channel center line. Pattern B: tip above parent channel center line. Patterns C&D: tip is at parent channel center line.

3.1.2 Device Fabrication

3.1.2.1 Master Wafer Fabrication

In order to create an accurate master wafer, several steps need to be carefully followed. Since our device has very thick height of 150μm, a very viscous photoresist (SU-3050, MichroChem, Newton, MA) is required. The first step is to carefully clean the master wafer. Even though the silicon wafers are cleaned before they are shipped, dust and other particles can accumulate on the surface of the wafer. These particles will cause bumps and imperfections on the channel if not cleaned properly. In order to clean the wafers, the surface is rinsed with de-ionized water and air-dried with nitrogen.

Once the surface of the silicon wafer is clean and dry, the photoresist can be poured onto the wafer. The final thickness of the photoresist is determined by the speed of spin coating, as shown in Equation (7) and Figure 16.
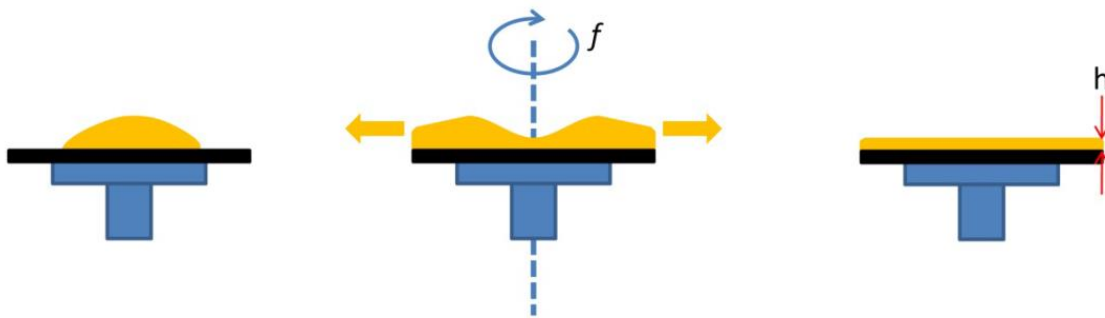
$$h = h_o[1 + \frac{16\pi^2 f^2}{3v} h_o^2 t]^{-\frac{1}{2}} \qquad \text{(Meyerhofer 1978)} \qquad \textbf{(7)}$$

Figure 16 - Spin coating process. (left) photoresist poured onto center of wafer; (center) spinning wafer drives photoresist to edges; (right) uniform thickness (h) of photoresist across entire wafer. from Shevkoplyas, BMEN 676 Lecture 13, Photolithography I, 2010

In order to achieve a channel height of 150μm, two layers of photoresist are required since the tallest layer that can be applied of SU-3050 is 100μm (Michrochem SU-8 3050 Data Sheet). First a 50μm layer is added by pouring a bead in the center of the wafer that covers ~20% of the radius. The wafer is then spun at 500rpm for 30 seconds with an acceleration of 100rpm/second in order to spread the photoresist over the entire surface. Then the wafer is spun at 3000 rpm for 30 seconds with an acceleration of 300 rpm/second. This final speed ensures that the photoresist layer is 50μm throughout the wafer, and excess photoresist is spun off of the wafer. Once spin coating is finished, a needle is used in order to pop any bubbles that remain on the surface of the wafer.

The soft bake process begins after all bubbles have been eliminated. The wafer is placed on a level hot plate in order to drive the solvent out of the photoresist. The hotplate is heated to 65C when the wafer is placed on it. Once the wafer is on the hotplate, the temperature is slowly increased by 5C every minute until it reaches 95C. The wafer is heated at this temperature for one hour.

Once soft bake for the first layer is completed, the wafer is cooled to room temperature, and then put back on the hot plate. If wrinkles form on the photoresist, the wafer is left on the hot plate until no wrinkles form. If none form, it is placed back on the spin coater. A second layer of photoresist is then placed on the center of the wafer. This bead also covers 20% of the radius. The hot plate is cooled back down to 65C. Spin coating of the second layer of 100μm then begins. First the wafer is spun at 500 rpm with an acceleration of 100rpm/second for 30 seconds in order to spread the photoresist over the entire surface of the wafer. Next the wafer is spun at 1000 rpm with an acceleration of 300 rpm/second in order produce the final desired channel height of 150μm. Once more after spin coating is finished, a needle is used in order to pop any bubbles that remain on the surface of the wafer

The soft bake process begins again after all bubbles have been popped. The wafer is placed on a level hot plate in order to drive the solvent out of the photoresist. The hotplate is cooled to 65C before the wafer is placed on it. Once the wafer is on the hotplate, the temperature is slowly increased by 5C every minute until it reached 95C. The wafer is heated at this temperature for one hour. Once soft bake is completed, the wafer is cooled to room temperature, and then put back on the hot plate. If wrinkles form

on the photoresist, the wafer is left on the hot plate. This process is repeated until no wrinkles form.

If no wrinkles form on the surface of the wafer, it is time to expose it. The wafer is placed on the mask aligner, and the photomask is placed on the master wafer such that the channels are positioned at an area of the wafer with minimal surface imperfections. With the mask compressed down on the wafer in the mask aligner (ABM, Scotts Valley, CA), it was exposed to near UV light (350nm-450nm) for 20 seconds.

Post exposure bake begins immediately after exposure. The wafer is heated to 65C, then slowly up to 95C. The wafer was heated at 95C for 2 hours after exposure. The wafer is then returned to room temperature.

Once the wafer has returned to room temperature, the wafer was developed with SU-8 developer (Microchem, Newton, MA). After 15 minutes of developing, it was rinsed with isopropyl alcohol (IPA). Development continued if a white film appeared under the IPA.

The developed wafer is then air-dried with nitrogen, then placed into a vacuum chamber with (tridecafluoro-1,1,2,2-tetrahydrooctyl)trichlorosilane, $C_8H_4C_{13}F1_3Si$ (CAS #78560-45-9) (Gelest, Inc., Morrisville, PA). The wafer is treated for at least four hours in the vacuum chamber. This monolayer of silane prevents irreversible bonding between the silicon and PDMS (Ng et al. 2002). Figure 17 gives a schematic of the photolithographic process.

Transparency
with a pattern

UV light

Photoresist

Silicon wafer

Dissolve uncrosslinked
photoresist

Negative of Channel
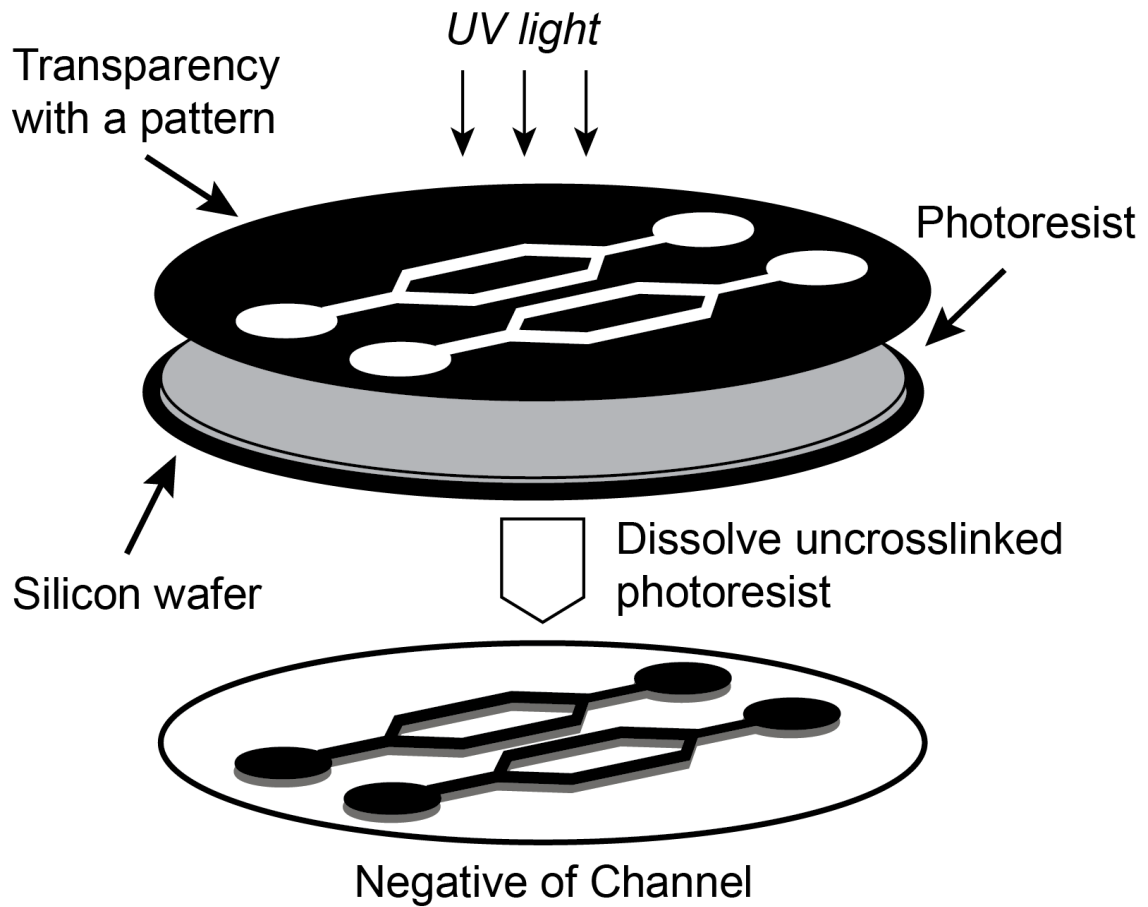
Figure 17 - Schematic of the photolithographic process.

3.1.2.2 Microfluidic Device Fabrication

Once the master wafer is completed, the microfluidic device can be created. The microfluidic device consists of a PDMS mold of the master wafer bonded to a glass slide coated with a thin layer of PDMS. In order to use the lateral positioning control incorporated in the translating stage system described in Smith et al. the base slide used measured 30mm x 161.5mm x 1.1mm (Smith 2009). The PDMS base and curing agent (Sylguard 184, Dow Corning Corporation,MI) are mixed in a 10:1 ratio by weight. This mixture is then placed inside a vacuum for 45 minutes or until all bubbles have left the

mixture. Next, the mixture is poured over the master wafer until it reaches a thickness of ~5mm and cured at 65C for one hour. Once cured, the mold is removed with a scalpel and forceps. Figure 18 shows a schematic of replica molding with PDMS. The base coating of PDMS on the glass slide is formed by pouring the PDMS mixture along the middle ~30% percent of the slide. The slide is then spun at 500rpm for 30 seconds with an acceleration of 100 rpm/second, then 1500rpm for 30 seconds with an acceleration of 300rpm/second. Once spin coated, the slides must be cured for one hour at 65C.

Pour PDMS prepolymer

Cure

Peel off from the negative
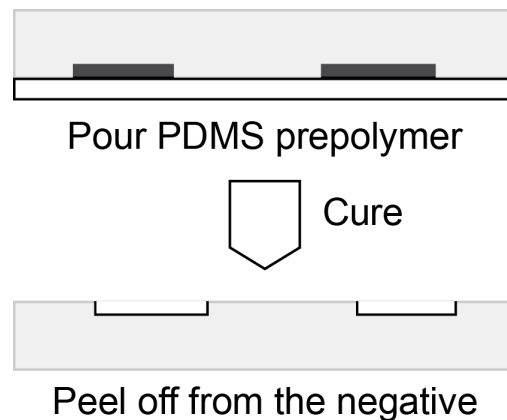
Figure 18 - Schematic of replica molding.

3.1.2.3 Micro-channel Pump Interface

One issue that arises with PDMS molding is that the connection between the microdevice and the pump driving flow must be connected reliably. There can be no leak. If the hole is too small, a crack will form at the connection, hindering flow control within the channel. If the whole is too big, there will be very little flow control. Finally if the connection puts too much stress on the bond between the mold and the slide, the

connection will break, rendering the channel useless. In order to correct this issue, the method from Christensen et al. was adapted (Christensen et al. 2005). Figure 19 depicts the process of creating the connection of the microchannels to the tubing that is connected to the syringe pump. Once the PDMS mold is removed from the master wafer, a sharpened 16 gauge needle is used to bore a plug from the PDMS. The needle should be sharpened after removing 3 holes, and, every time it is sharpened, forceps should be put in the needle in order to ensure that its inner diameter has not decreased due to sharpening. Since the diameter of the hole is equal to the inner diameter of the needle, if it shrinks, it becomes extremely difficult to connect the channel to the flow control pump. This removal is done prior to separating all of the channels and plasma bonding to the glass slide. Once the device is assembled the hole is slightly smaller than 1/16" tubing that connects the pump to the microchannel. If the syringe is not sharpened properly, or if its inner diameter is too small, the hole will crack. This will allow air and water to enter the microchannel, contaminating the solutions in the microchannel and hindering control of the flow. The pump system was already configured to attach to 1/16" glass tubing, so finding a method to connect this tubing to the microchannel allows for a simple connection method.

42
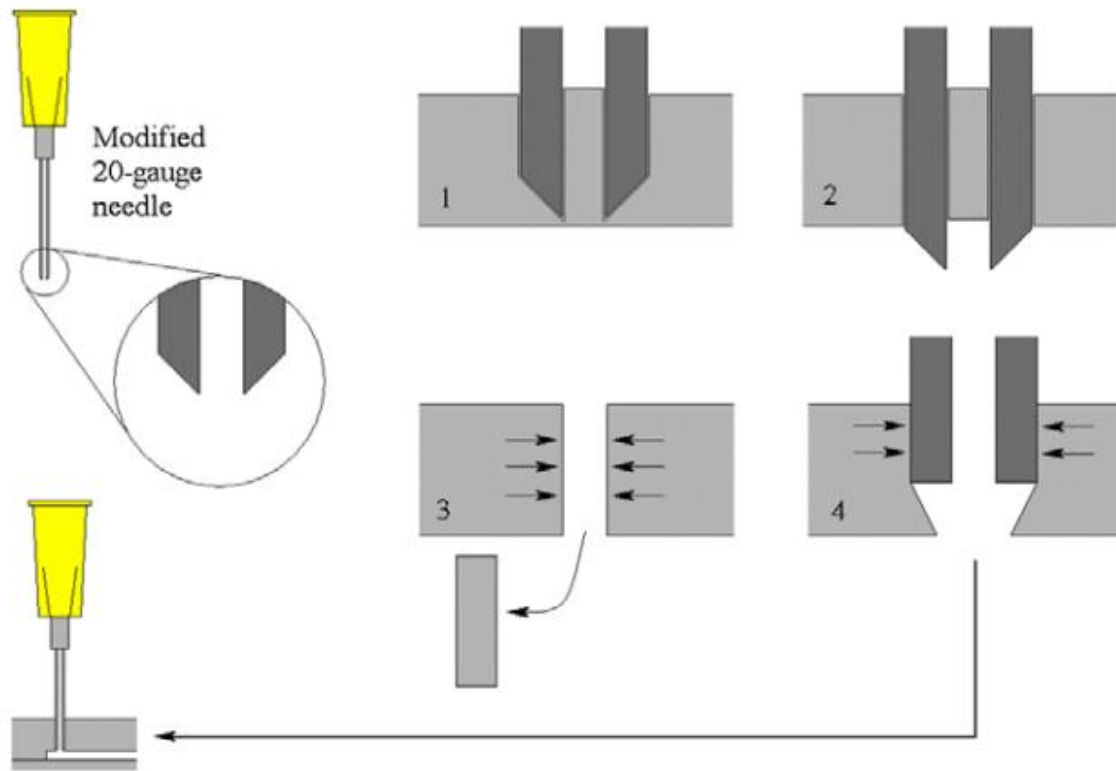
Figure 19 - Coring process for connecting PDMS channels to PEEK tubing. From (Christensen et al. 2005)

3.1.2.4 Device assembly

Once the base slide is coated with PDMS, and the ports are made in the PDMS mold, the device can be assembled. The custom slide allows for additional area compared to a standard microscopic slide, accommodating for 4-5 individual devices per slide. First the faces that are to be bonded are cleaned with scotch tape in order to ensure no particles will be bonded between the two surfaces. Next, the base slide and the molds are exposed to oxygen plasma for 100 seconds. Exposing PDMS to oxygen plasma develops silanol groups at the expense of methyl groups. The oxidation of the surface

layer increases the concentration of hydroxyl groups and this leads to the formation of strong intermolecular bonds (Garbassi et al. 1994). These bonds have been tested to last over 45 days (Kim et al. 2004). After exposure the molds are placed on the base slide, ensuring they are placed along the midline of the slide. If the molds are placed too far away from the midline of the slide, the device will not fit in the water jacket. The assembly process is shown in Figure 20.
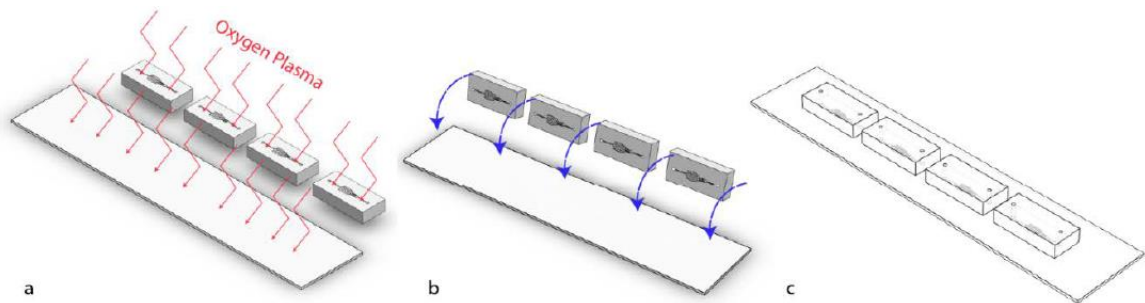
Figure 20 - Microfluidic device assembly: (a) the bonding face of the PDMS coating slide and the PDMS mold are exposed to oxygen plasma. (b) The pieces are bonded together. (c) Assembled device with four independent channels. From (Giannetti 2013)

3.1.2.5 Device Surface Treatment

Once bonding is completed, the channels are filled with 2-[METHOXY(POLYETHYLENEOXY)PROPYL] TRIMETHOXYSILANE (Silane) (tech 90, Gelest, Morrisville, PA). The channels must be completely filled to ensure successful surface treatment. This is done using a 50μl micropipette. The Silane sits in the channel for 30 minutes at room temperature, and the excess Silane is removed from the surface of the channel with a Kimwipe. While the silane sits in the channel, two different functional groups, poly(ethylene glycol) and amine are introduced onto the

PDMS surfaces for passivation of nonspecific protein absorption and attachments of biomolecules (Sui et al. 2006)). This Silane treatment modifies the surface of PDMS in order to decrease its permeability and deactivate its surface (Abate et al. 2008).

Once 30 minutes have passed, the channel is rinsed with de-ionized water 5-6 times to remove any unreacted Silane. Once all of the Silane is removed from the channel, the water must also be removed, and the device is cured once more at 65C for 12 hours to ensure the PDMS is now fully cured. Once curing is complete, the channels are to sit for another 12 hours in order to allow the channels to reach equilibrium. PDMS remains permeable to liquids and gases after curing, and organic solvents can cause it to swell significantly.

3.2 Particle Image Velocimetry

3.2.1 Equipment

The experimental equipment is based on a laser-camera setup. An inverted microscope (Nikon Eclipse TE2000-U, Nikon Corporation, Japan) with a 10x objective lens (NA=0.30 Plan Fluor; Nikon Corporation, Japan) and a 2048x2048 pixel CCD camera (12 bit, 4MP, TSI POWERVIEW Plus; TSI Incorporated, MN) provides the observation area of 1523x1523μm with a theoretical pixel length of 0.6583μm/pixel, and an optical resolution of 1.169 μm. For the μ-PIV, the volumetric illumination is provided by a dual pulse Nd:YAG laser (λ=532nm, Power=15mJ/pulse, Duration=4 ns, New Wave Laser Pulse Solo Mini; New Wave Research - ESI, Fremont, CA). The liquid phase is seeded by 1.0 μm fluorescent particles that have excitation/emission peaks at 535/575nm (Nile Red FluoSpheres; Invitrogen Corporation, CA). Therefore only the returning emission spectrum from the particles passed the dichroic filter

(λ>550nm) and reaches the camera. The camera and laser timing is controlled by a multi-channel synchronizer (Model 610035; TSI Inc., Minneapolis, MN). The μ-PIV system utilized in this study is depicted schematically in Figure 21.
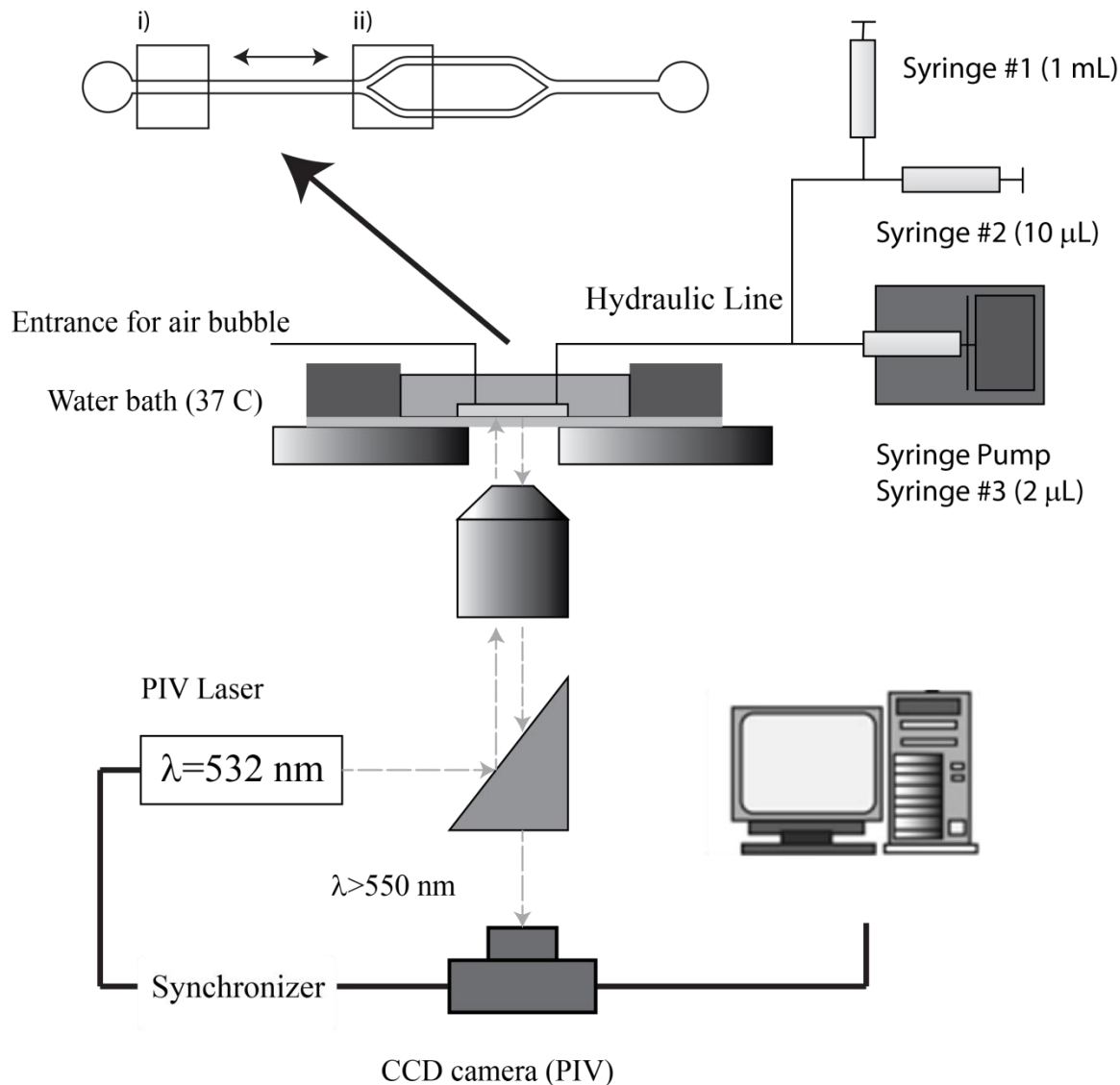
Figure 21 - Schematic of the μ-PIV data acquisition system. The system utilizes a monochrome camera, a laser, and an epifluorescent cube filter. i) Shows the position of the channel in the observation window when drawing the bubble into the channel. ii) Shows the location of the channel in the observation window during image acquisition.

3.2.2 Test Solutions

In a previous study done in our lab, solution functionality was examined to determine test solutions implemented in our microfluidic investigation (Dearden 2014). Surface tension measurements were taken with a micro-size Langmuir trough. The

Langmuir trough is composed of a rectangular trough and barriers that move laterally to compress the surface of the fluid in the trough, and a microbalance. A water bath was used to maintain a trough temperature of 37C throughout the experiments, and the solutions were maintained at this temperature as well to maintain physiological relevance.

The solutions we examined used Dulbecco's Phosphate Buffered Saline (DPBS) as a base buffer solution. The following test solutions were investigated.

- **Dulbecco's Phosphate Buffered Saline (DPBS):** This is a water-based buffer solution that contains C=0.1 mg/ml $CaCl_2$, which is required for sufficient pulmonary function. Since DPBS has no surface active agent, it has a high and constant surface tension of 70 dyn/cm, which is very close to the theoretical value of pure water which is 72 dyn/cm. This solution was used as a base buffer solution as well as a control.

- **Sodium dodecyl sulfate (SDS):** SDS is an anionic surfactant used in many cleaning and hygiene products. Since SDS molecule has a high diffusion rate near the air-liquid interface, its surface tension cannot be changed dynamically within our setting is low and nearly constant.

- Figure 22 demonstrates that when C=1.73 mg/ml, SDS can maintain the lowest surface tension (42dyn/cm) while avoiding the critical micelle concentration (Dearden 2014) .

- **Infasurf**: (calfactant) (ONY Inc., NY) an exogenous pulmonary surfactant analog used in surfactant replacement therapy.

- C= 0.01mg/ml: lower static surface tension than DPBS (37 dyn/cm), and has very dynamic surface tension

- C=0.1mg/ml: lower static surface tension than C=0.01 mg/ml (23dyn/cm), and has dynamic surface tension

- C=1mg/ml: similar hysteresis loop to C=0.1 mg/ml, but with more rapid absorption and a lower minimum surface tension.

Even though C= 0.1 and 1 mg/ml have very similar values for static and dynamic surface tension, the 1 mg/ml solution has more surfactant, which means that it can potentially change its surface tension much more quickly than C=0.1 mg/ml. How this affects airway reopening will be determined in this study. The dynamic surface tension properties of these solutions can be seen in Figure 23, and their static surface tension properties can be seen in Table 5.

Fluorescent particle with Nile Red was then added to our solutions for visualization. It has excitation/emission peaks combination at λ=535/575 nm. This emission spectrum was ideal for the combination with the LED red laser (λ=675nm) for the PIV (Yamaguchi et al. 2012). The particle size chosen is 1μm, and the particle concentration in each solution is .04% per unit volume. The particle size was chosen to be 1μm because of the pixel resolution of our observation window. The pixel resolution was previously measured to be .6583μm/pixel. Since each particle is slightly larger than one pixel, no matter its position, we can assure that the location of the particle is accurately measured. Particle seeding density was determined by trial and error using Poisseulle flow with the same methodologies described in (Liu et al. 2000) and (Meinhart et al. 1999). The

concentration was determined based on our interrogation window size (32x32 pixels with 50% overlap). A particle concentration of .04% was deemed acceptable for our purposes.

Table 5 - Solutions and their static surface tension values

Solution	Static Surface Tension (dyn/cm)
DPBS	70
0.01 mg/ml Infasurf	37
0.1 mg/ml Infasurf	23
1 mg/ml Infasurf	23
SDS	42
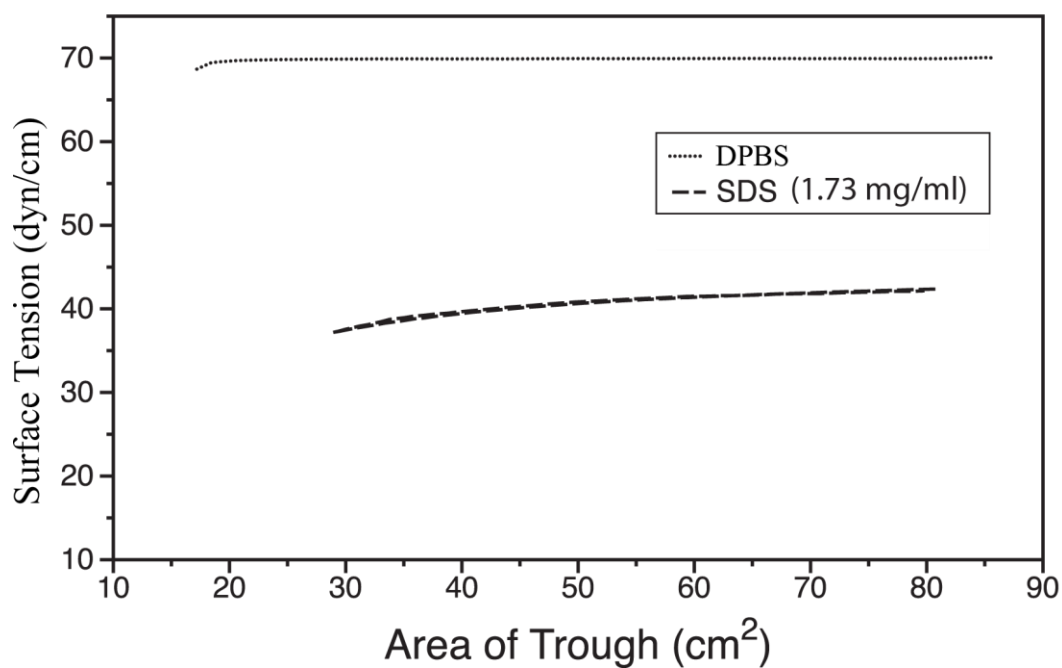
Figure 22 - Dynamic Surface tensions of DPBS and SDS (Dearden 2014)**.**

Effect of Surfactant Concentration
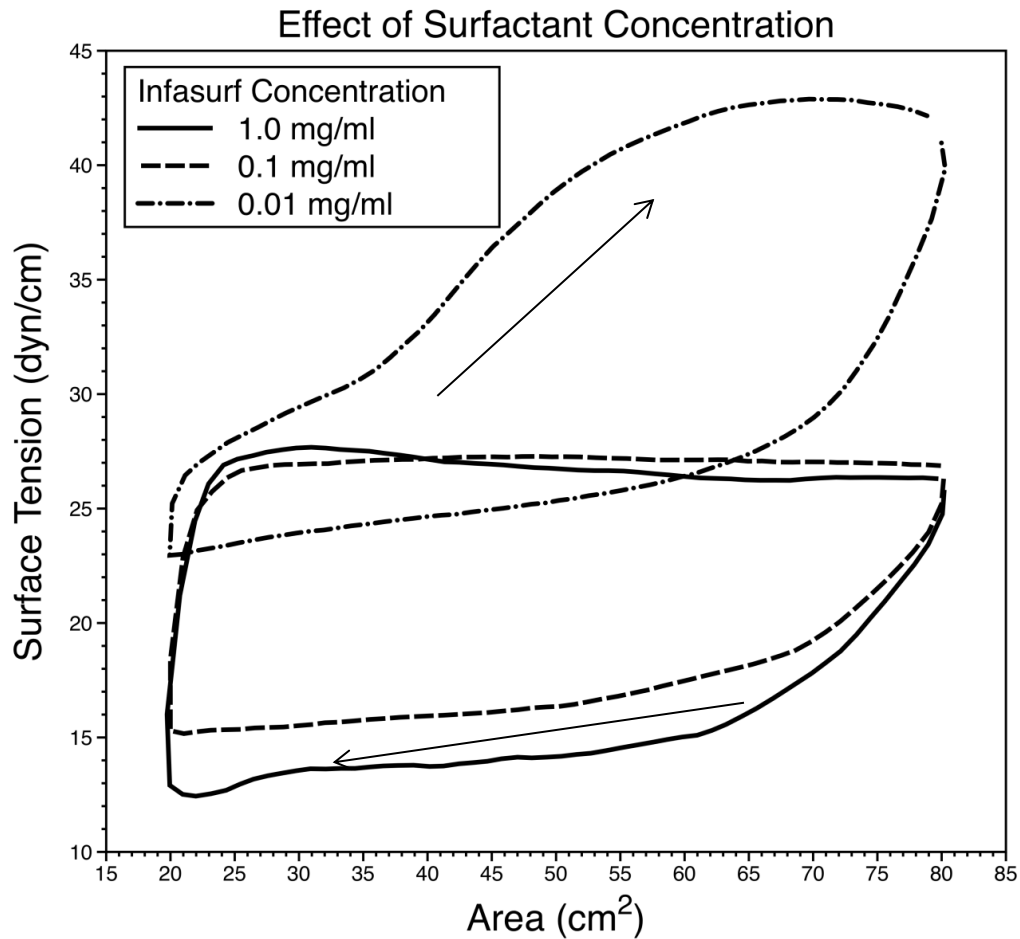
Figure 23 - Effect of surface area and surfactant concentration on surace tension (Dearden 2014)

3.2.3 Image Acquisition Preparation

The first step in ensuring that the PIV system is ready for image acquisition is to determine an appropriate interrogation window size. Based on our model, we determined that a 32x32 pixel interrogation window would be appropriate. Since the

daughter channels of our devices have an average width of 150μm, it was necessary to have enough interrogation windows to ensure measurement of u_{max} in the center of the channel. Since there are 1.52pixels/μm, there is an average of ~230 pixels in every daughter channel. With a 32x32 pixel with 50% overlap interrogation window, this ensures that there will be at least fourteen interrogation windows across the width of each daughter channel. This ensures approximately 7% margin of error for the determination of the center. Since the channels are longer than they are wide, this window size will also ensure that there are enough interrogation windows downstream in order to have an accurate measurement of u_{max}.

Once the interrogation window size is set, the flow rate of the syringe pump must be set. Since our desired bubble speed is 0.5 mm/s in the parent channel, the average area of the parent channel can be used to measure the necessary flow rate. The average area of the parent channels (taken from Figure 28) is 39,154μm^2. In order for the bubble to travel at a speed of 0.5mm/s in a 39,154μm^2 channel, a flow rate of 1.17μL/min is required.

Since the μ-PIV employs cross-correlation analysis, two separate fluorescence images separated by a very short period of time (Δt) are captured at every data acquisition point. For this to work properly, the solution should not move more than one quarter of the interrogation window (8 pixels or 5.26 μm) during Δt (Adrian 2005). Since u_{max} is known to be 1.075mm/s, Δt must be at least 4.89 ms for the parent channel. However since measurements are taken in the daughter channels, this value must be multiplied by 1.44. Therefore, Δt is set to 8ms.

Finally, once Δt has been determined the final parameter that has to be selected is the number of images per experiment. Since the image acquisition rate of this system is 7.25 images/sec, the number of images required in order to run a successful experiment can be determined easily. First, at least 10 images are required before the bubble tip hits the carina tip in order ensure that the flow is fully developed before reaching the carina tip, and to accurately measure the single phase flow of the two daughter channels. This is done to ensure that the flows in the daughter channels are behaving as they were designed to do. Since the bubble moves at 0.5 mm/sec, it can take up to 3 seconds for the bubble to fully propagate through the bifurcation. Therefore, 22 images are required in order to view the entire reopening process. Since the bubble cannot start at the same place every time, it takes a second or two for flow to fully develop, and the bubble tends to sit on the carina tip for a few images during every experiment, 80 images will be taken during each experiment in order to ensure everything is properly measured.

3.2.4 Image Acquisition

Once the microchannel has completed curing after surface treatment and rested for 12 hours, and all of the parameters for the μ-PIV/Shadowgraph system have been set, the experiment is ready. First, the slide is attached to the water bath and placed above the μ-PIV/Shadowgraph system. Next it is connected to the syringe pump system. Two flexible plastic tubes are used to connect the channel to the glass tubes that connect with the syringes and to the air in the room in order to pull the semi-infinite bubble. The glass tubes are not used to directly connect to the channel because they are too rigid and apply

stresses on the channel that causes them to unseal the channel. However, they are used for the rest of the system to ensure that as much of the hydraulic line is as rigid as possible. This is done so that there is no stretching or compressing in line diameter to keep the flow as steady as possible. Figure 24 shows the water bath in position and the plastic tube used to connect the channel to the syringe pump system. Once the bifurcation is in the field of view of the μ-PIV and connected to the syringe pump systems, the image is focused at the center of the channel. It is important that the images are focused at the center in order to ensure the true u_{max} is measured. Once the image is focused properly, Syringe #1 is filled with the desired solution, connected to the glass tubes, and the channel is filled. If surfactant is in the solution, it is important that the water bath is filled with deionized water and heated to 37C. Once the channel is filled, and the solution is heated to 37C (if necessary), a bubble is pulled first with syringe 1 until it is near channel. Once the bubble is near the channel, it is pulled with syringe 2. This syringe is 100 times smaller than syringe 1 and allows for much more precise bubble control. Syringe 2 is used until the bubble is near the carina.

If the bubble position is unstable, it is left to stabilize. However, if it does not stabilize, there is air trapped in the syringe pump system somewhere, and the entire system needs to be flushed. This is repeated until the bubble position is stable. Once the bubble position is stable, it is near the carina tip, and the bifurcation and part of the downstream of the channel is in the field of view of the camera, it is time for image acquisition. Figure 25 is an example of correct channel position for successful image and data acquisition.
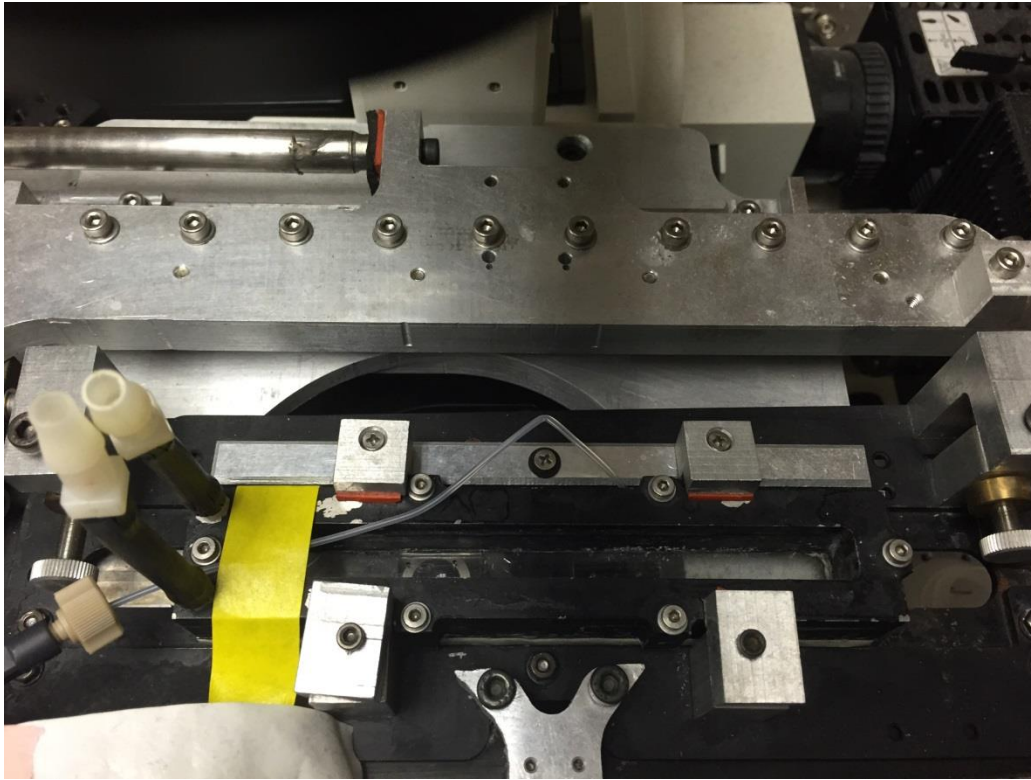
Figure 24 - Water bath in place above μ-PIV/Shadowgraph system and plastic tubing used to connect channel to syringe pump system

Once the channel is ready for image acquisition, the lights in the room are turned off, images are taken and saved and the syringe pump is turned on until image acquisition is over.

3.2.5 Image Analysis and Data Acquisition

Data acquisitions from Figure 25 were performed to acquire five usable experimental trials. Trials were accepted when the bubble tip hit the carina tip after at least 10 images and continued to progress for 22 more images. This way, accurate measurements of single-phase downstream flows could be measured to ensure the

channel design had the desired u_{max1}/u_{max2} value, and a complete reopening of the bifurcation could be observed. The time was set to t=0 when the bubble tip first reaches the carina tip (as seen in Figure 25).

Velocities are estimated by the correlation of particles in the focal plane. The region that is measured is called the vector correlation depth, and relates to the depth of the focal plane and the size of the particle (Liu et al. 2000). With our system, the depth of the vector correlation is approximately 15 μm; therefore, the focal plane was adjusted to the midpoint depth of the rectangular channel in order to capture the maximum velocity of the daughter channels. An exact solution of fully developed pressure-driven viscous flow in a square or rectangular channel is given as:

$$u_{(y,z)} = \frac{H^2}{\mu}\left(\frac{\partial P}{\partial x}\right)\left[1 - \left(\frac{y}{H}\right)^2 - \frac{4}{\pi^3}\sum_{n=0}^{\infty}\frac{(-1)^n}{(n+1/2)^3}\frac{\cosh\left\{\left(n+\frac{1}{2}\right)\pi\frac{z}{H}\right\}}{\cosh\left\{n+\frac{1}{2}\pi a\right\}}\cos\left\{\left(n+\frac{1}{2}\right)\pi\frac{y}{H}\right\}\right] \quad (8)$$

$$u_{max(y=0,z=0)} = \frac{-H^2}{2\mu}\frac{dP}{dx}\frac{4}{\pi^3}\sum_{n=0}^{\infty}\frac{(-1)^n}{\left(n+\frac{1}{2}\right)^3}\frac{1}{\cosh\left\{\left(n+\frac{1}{2}\right)\pi a\right\}} \quad (9)$$

where 2H is the channel depth and 2aH is the channel width in the measurement region. Solving for $\frac{dP}{dx}$ in Equation (9), it can be substituted into Equation (8) in order to solve for the velocity profile in terms of u_{max}. A computer simulation was used in order to model this equation with different values for a in order to calculate different values of b in Equation (10) (Binous 2007). The results from this model can be seen in Table 6.

$$u_{max} \simeq b \cdot u_{avg} \quad (10)$$

Table 6 - Channel cross section dimensions and a & b values

Channel Cross-Section Dimensions (µmxµm)	a	b
140x150	0.933	2.123
145x150	0.967	2.120
148x150	0.987	2.117
150x150	1.000	2.116
152x150	1.013	2.114
155x150	1.033	2.112
160x150	1.067	2.111
250x150 (parent channel)	1.667	2.025
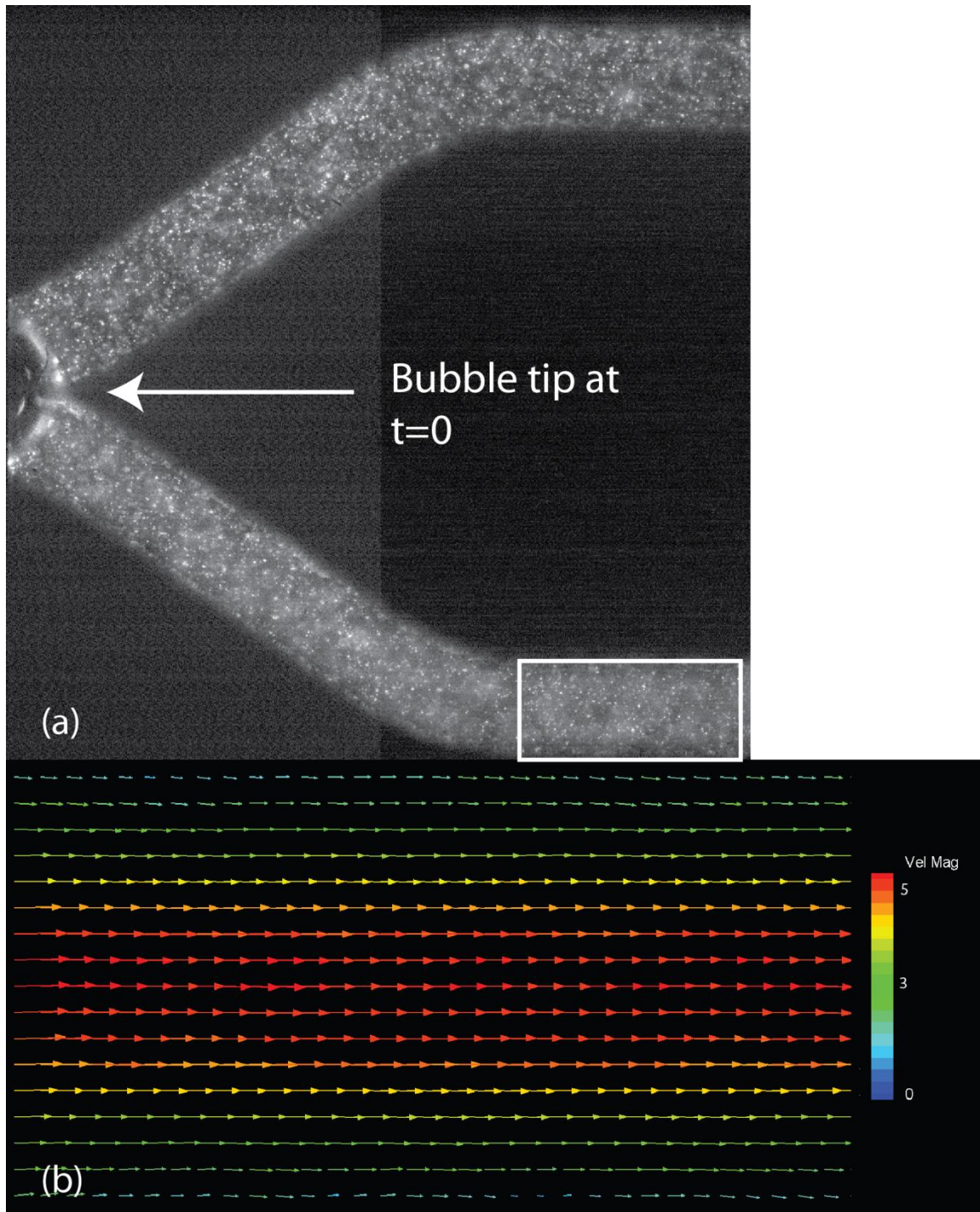
Figure 25 – (a) Correct channel position for successful image acquisition, and bubble position at t=0. The square in the bottom right represents all of the interrogation windows. (b) Measured velocity profile of downstream channel.

Chapter 4: Results

First, in this section the geometries of each microfluidic device that was constructed will be measured in order to determine whether it accurately reflects the designed model. Once the geometries of the microfluidic devices have been confirmed, we will go through the process of the imaging analysis. Finally, we will look at the reopening profiles of each model with up to 5 different solutions in order to ultimately determine whether or not pulmonary surfactant is capable of reopening both daughter channels of an asymmetric bifurcation.

4.1 Microfluidic Studies

In this section the geometries of each fabricated channel will be measured in order to determine if it accurately reflects the designed model. Various bonding methods will also be explored in order to ensure the strongest bond possible between the PDMS channel and the PDMS covered test slide.

4.1.1 Microfabricated Master Wafer

Once the correct duration of exposure was determined, a more uniform and geometrically accurate photoresist was obtained after the soft baking process. If the photoresist is underexposed, the negative of the channel will be much thinner at the bottom than it is at the top. This will cause the channel's cross-sectional area to be smaller than desired and cause the bubble to move faster than anticipated. It also creates rough walls along the channel, which can affect the reopening of the microchannel. If the

photoresist is overexposed, there channel cross-section will have a sharp, wider area at the top, and the channel walls will be slightly curved. This causes the channel to be wider than anticipated, and cause the bubble to move slower. The result of proper and improper exposure time can be seen in Figure 26. The resultant master wafer of proper exposure is depicted in Figure 27.
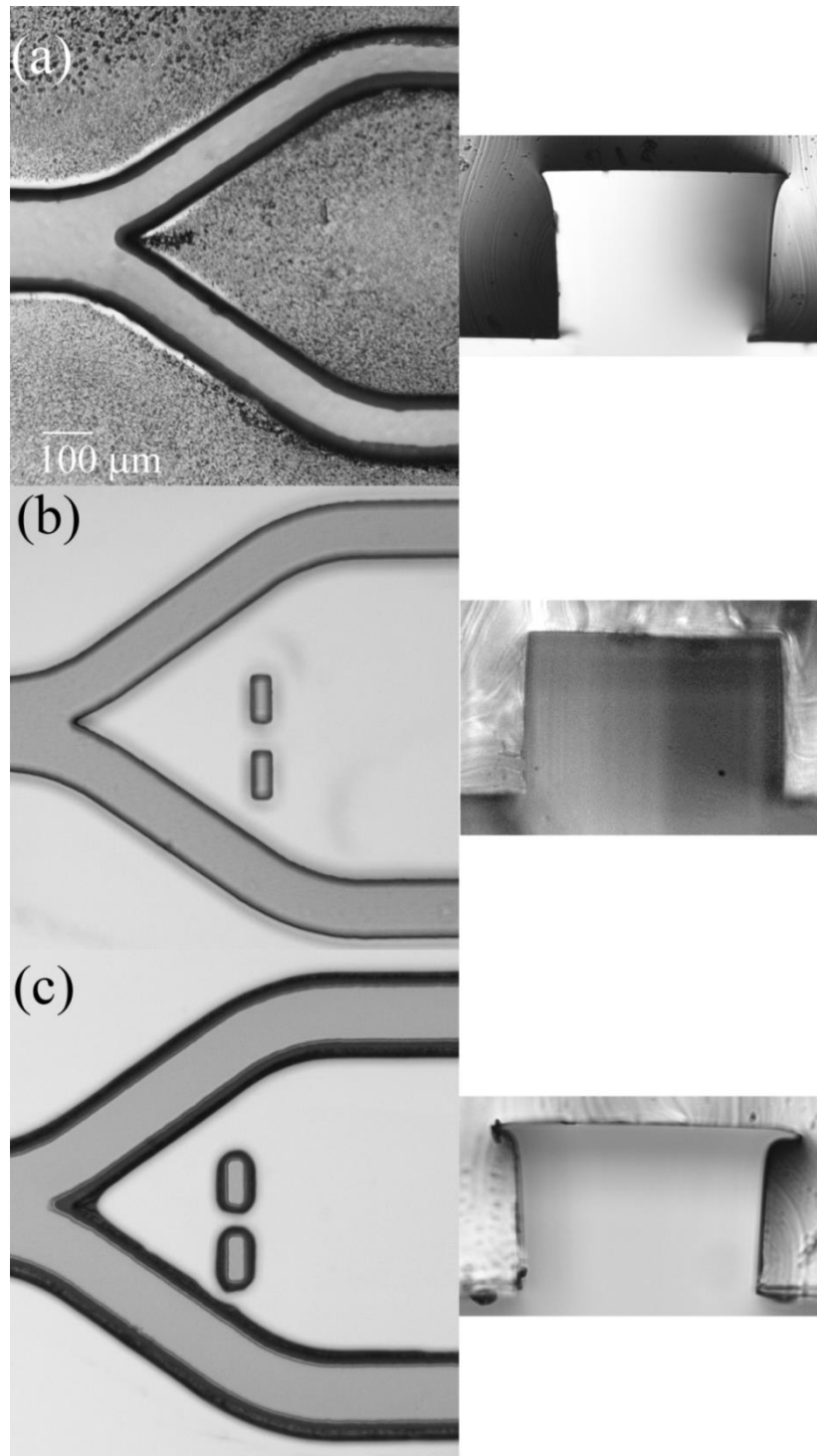
Figure 26 - Effect of proper and improper exposure on channel geometry. (a) Insufficient exposure causes curved walls. (b) Proper exposure causes straight walls. (c) Overexposure causes jagged edges at top of channel cross section.
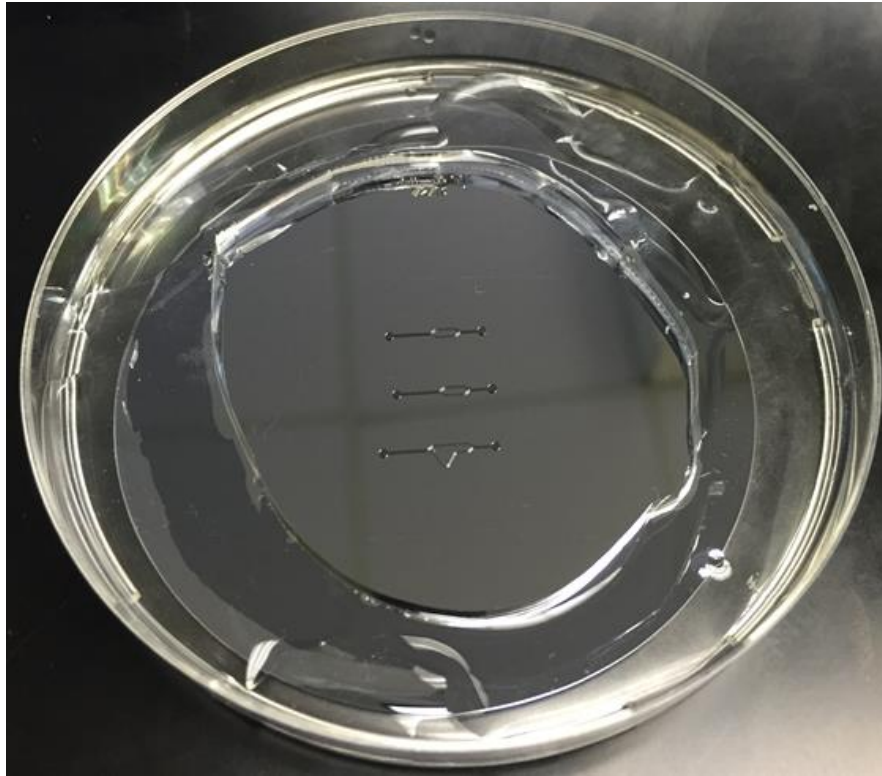
Figure 27 - Microfabricated master wafer

This study determined that acceptable depths only occur within r/R<.45 (R=width of the wafer). For this reason there are only three channels on each wafer. However, in order to ensure that an acceptable channel cross sectional area was actually acquired the cross sectional area of all of the channels was measured. The intended channel depth from this wafer was 150μm. In order to measure the height of each channel, cross-sections of the parent channel were cut from various distances from the center of the wafer. Once this was done, the height was measured using the number of pixels, and the measured pixel length of .6583μm/pixel. The results of these measurements can be seen in Figure 28.
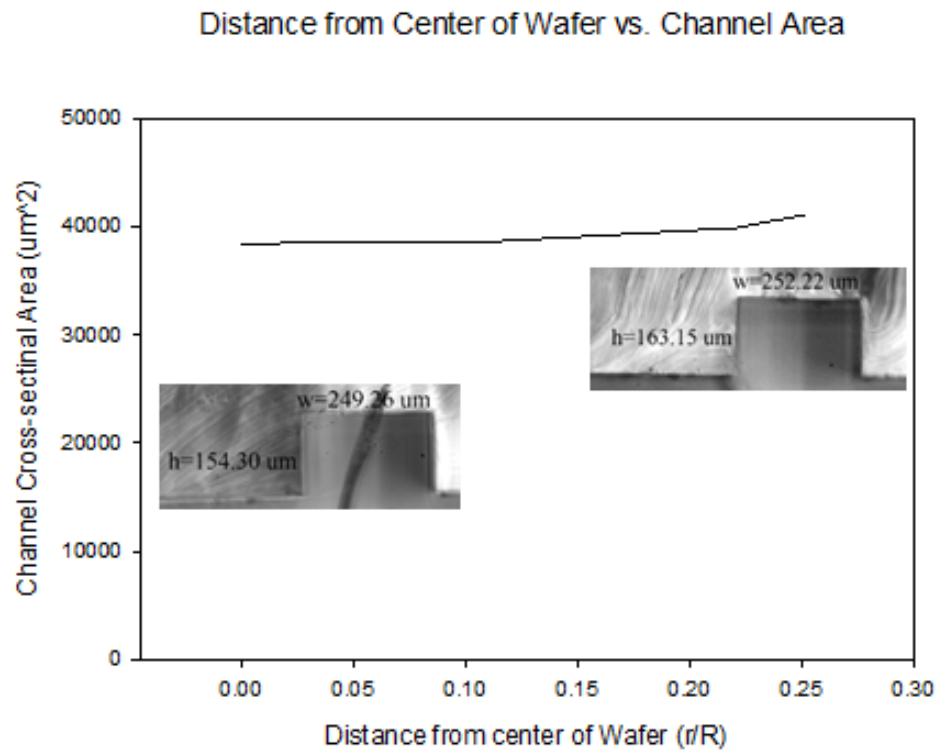
Figure 28 – Parent channel cross-sectional area as a function of radial position of wafer. Area varies more further from r=0, but this variation is less than 5%.

Even though the area of the channels varies slightly the larger r becomes, this error does not surpass 5%. Therefore the change in area will not have a significant effect on maximum velocities within the channels during experiments. Once it was determined that the height of the channels was consistent within r/R > .45, it was necessary to measure all of the features for each channel design. The result of these measurements can be seen in Table 7.

Table 7 - Measured features of channel

Channel	Designed Daughter Diameter	Actual Daughter Diameter	Designed Carina tip offset (μm)	Actual Carina tip offset	Designed theoretical u_{max1}/u_{max2}	Calculated u_{max1}/u_{max2}	Percent error u_{max1}/u_{max2}
αA_1	160	160	-10	-10	1.143	1.134	.79
αA_2	140	141					
αB_1	160	148	+10	+10	1.143	1.164	1.8
αB_2	140	128					
αC_2	150	140	0	0	1.143	1.134	.79
αC_2	150	141					
αD_1	160	155	0	0	1.143	1.168	2.1
αD_2	140	133					
βA_1	155	151	-5	-8	1.069	1.056	1.2
βA_2	145	143					
βB_2	155	155	+5	+7	1.069	1.069	0
βB_2	145	145					
βC_2	150	148	0	0	1.069	1.069	0
βC_2	150	148					
γA_1	152	152	-2	+2	1.027	1.027	0
γA_2	148	148					
γB_1	152	153	+2	-2	1.027	1.027	0
γB_2	148	149					
γC_1	150	150	0	0	1.027	1.027	0
γC_2	150	150					

Even though the overall dimension of the β series appears accurate, the radius of curvature of the carina tips for all 3 β models have a much larger radius of curvature than designed. We will discuss how this affects reopening later.

Once the actual dimensions of the channels were determined, it was necessary to calculate how the actual dimensions of the channels will affect the theoretical values of u_{max1}/u_{max2}. The first step was to calculate the hydraulic diameter of each daughter channel using their measured height and widths. Since the two daughter channels were 1mm apart, their heights were the same. For this reason, their heights were held constant

at 150μm. This was possible because the maximum height measured in the daughter channels was 155μm and altered the calculated u_{max1}/u_{max2} by less than .001 from the value of u_{max1}/u_{max2} using a height of 150μm. Once the hydraulic diameters were all calculated for each channel, the values for u_{max1}/u_{max2} for each channel were calculated using Equation (6).

Next, the percent error of u_{max1}/u_{max2} was calculated. Since the error only exceeded 2% for one of the channels, and never exceeded 3%, these channels successfully portray our model.

4.1.2 Device Assembly

Once it was determined that the master wafer satisfied the desired requirements, it was important to ensure that the bond between the PDMS mold and the slide were strong enough to endure the pressure and stresses involved with running a successful experiment. The previous method used was not strong enough to endure such stresses. The original method involved completely curing the PDMS mold and the spin coated bottom slide for 4 hours each at 65C, then exposing both the mold and the slide to oxygen plasma for 100 seconds. Once the plasma exposure was finished, the molds were placed on the slide, the channel was treated with Silane for 30 minutes, and the channels were cleared with water and simply let to sit for 24 hours. This method was replaced with a new one that did not completely cure the PDMS before the plasma exposure and completed curing after surface treatment as explained in 3.1.2.2-5. This new method allowed us to run at least five experiments with all five solutions without beginning peel

off, while the old method only allowed for up to 5 runs with each channel before beginning to peel off. Figure 29 shows the mold peeling off of the slide, and water leaking out of the channel and into the area where there should still be a bond.
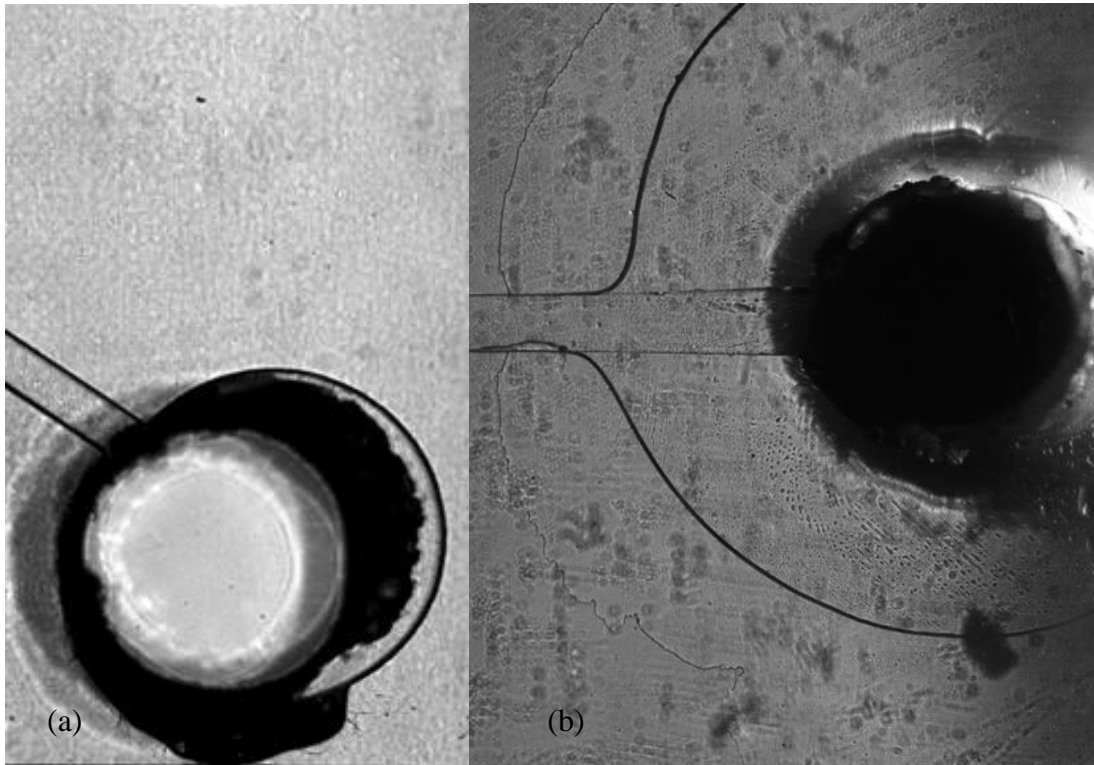
Figure 29 - Effect of weak plasma bonding and channel leaking. (a) A strong connection where no fluid is leaking out of channel. (b) A weak bond where the mold and the slide have separated and allowed the fluid to leak out of channel.

During this experiment, various cure times were attempted and curing for more than one day had adverse effects on the master wafer. If the PDMS is left to cure for more than one day, the PDMS will begin to bond to the master wafer, altering the geometry of the master wafer and ultimately the channel. This, in turn, rendered the master wafer useless. The result of severe overcuring can be seen in Figure 30.

Figure 30 - Effects of severe overcuring. PDMS has bonded to the wafer and severely altered the channel geometry

4.2 Particle Image Velocimetry

Once the images have been acquired, the first step is to ensure that sufficient fluorescent microparticles are in the test solutions and that the excitation light sufficiently excites the particle. This can be easily done by visually examining one of the images acquired during one of the experiments. In order for the flow field to be accurately measured, clear particles must be discernable throughout the image. An example of a good fluorescent image can be seen in Figure 25a.

4.2.1 Data Processing

Once the image has been successfully approved, the image analysis process begins. The general process for data analysis of images will be demonstrated in sections 4.2.1.1-4 by the data from Channel αA with DPBS Solution. The steps include

1. Continuous data acquisition of down-stream u_{max}.

2. Using Equation (10) to convert the experimentally obtained u_{max} values to determine u_{avg}.

3. Determine the mean u_{avg} at each time point $\Delta t = .14$ seconds for the 5 runs.

4. Integrate the mean u_{avg} reopening profile in order to estimate the bubble tip propagation pattern as a function of time.

4.2.1.1 Continuous Data Acquisition of Down-stream u_{max}.

The downstream flow-rate is monitored by performing a continuous data acquisition of u_{max}. The two dimensional down-stream velocity profiles can be seen in Figure 25b. This process is done for each image during each of the five experiment runs. Once the instantaneous flow fields of all the images for all five runs have been created, it is necessary to ensure that none of the u_{max} values surpass 8 pixels (25% of the interrogation window). Accuracy of the PIV measurements become inaccurate if the displacement of the particle surpasses 25% of the interrogation window during Δt (Adrian 2005).

4.2.1.2 Convert the Experimentally Obtained u_{max} Values to Determine u_{avg}.

      If the measurements are accurate, the values for u_{max} are used to find u_{avg} using Equation (10). The value for u_{avg} can be used to represent the velocity of the bubble tip since the solutions in our model are incompressible. The average velocities for five experiment runs in daughter channels 1 and 2 for channel αA can be seen in Figure 31.
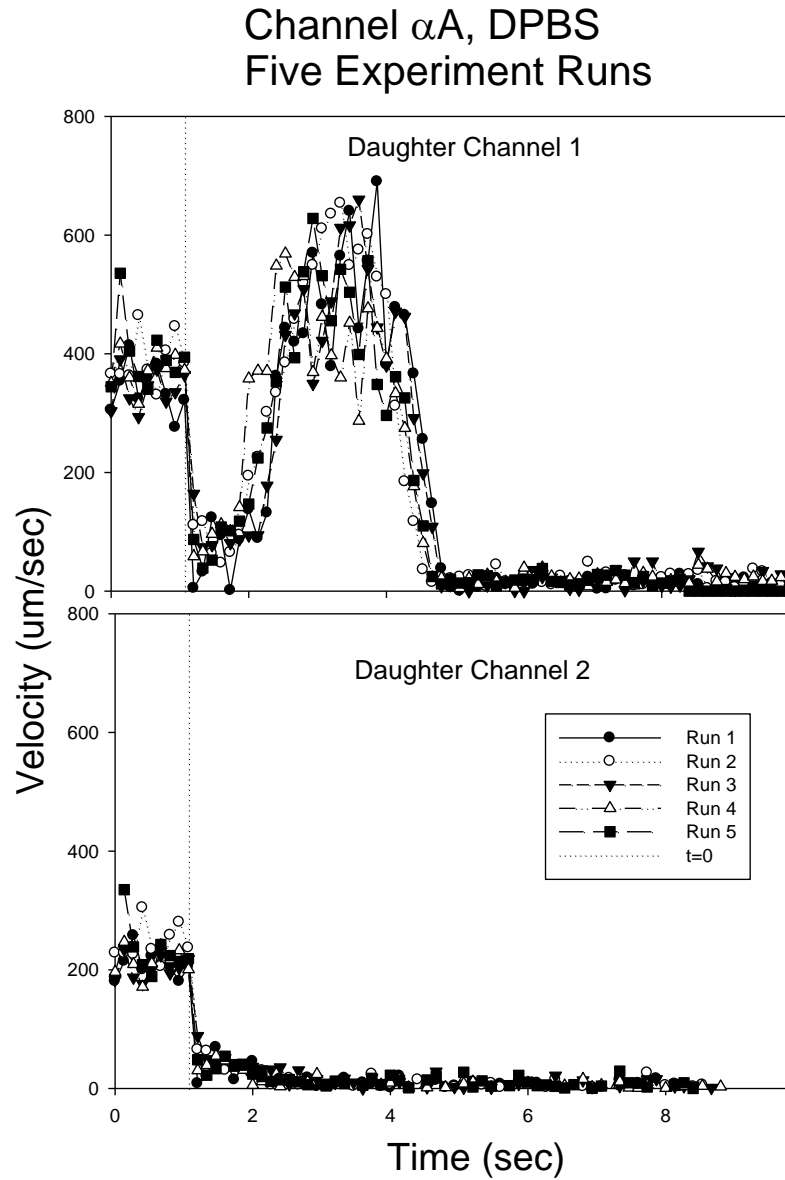
Figure 31 – μ-PIV flow velocity data as an interface propagates into Channels αA1 and 2. u_{avg} is the average velocity in each daughter channel. t=0 is defined as the time when the bubble tip first reached the carina, which can be found by a sudden velocity drop due to need to decrease in pressure in order to reach the yield pressure

Figure 31 shows that the instance when the bubble first touches the carina tip can be easily located because by a sudden drop in velocity. This drop in velocity is the need to decrease the pressure to reach the yield pressure necessary to cause the interface to move to the daughter airways. This was confirmed by investigating the image of that instance. Every time there was a sudden drop in velocity (Figure 31), the bubble had just reached the carina. We define t=0 to the time when the bubble tip first touches the carina tip (Figure 34 - Figure 40). The u_{avg} values that occur while the interface is in the parent airway is used to calculate u_{max1}/u_{max2} since these values represent the single phase flows in the daughter airways. The results of these measurements can be seen in Table 8.

Table 8 - Measured u_{max1}/u_{max2} values for each design (refer to Figure 14 for nomenclature standards)

Channel	Designed u_{max1}/u_{max2}	Measured u_{max1}/u_{max2}
αA	1.143	1.225
αB	1.143	1.193
αC	1.143	1.195
αD	1.143	1.148
βA	1.069	1.121
βB	1.069	1.100
βC	1.069	1.061
γA	1.027	1.040
γB	1.027	1.031
γC	1.027	1.030

Once t=0 has been set, it is important to properly determine when the experiment ends. When looking at the five runs, the top channel appears to begin to slow down when time approaches 4 seconds.   However this actually occurs because the bubble is entering the interrogation windows. Since the bubble is entering the interrogation window, there is no particle for the PIV, and the vector analysis will put a zero vector in its place.

Therefore, once u_{avg} of the five runs begins to steadily decline, the experiment is over and the later data points are not valid. The invalid data points at the end of the experiment have been excluded in Figure 32. Again, the data points before t=0 are used to measure u_{max1}/u_{max2}.

4.2.1.3 Mean u_{avg} at Each Time Point for the 5 Runs

Once the end of experiment has been determined, the mean u_{avg} for each time point $\Delta t=.14$ seconds for the 5 runs. The result of this can be seen in Figure 32.

72
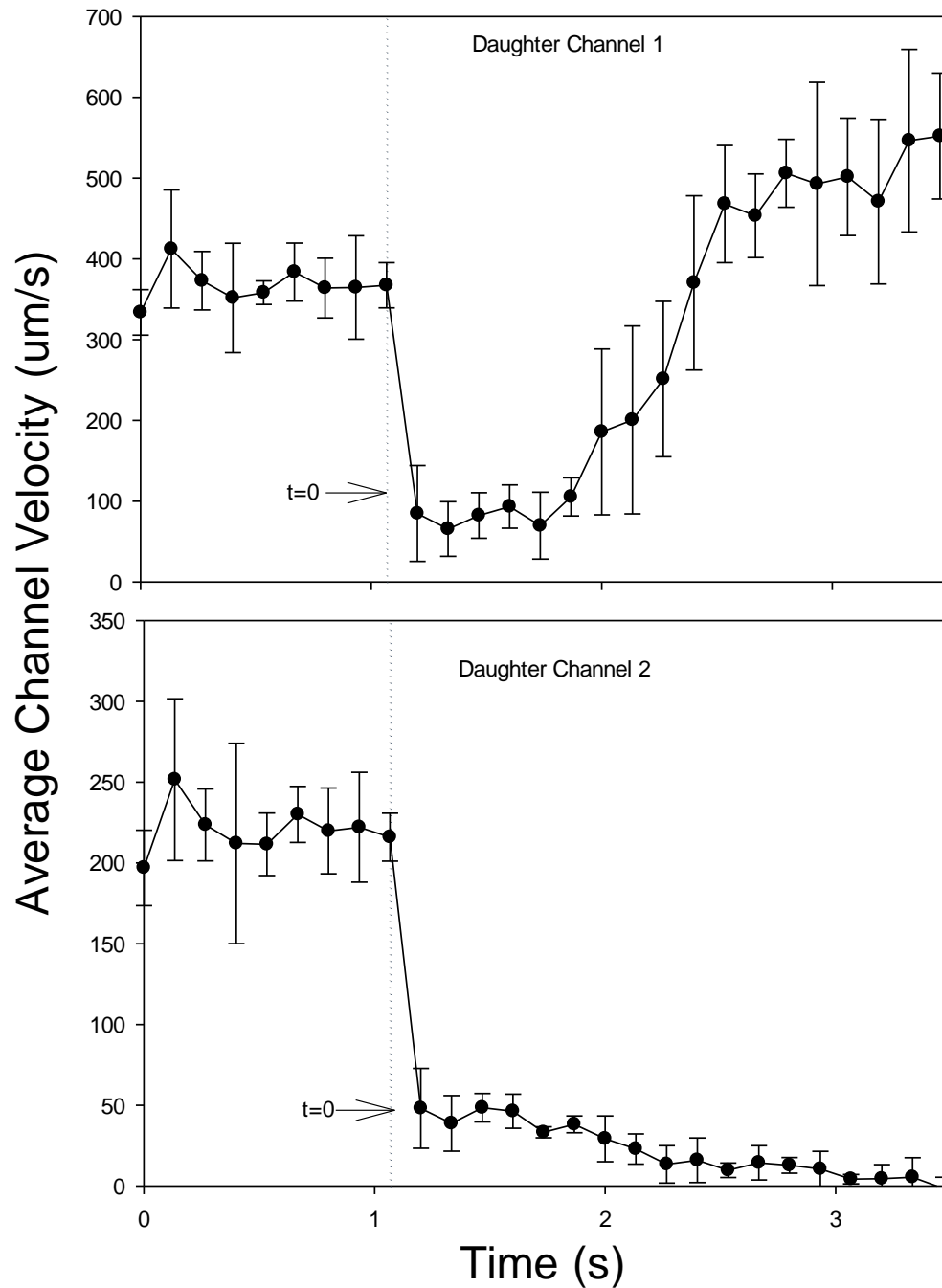
Figure 32 – Average down-stream velocities of channels αA1 and 2 with DPBS for five runs. In this particular model, the capillary and hydraulic pressure differences between Channels 1&2 are large. Therefore the bubble only propagates in Channel 1

73

4.2.1.3 Integration

After the average reopening velocity profile of the five runs has been determined, the mean u_{avg} values are numerically integrated in order to measure the location of the bubble tip once it touches the carina tip. At t=0, the bubble tip is touching the carina, which is also position 0. The results of this integration can be seen in Figure 33.

Channel αA, DPBS
Bubble Tip Location
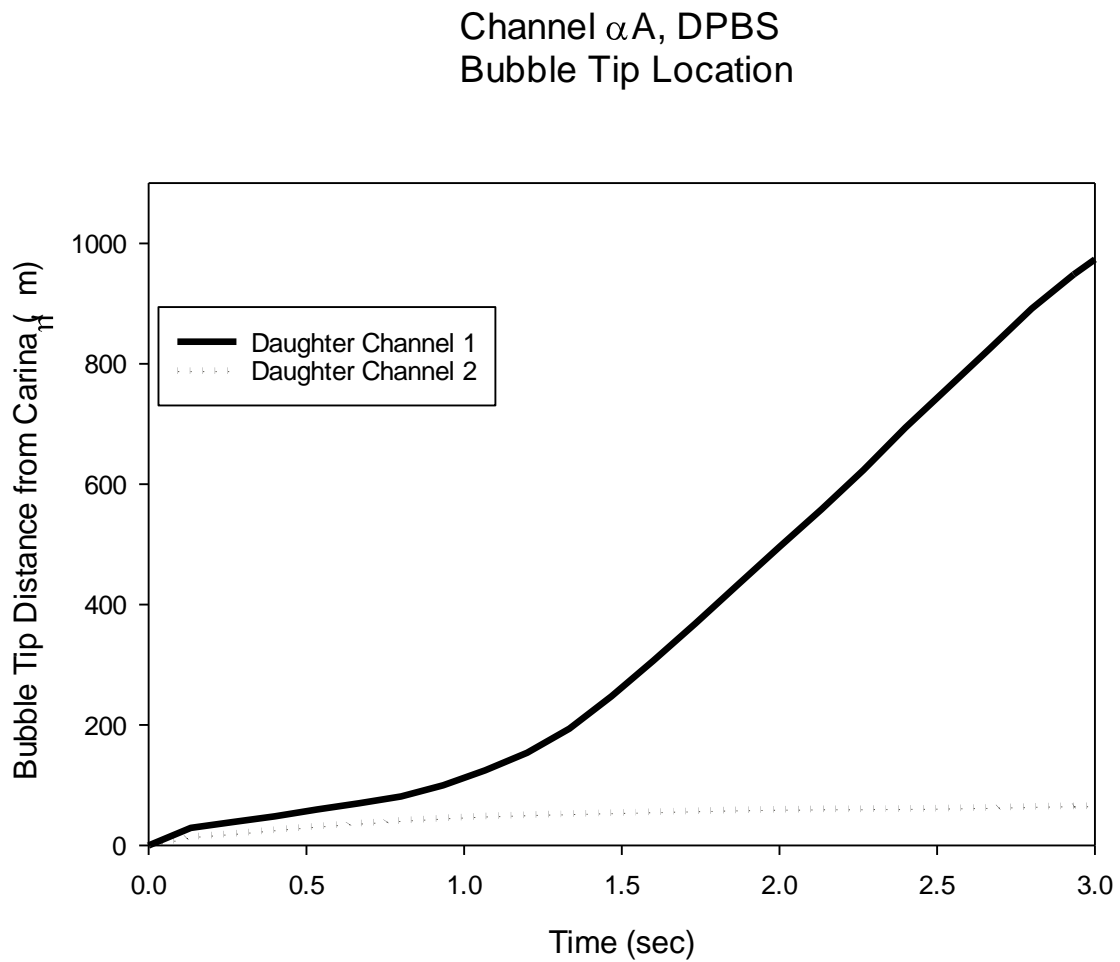
Figure 33 - Bubble Tip distance from Carina vs. Time for Model αA with DPBS.

4.2.2 Sources of Error

Now that we have estimated values for where the bubble tip is when the experiment ends, we can compare this to where the end of the experiment should occur. In Figure 33, the propagation of the bubble begins to substantially slow down once it reaches 1100μm. The distance from the carina to the beginning of the vector interrogation window was measured to be 1200μm, which is very close to our measured value. The error between calculated and measured values can come from three assumptions that were made: bubble speed and u_{avg} are equal, the location where u_{max} was measured may not have been the exact channel center, and 7.25 images/second is a fast enough image acquisition rate to numerically integrate u_{avg} to calculate the bubble position. Therefore, we estimate a ~10% error in prediction.

Assuming that the bubble speed and downstream u_{avg} are equal may lead to errors when calculating the bubble position. When the bubble travels down the channel, there is a resistance layer of solution that remains between the propagating air bubble and the channel wall. Even though this layer is very thin, it may cause the bubble to be slightly further down the channel than was calculated.

Assuming u_{max} was measured in the exact middle of the channel may also lead to errors when calculating the bubble position. Even though this is possible, this assumption is very reliable. Since there are at least fourteen interrogation windows across the width of each daughter channel, the likelihood of measuring u_{max} at the channel center is very high. This means that there is one interrogation for every 11μm. Therefore

75

there will always be an interrogation window ± 5μm. The difference in velocity between the centerline and ± 5μm in a rectangular channel is less than 1%. Therefore, unless the interrogation window is severely misplaced and is not near the centerline, this assumption will hold.

The final assumption that was made that could introduce errors in our calculations was that 7.25 images/sec is a fast enough image acquisition rate to numerically integrate u_{avg} to calculate the bubble position. Since the bubble approximation uses the trapezoid rule to estimate its location between images, there will be some error if the actual velocity graphs have a lot of curvature between images. This, however, is not likely since we are dealing with steady flows, and, since this image acquisition rate is the fastest possible with our current PIV system, nothing can be done to improve this frame rate.

The relative bubble positions in the two daughter channels can be seen in Figure 34 - Figure 43.

Figure 34 – Average bubble propagation patterns for Daughter Channels 1 and 2 for Channel αA (different daughter channel widths 160μm, 140μm) with all solutions. In this model, the capillary and hydraulic pressures are different in each channel. <u>DPBS</u>: ~0.5 second pause in transition area, Channel 1 then quickly opens while bubble in Channel 2 halts. <u>C=0.01mg/ml Infasurf</u>: ~0.75 second pause in transition area, Channel 1 then quickly opens while bubble in Channel 2 halts. <u>C=0.1mg/ml Infasurf</u>: ~1.25 second pause in transition area, Channel 1 then quickly opens while bubble in Channel 2 halts. Bubble does not propagate as far in this model due to longer pause in transition period. <u>C=1mg/ml Infasurf</u>: no pause in transition area, Channel 1 quickly opens while bubble in Channel 2 halts. Surfactant is unable to create a symmetric reopening profile in this model; there is a limit to what Infasurf can do.
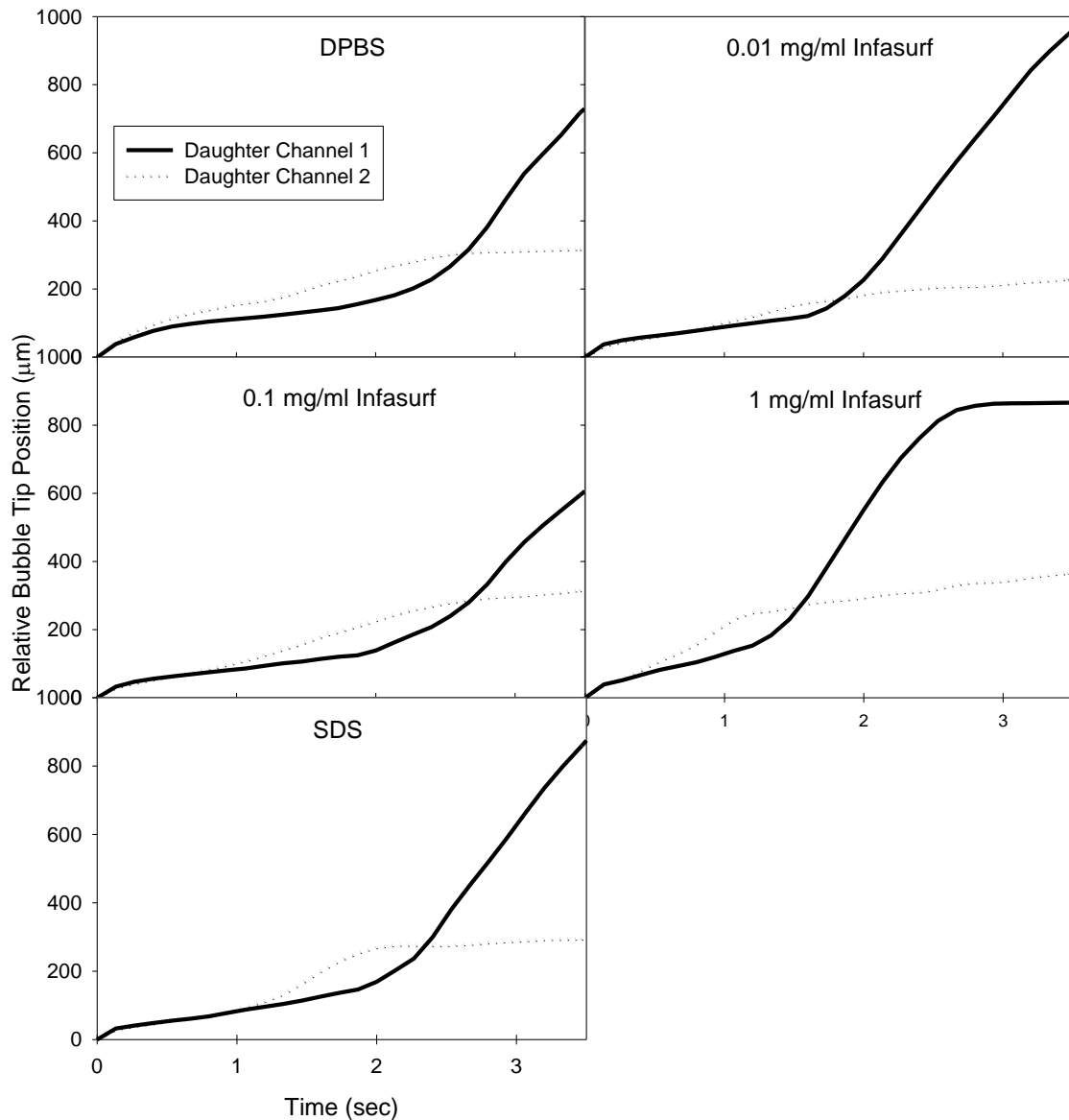
Figure 35 - Average bubble propagation patterns for Daughter Channels 1 and 2 for Channel αB (different daughter channel widths, 160μm, 140μm, moved carina tip to 10μm above center of parent channel) with all solutions. In this model the local capillary pressure at the carina tip is smaller in Channel 2, causing it to open first. It will halt once it passes the transition area, and Channel 1 will then begin to fully open. <u>DPBS</u>: Channel 1 leads for ~2.5 seconds before Channel 1 quickly catches up. <u>C=0.01mg/ml Infasurf</u>: Channel 1 leads for ~1.75 seconds before Channel 1 quickly catches up. <u>C=0.1mg/ml Infasurf</u>: Channel 1 leads for ~2.75 seconds before Channel 1 quickly catches up. <u>C=1mg/ml Infasurf</u>: Channel 1 leads for ~1.5 seconds before Channel 1 quickly catches up. <u>SDS</u>: Channel 1 leads for ~2.25 seconds before Channel 1 quickly catches up.

Figure 36 - Average bubble propagation patterns for Daughter Channels 1 and 2 for Channel αC (same width, different length, $L_2=1.1.143L_1$) with all solutions. In this model the hydraulic pressures are the same in both daughter channels, but differ in hydraulic pressures. Daughter Channel 1 always opens first because it has less resistance, but Daughter Channel 2 never halts because of the same capillary pressures. <u>DPBS</u>: Channels open symmetrically for ~1 second before Channel 1 takes lead. <u>C=1mg/ml Infasurf</u>: Channels open symmetrically for ~.75 seconds before Channel 1 takes lead. <u>SDS:</u> Channels open symmetrically for ~1.25 seconds before Channel 1 takes lead.

Figure 37 - Average bubble propagation patterns for Daughter Channels 1 and 2 for Channel αD with all solutions (different daughter channel widths, 160μm, 140μm, moved carina tip to center of parent channel) with all solutions. In this model the local capillary pressure at the carina tip are equal, causing both channels to open symmetrically. Channel 2 will halt once it passes the transition area, and Channel 1 will then begin to fully open. <u>DPBS</u>: Channels open symmetrically for ~1 second. <u>C=0.01mg/ml Infasurf</u>: Channels open symmetrically for ~1.25 seconds. <u>C=0.1mg/ml Infasurf</u>: Channels open symmetrically for ~1.25 second. <u>C=1mg/ml Infasurf</u>: Channels open symmetrically for ~1.25 seconds. <u>SDS</u>: Channels open symmetrically for ~1.25 seconds.

80
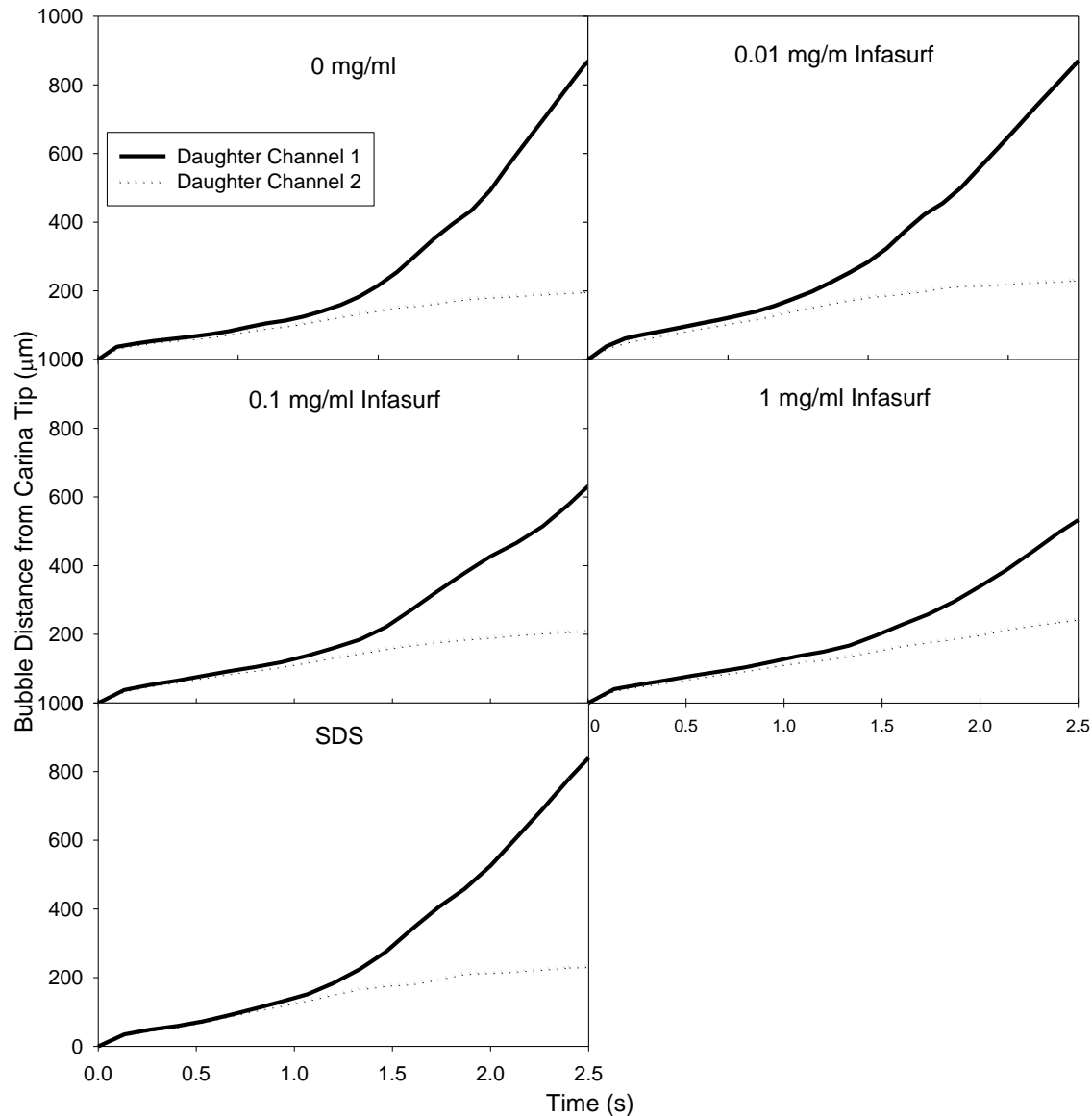
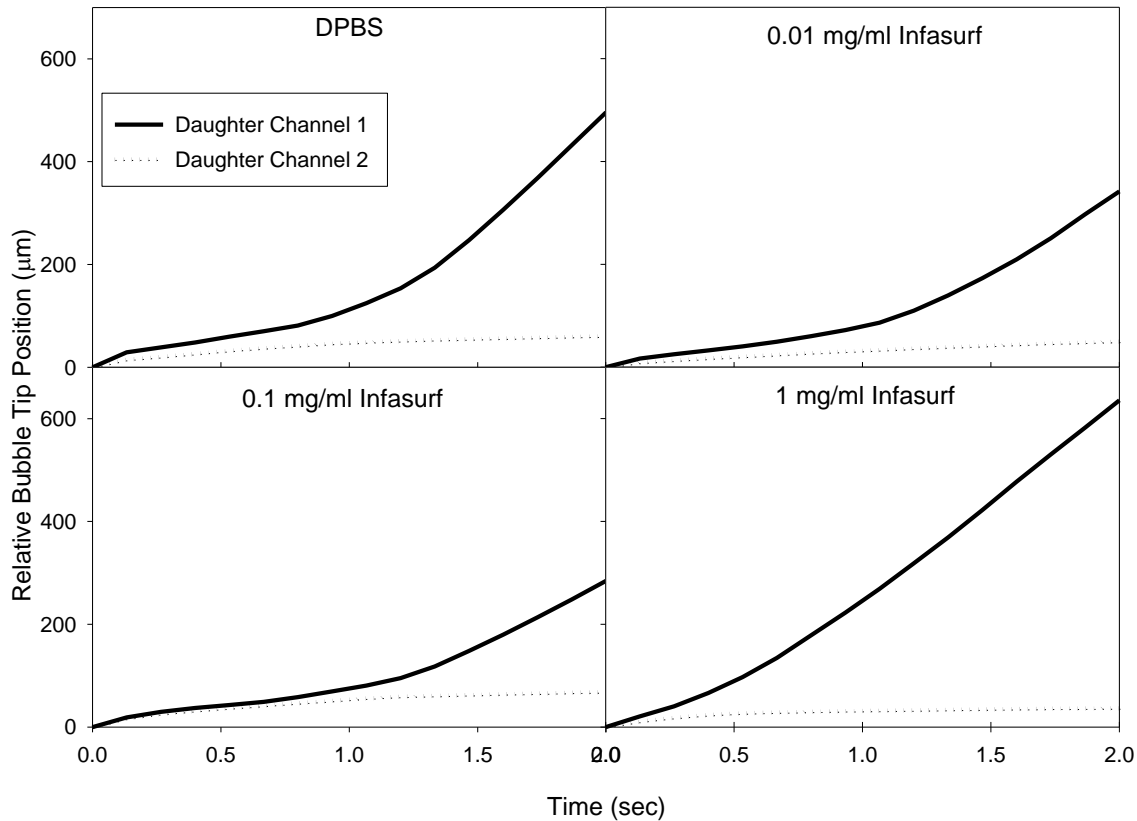**Figure 38 -**Average bubble propagation patterns for Daughter Channels 1 and 2 for Channel βA (different daughter channel widths 155μm, 145μm) with all solutions. In this model, the capillary and hydraulic pressures are different in each channel. <u>DPBS</u>: ~1.25 second pause in transition area, Channel 1 then quickly opens while the bubble in Channel 2 halts. <u>C=0.01mg/ml Infasurf</u>: ~0.5 second pause in the transition area, Channel 1 then quickly opens while the bubble in Channel 2 halts. <u>C=0.1mg/ml Infasurf</u>: ~1 second pause in transition area, Channel 1 then quickly opens while the bubble in Channel 2 halts. <u>C=1mg/ml Infasurf</u>: ~ 1 second pause in transition area, Channel 1 quickly opens while bubble in Channel 2 halts. <u>SDS</u>: ~1 second pause in transition area, Channel 1 quickly opens while bubble in Channel 2 halts.

Figure 39 - Average bubble propagation patterns for Daughter Channels 1 and 2 for Channel βB with all solutions (different daughter channel widths, 155μm, 145μm, moved carina tip to 5μm above center of parent channel) with all solutions. In this model the local capillary pressure at the carina tip is smaller in Channel 2, so it should open first. However, the carina tip radius of curvature is much larger than designed. Instead the two daughter channels open symmetrically until Channel 1 begins to propagate alone. <u>DPBS</u>: Channels open symmetrically for ~3 seconds. <u>C=0.1mg/ml Infasurf</u>: Channels open symmetrically for ~2.5 seconds. <u>C=1mg/ml Infasurf</u>: Channels open symmetrically for ~1.25 seconds. <u>SDS</u>: Channels open symmetrically for ~2.25 seconds.
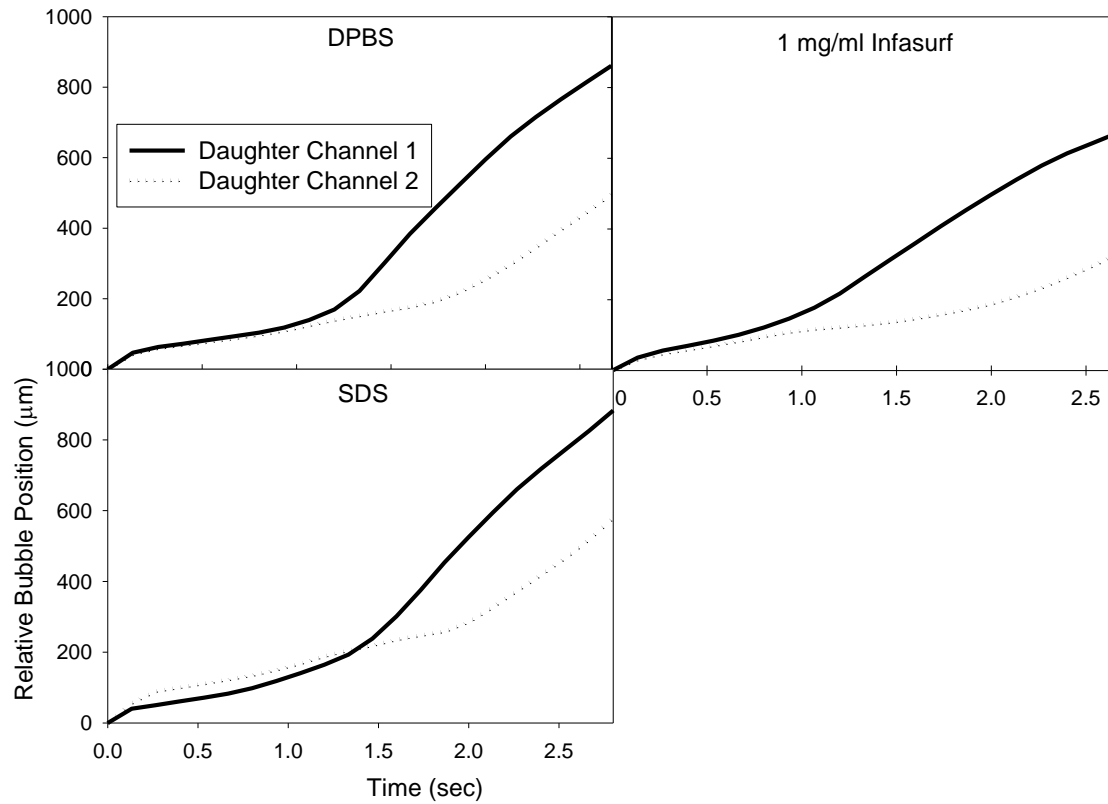
Figure 40 - Average bubble propagation patterns for Daughter Channels 1 and 2 for Channel βC (same width, different length, $L_2=1.1.069L_1$) with all solutions. In this model the hydraulic pressures are the same in both daughter channels, but differ in hydraulic pressures. Daughter Channel 1 always opens first because it has less resistance, but Daughter Channel 2 never halts because of the same capillary pressures. <u>DPBS</u>: Channels open symmetrically for ~2 seconds before Channel 1 takes lead. <u>C=0.01mg/ml Infasurf</u>: Channels open symmetrically for ~2 seconds before Channel 1 takes lead. <u>C=0. 1mg/ml Infasurf</u>: Channels open symmetrically for ~2.5 seconds before Channel 1 takes lead.
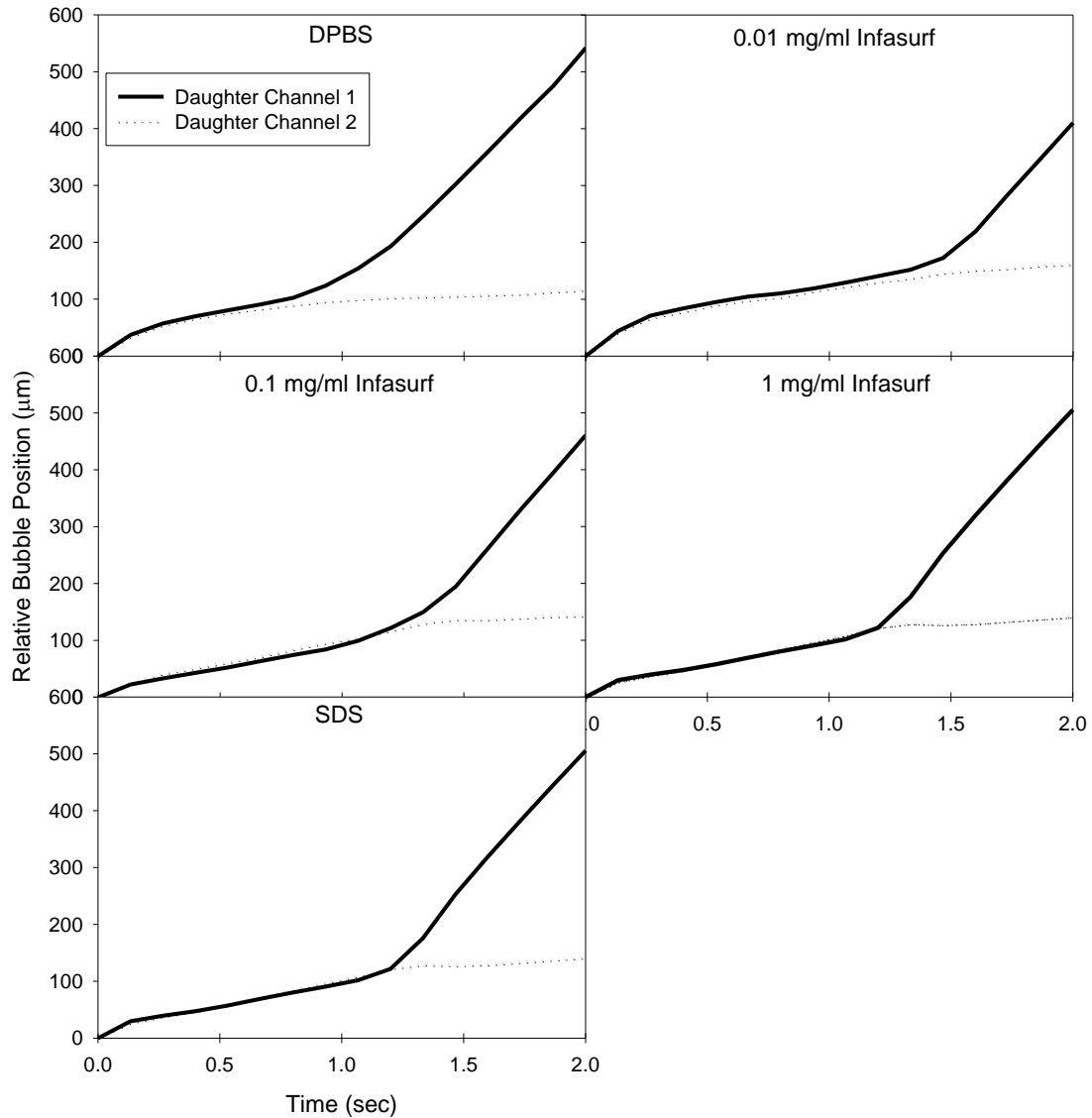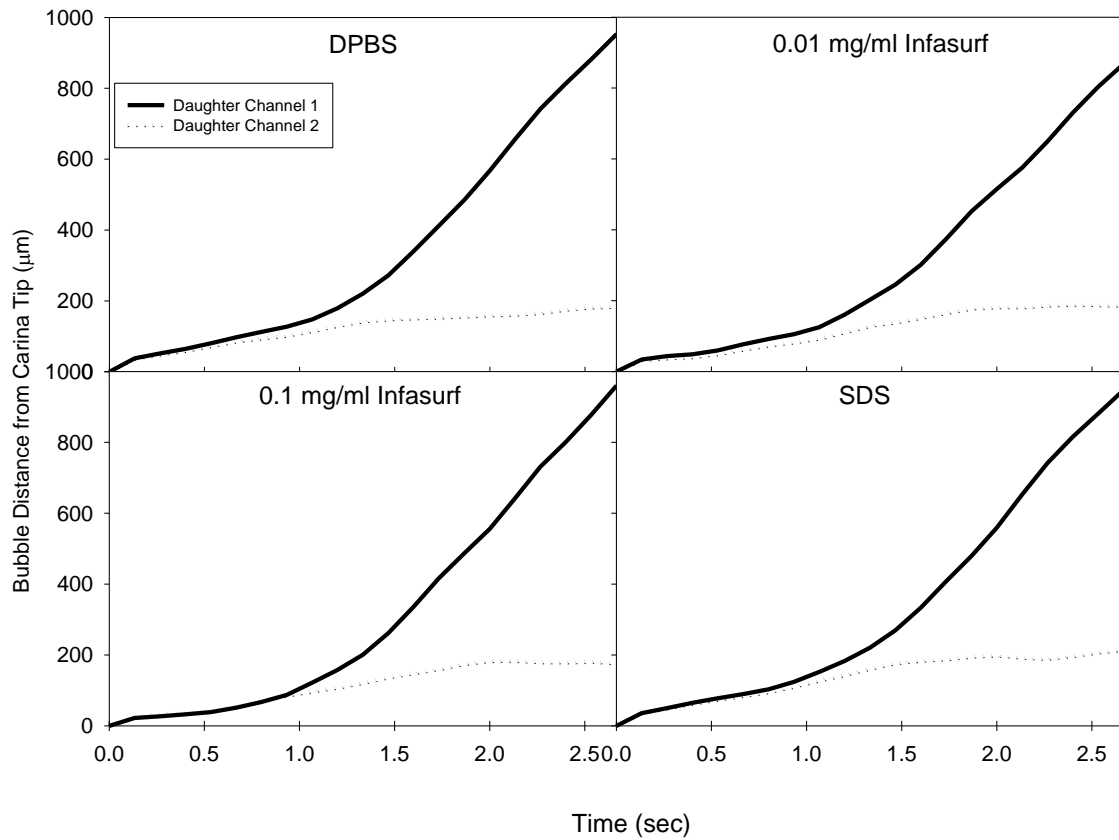
Figure 41 - Average bubble propagation patterns for Daughter Channels 1 and 2 for Channel γA with all solutions (different daughter channel widths 152μm, 148μm) with all solutions. In this model, the capillary and hydraulic pressures are different in each channel. <u>DPBS</u>: ~0.5 second pause in transition area, Channel 1 then quickly opens while bubble in Channel 2 halts. <u>C=0.01mg/ml Infasurf</u>: ~1.0 second pause pause in transition area, Channel 1 then quickly opens while bubble in Channel 2 halts. <u>C=0.1mg/ml Infasurf</u>: ~1.0 second pause in transition area, Channel 1 then quickly opens while bubble in Channel 2 halts. <u>SDS</u>: ~1 second pause in transition area, Channel 1 quickly opens while bubble in Channel 2 halts.
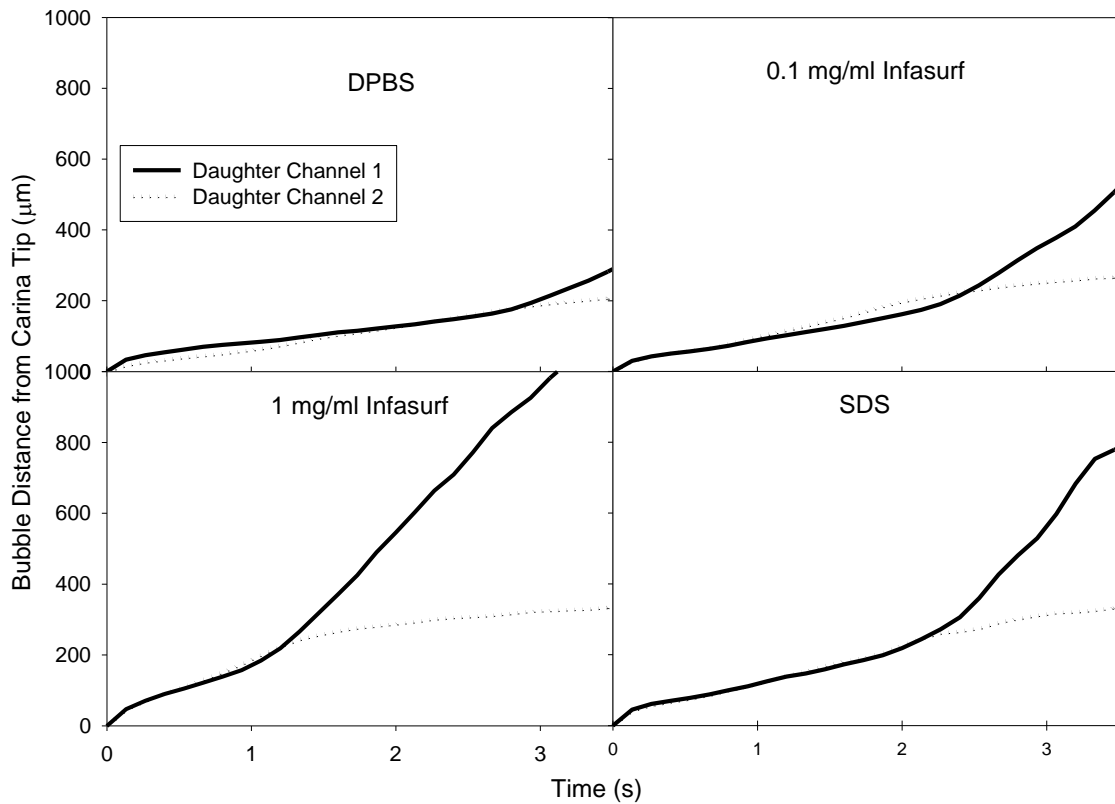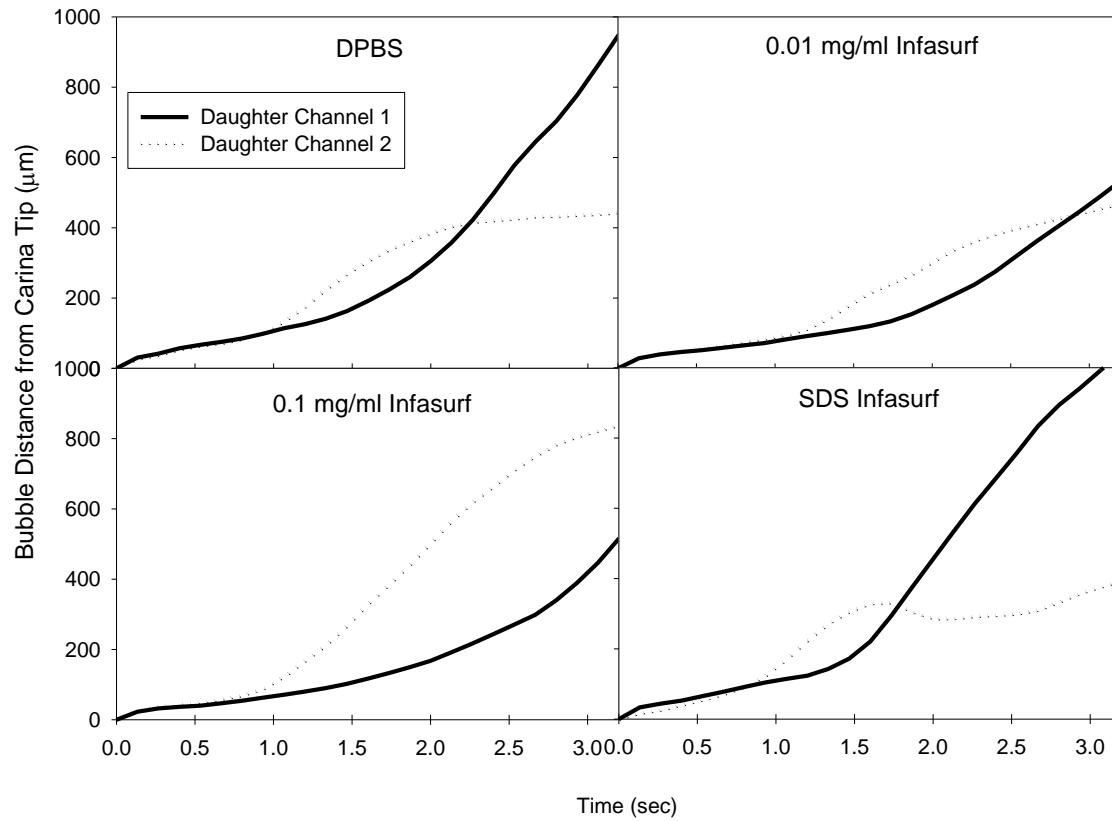
Figure 42 - Average bubble propagation patterns for Daughter Channels 1 and 2 for Channel γB with all solutions (different daughter channel widths, 152μm, 148μm, moved carina tip to 2μm above center of parent channel) with all solutions. In this model the local capillary pressure at the carina tip is smaller in Channel 2, causing it to open first. It will halt once it passes the transition area, and Channel 1 will then begin to fully open. <u>DPBS</u>: Channel 1 leads for ~2.25 seconds before Channel 1 quickly catches up. <u>C=0.01mg/ml Infasurf</u>: Channel 1 leads for ~2.75 seconds before Channel 1 quickly catches up. <u>C=0.1mg/ml Infasurf</u>: Channel 1 leads for ~4 seconds before Channel 1 catches up. <u>SDS</u>: Channel 1 leads for ~1.75 seconds before Channel 1 quickly catches up. With the introduction of surfactant in this model, Channel 2 completely reopens before Channel 1 catches up.
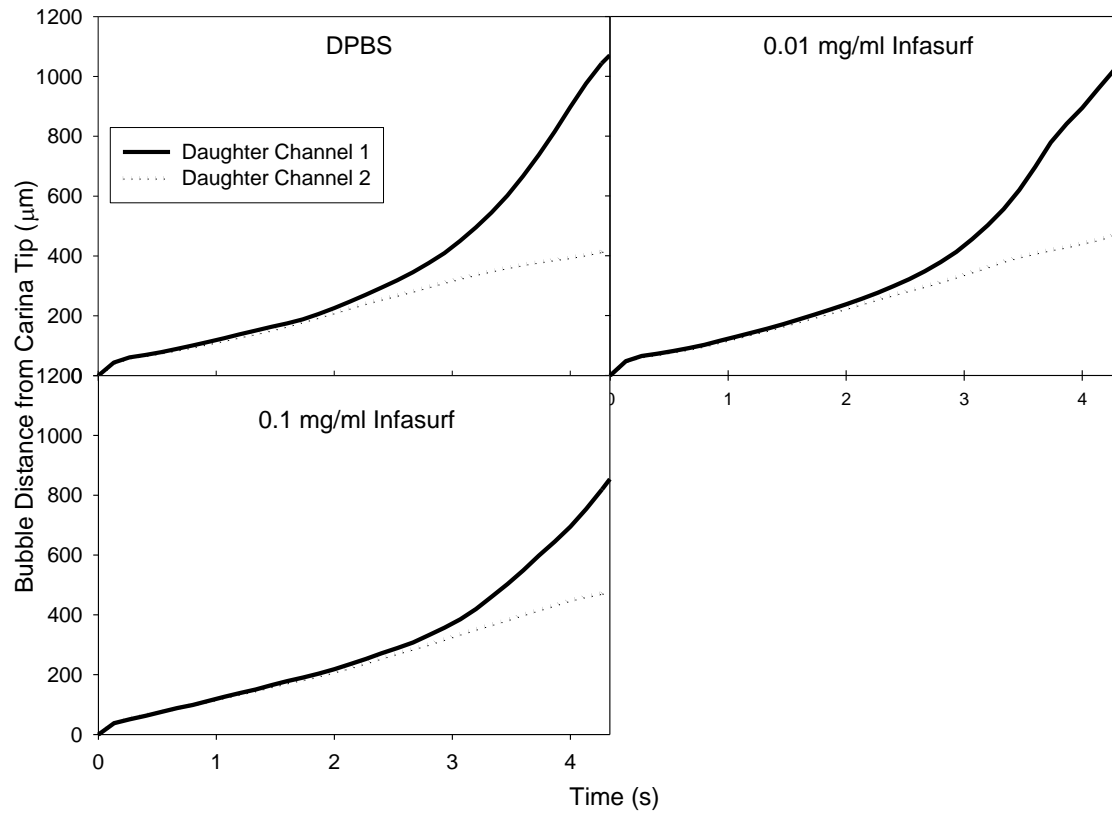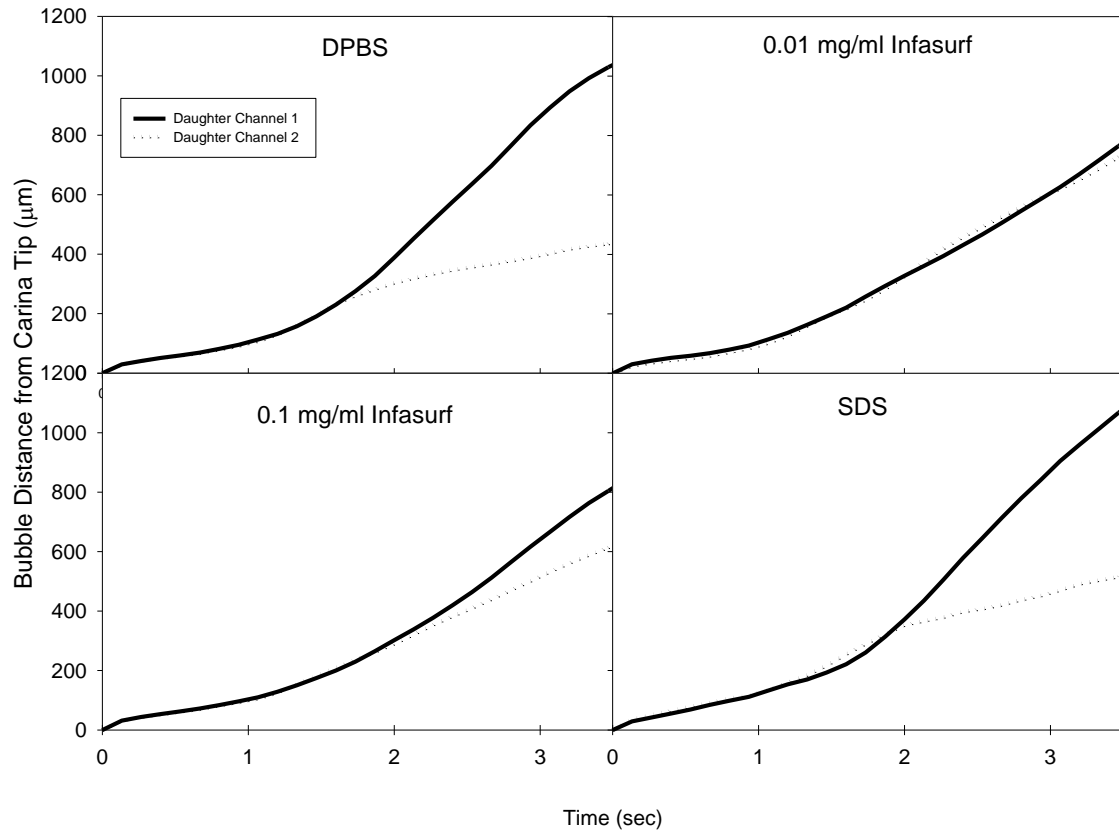
Figure 43 -- Average bubble propagation patterns for Daughter Channels 1 and 2 for Channel γC (same width, different length, $L_2=1.027L_1$) with all solutions. In this model the hydraulic pressures are the same in both daughter channels, but differ in hydraulic pressures. Daughter Channel 1 always opens first because it has less resistance, but Daughter Channel 2 never halts because of the same capillary pressures. <u>DPBS</u>: Channels open symmetrically for 1.75 seconds before Channel 1 takes lead. <u>C=0.01mg/ml Infasurf</u>: *Channels open symmetrically for entire bifurcation.* <u>C=0.01mg/ml Infasurf</u>: Channels open symmetrically for 2.25 seconds before Channel 1 takes lead. <u>SDS:</u> Channels open symmetrically for 2 seconds before Channel 1 takes lead

Chapter 5: Discussion

Now that the reopening profiles of each channel has been measured both with and without surfactant. We will then directly compare the effects of each solution on the reopening profile of each bifurcation. Ultimately we will determine which solutions are capable of best reopening which asymmetric bifurcations

5.1 Microfluidic Models

5.1.1 α Model

The comparison of the influence of different solutions in model αA where the cannel widths are varied is shown in Figure 44. In every experimental trial, Channel 1 opened first, and the bubble barely progressed at all in the narrow Channel 2 before coming to a complete stop. One main difference that can be seen between solutions, however, is how long the bubble propagates symmetrically in the transition period before the interface in Channel 2 comes to a complete stop.

Using (4), and replacing R with hydraulic diameter (D_h) the ratio of capillary pressures between channels can be estimated. For all of our models:

$$\frac{\Delta P_{cap1}}{\Delta P_{cap2}} \simeq \frac{\left(\gamma_1 / D_{h1}\right)}{\left(\gamma_2 / D_{h2}\right)} \tag{11}$$

Therefore the ratio of capillary pressure drops can be estimated as a ratio of D_h for when the surface tension is uniform along the surface of the bubble (DPBS or SDS solution).

When the surface tension is not uniform (Infasurf solutions), Daughter Channel 1 has a substantially lower surface tension due to the carina tip's distribution of the surfactant accumulation point at the center of the bubble tip to Channel 1. Therefore, the ratios are estimated to be .935 for uniform surface tension and .624 for non-uniform. These surface tensions are estimated using results from Langmuir Trough experiments. This shows that the introduction of the air-liquid interface to the daughter channel imposes varying additional resistance to Channel 2 depending on the solution. This explains why the slower Channel 2 always comes to a stop.

Since we designed our models to maintain $D_{h1} + D_{h2}=1.2D_{h0}$, the relationship between capillary pressure drops between channels:

$$\frac{\gamma}{D_{h1}}, \frac{\gamma}{D_{h2}} > \frac{\gamma}{D_{h0}} \tag{12}$$

Requires additional pressure to split the bubble tip. Since PDMS is elastic, it can absorb additional pressure, causing slow reopening at the beginning of the bifurcation. Therefore the duration of the transition period is related to the dynamic surface tension.

Model αA

Figure 44 - Relative Position Difference in Model αA (different daughter channel widths 160µm, 140µm) for all solutions. This figure shows the bubble position in each daughter channel relative to the other vs. time. Negative Values indicate that the interface in Channel 2 is further downstream, while positive values indicate that the interface in Channel 1 is further downstream.

Model αB
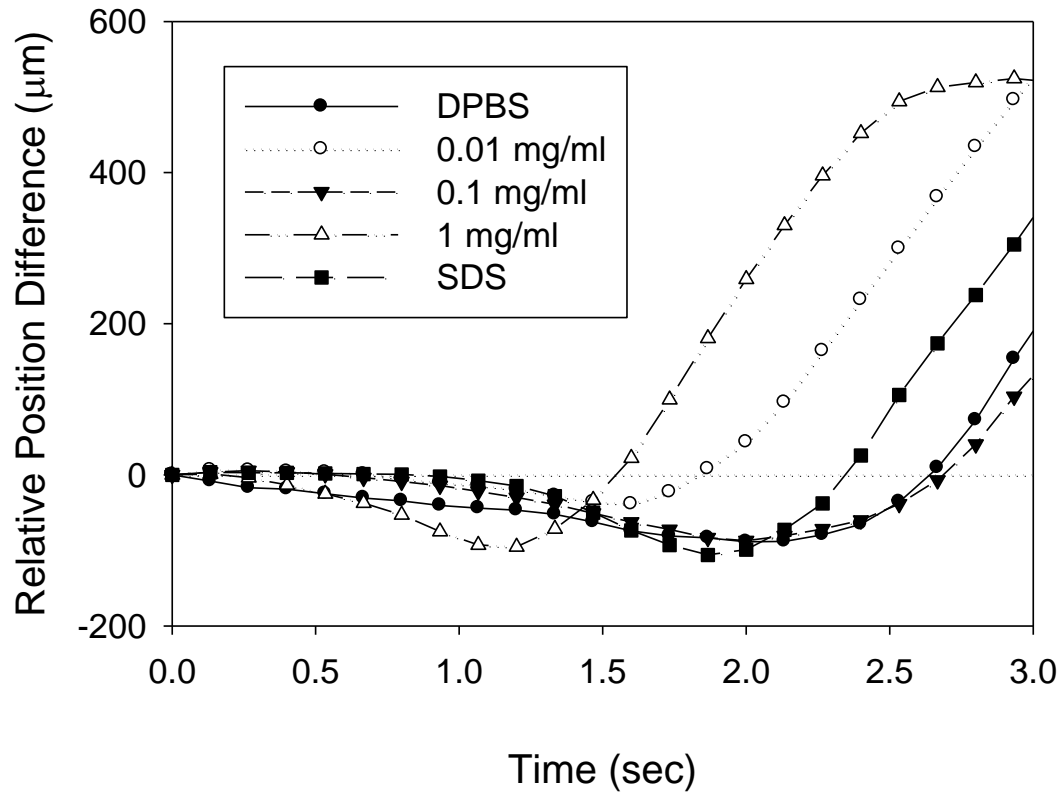
Figure 45 - Relative Position Difference in Model αB (different daughter channel widths, 160µm, 140µm, moved carina tip to 10µm above center of parent channel) for all solutions.

Model αD
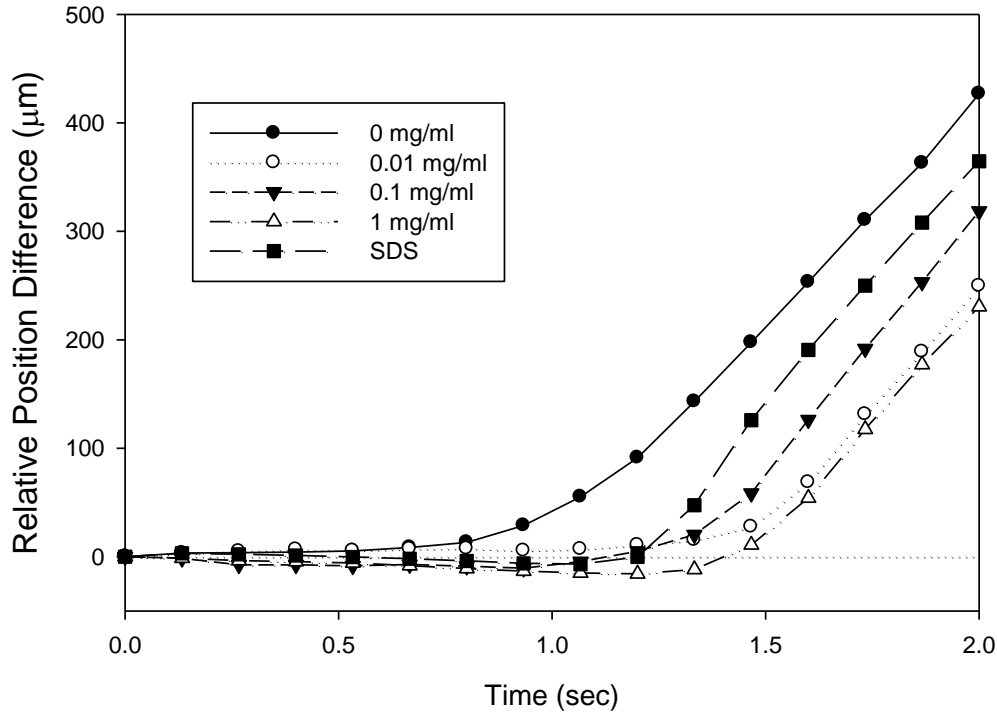
Figure 46 - Relative Position Difference in Model αD (different daughter channel widths, 160μm, 140μm, moved carina tip to center of parent channel) for all solutions

The same experiment but with αB and αD (same model geometry as αA, but with carina tip moved to +10μm and 0) is shown in Figure 48 and Figure 46. As previously mentioned, transition period is related to dynamic surface tension, and the interface in Channel 2 always came to a complete stop due to the imposed capillary pressure further downstream. The moved tip causes $D_{h1}<D_{h2}$ in the transition zone, and thus the surfactant concentration point at the bubble tip is distributed to Channel 2. Therefore the expected capillary drop of Channel 2 at the beginning of the bifurcation is much lower

91

than that of Channel 1. This explains why Channel 2 opens in the transition period

before it reaches the same geometry as in αA further downstream.

Model αC
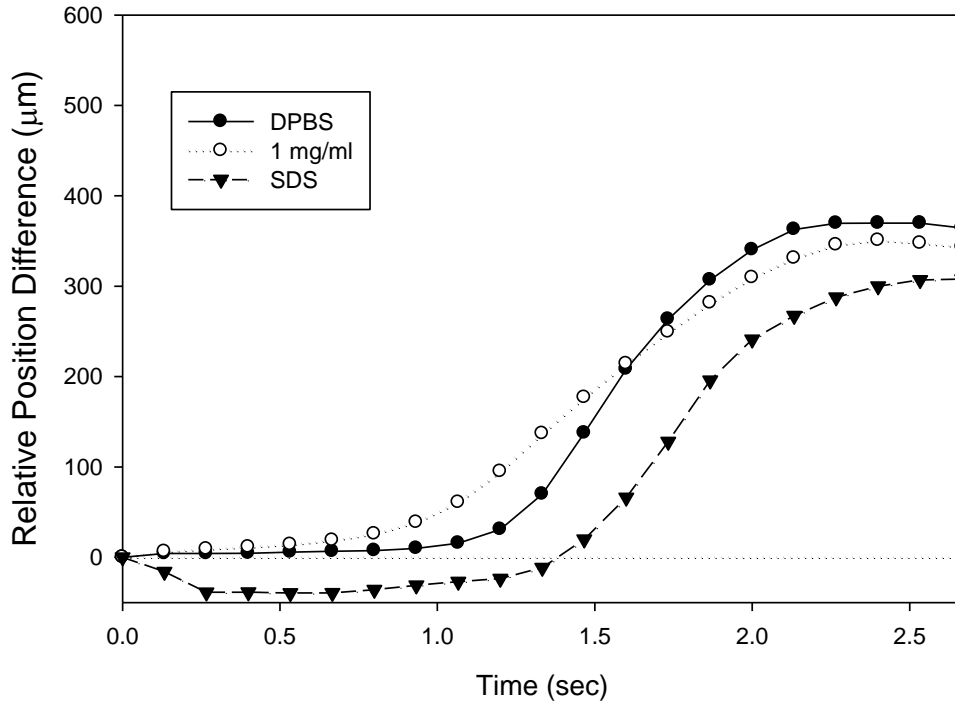
Figure 47 - Relative Position Difference in Model αC (same width, different length, $L_2=1.1.143L_1$) for all solutions.

The same experiment but with αC (Daughter Channel geometry is the same, but

different length) is shown in Figure 47. In this case, $D_{h1}=D_{h2}$ and the difference will be

imposed by the length of the liquid remaining in daughter section. Since there is no

capillary pressure drop difference between daughter channels at the beginning of the

bifurcation, Channel 2 did not stop during in the transition period (t=0-1.5) and continues

to propagate throughout the experiment. With Infasurf 1.0 solution, the transition period is shorter, and the development of relative difference is slower than those of DPBS and SDS. This phenomenon can be explained by the unique dynamic surface properties of Infasurf rich solution (Yamaguchi et al. 2014).

5.1.2 β Model

Figure 48-Figure 50 are the results from the β models which resemble the α models, but with smaller differences in channel width and length. In basic, these models follow the same patterns as those discussed for the α models with only small degrees of differences with one exception. The transition period in the model βB (Figure 49) does not show as significant an impact on reopening of Channel 2 as seen in model αB (Figure 45) due to the previously mentioned geometric inaccuracy of the carina tip in this model.

Model βA
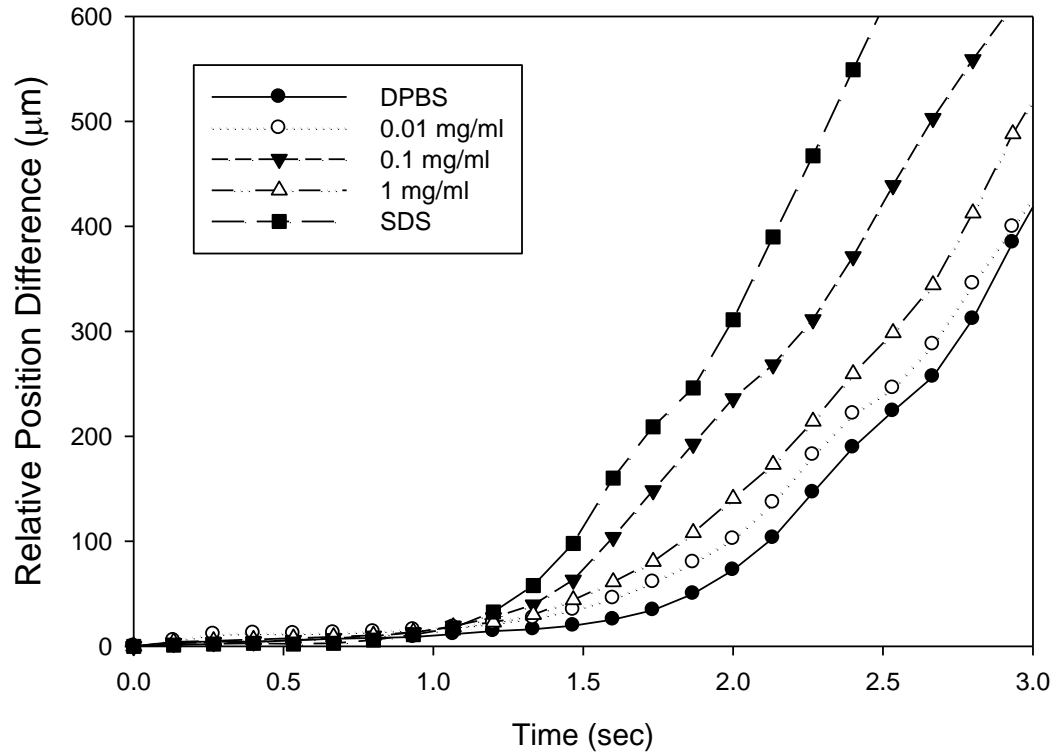
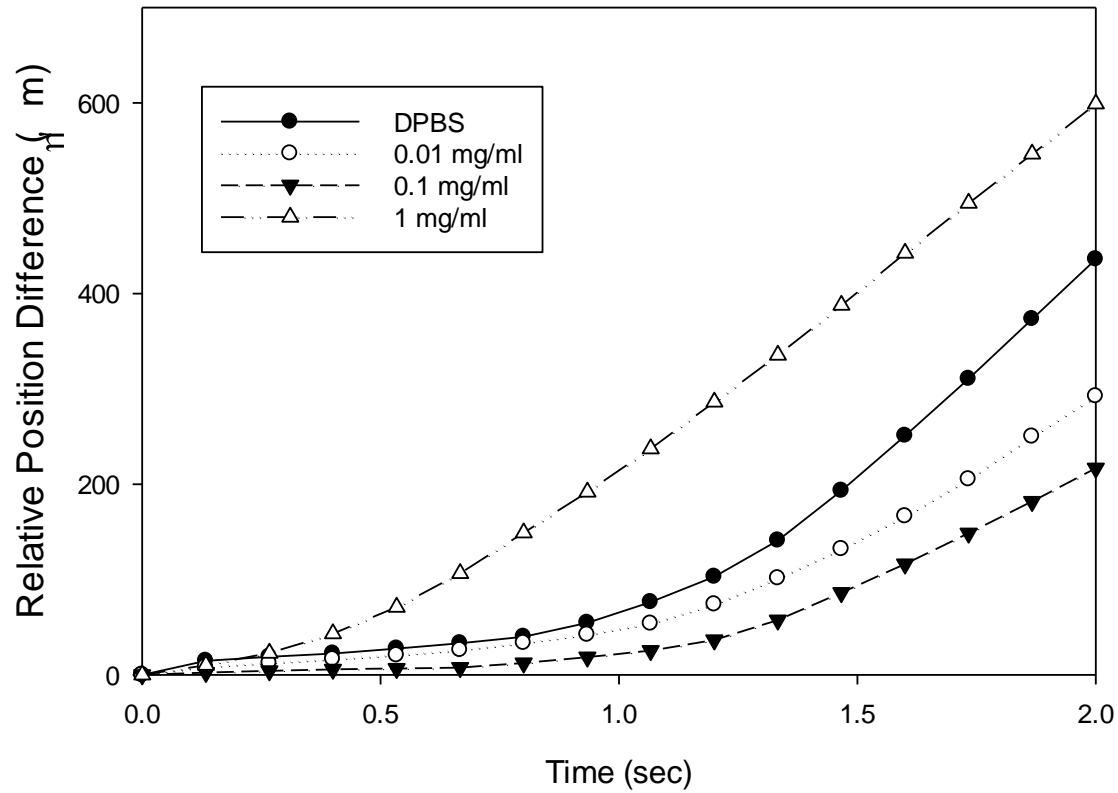**Figure 48 - Relative Position Difference in Model βA (different daughter channel widths 155µm, 145µm) for all solutions. DPBS has the longest time of symmetric reopening while SDS had the shortest. Channel 1 opens in every run with every solution. Channel 1 opens in every run with every solution, while the interface in Channel 2 comes to a complete stop.**

Model βB
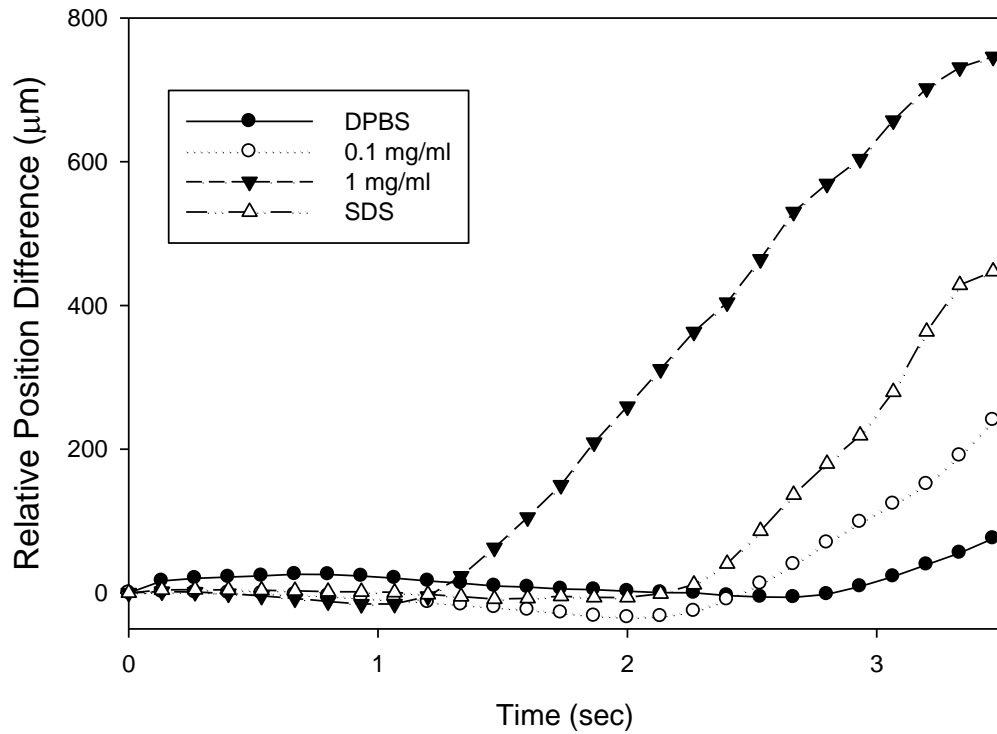
Figure 49 - Relative Position Difference in Model βB different daughter channel widths, 155μm, 145μm, moved carina tip to 5μm above center of parent channel) for all solutions. DPBS has the longest period of symmetric reopening while C=1.0 mg/ml Infasurf has the shortest. The large radius of curvature at the carina tip clearly changes the reopening profile of each solution. Channel 1 opens in every run with every solution, while the interface in Channel 2 comes to a complete stop.

Model βC
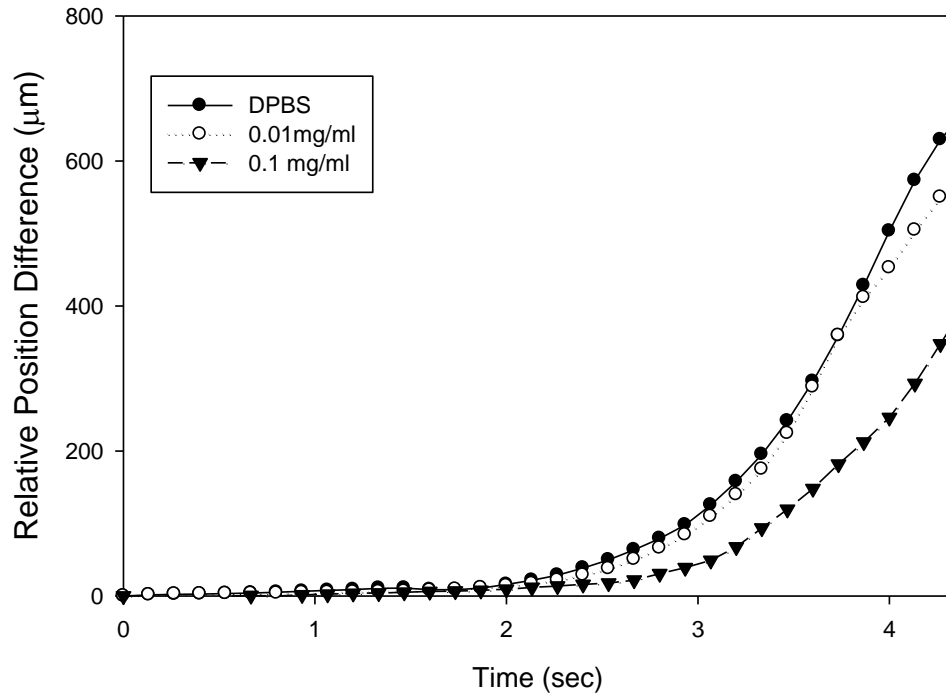
Figure 50 - Relative Position Difference in Model βC (same width, different length, $L_2=1.069L_1$) for all solutions. DPBS and C=0.01 mg/ml have almost identical reopening profiles. C=0.1 mg/ml Infasurf has a longer period of symmetric reopening. Channel 1 reopens in every run with every solution, but the interface in Channel 2 never stops propagating.

5.1.3 γ Model

γ models strongly resemble the α model, but with even smaller differences in the channel width or length. Figure 51 shows significant differences between surfactant solutions. The advantageous capillary pressure drop difference on Channel 2 imposed by the moved carina tip is now capable of sustaining reopening throughout Channel 2. For example the C=0.1 mg/ml Infasurf solution starts with a 400μm lead in Channel 2, and

takes until the end of the bifurcation for Channel 1 to catch up. This event also occurs for the other solutions, but in much smaller degree, but now we can finally see this trend outside of transition period.

Model γB
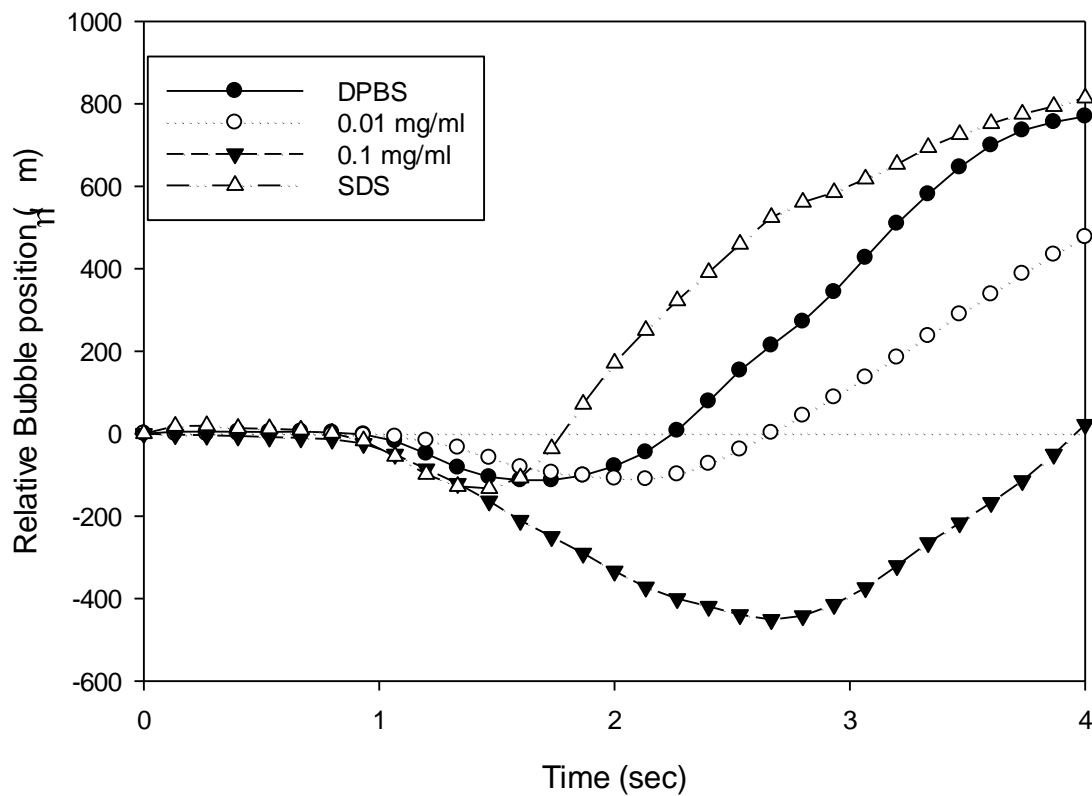
Figure 51 - Relative Bubble Position Difference for Model γB (different daughter channel widths, 152μm, 148μm, moved carina tip to 2μm above center of parent channel) for all solutions.

Since the balance of Channel 1 and 2 is so sensitive in these γ models, data starts to exhibit large fluctuations during separate runs. For example, there were 2 runs of the

0.01 mg/ml solution that actually completely open Channel 2. Including these significantly alters the average relative position difference; therefore most of the runs for the 0.01 mg/ml solution are not well reflected in Figure 51. The error bars that are created by this can be seen in Figure 52. This figure helps to prove how fragile the balance of the reopening profile now becomes with the introduction of surfactant.

98

Average Channel Velocities 0.01 mg/ml Infasurf, γB model
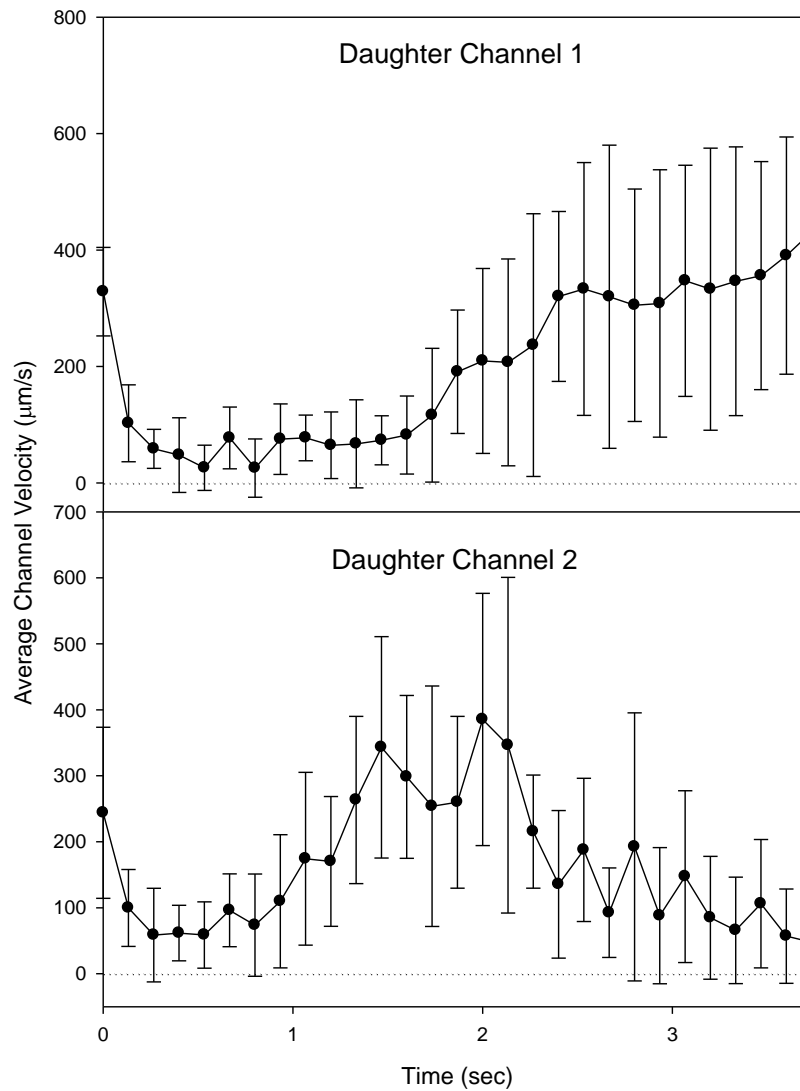
Figure 52 - Average velocities of 0.01 mg/ml Infasurf Solution with standard deviation in γB model

The hydraulic pressure difference in the γC model is now so small that, with the introduction of surfactant, the two daughter channels can now open symmetrically, as seen in Figure 53. Since the hydraulic diameters are the same in this model, there is no

99

capillary pressure difference between each daughter channels. Using Equation (4), the symmetric reopening of the two daughter channels is likely to occur only with dynamic surface tension (Yamaguchi et al. 2014).

Model γC
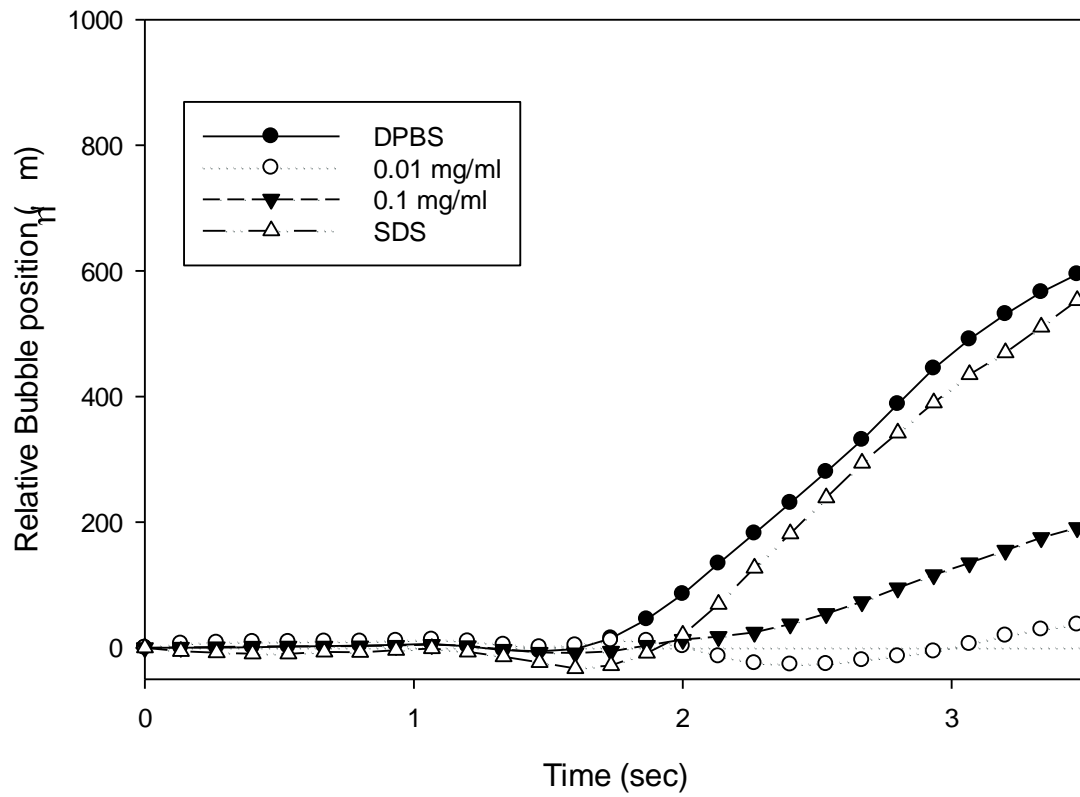
Figure 53 - Relative Bubble Position Difference for Model γC (same width, different length, $L_2=1.027L_1$).

5.1.4 Stability Analysis

Now that we have determined how the varying solutions affect the reopening profile of the different asymmetric bifurcating networks. It is important to measure how stable these results are. In order to do this, the amount of variation that took place at the end of the transition period (t=2.5 sec) for models γB&C were examined.

Relative Position Difference at t=2.5 for γ Models
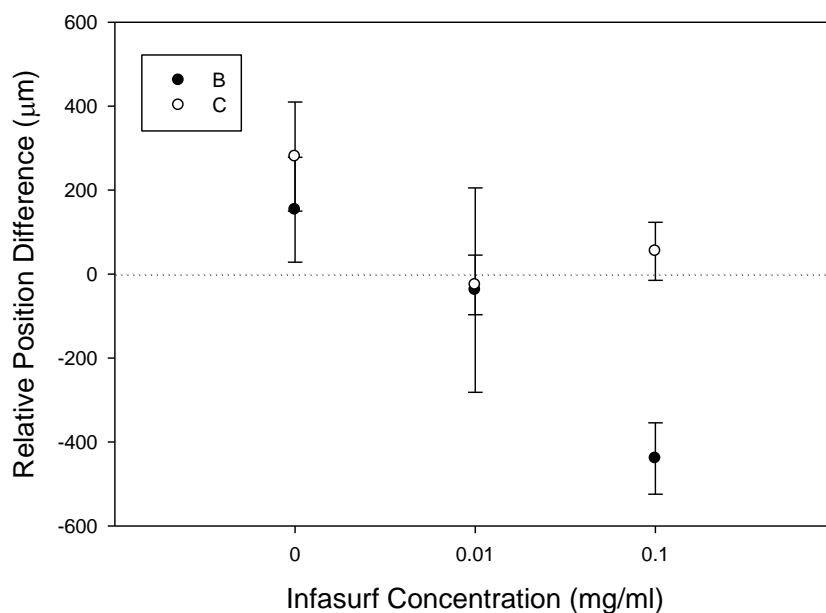
Figure 54 - Relative position differences for γ models at different times for varying solutions

With the exception of the 0.01 mg/ml solution in model γB experiment, the standard deviation of the relative bubble position actually became more stable as the concentration of surfactant increased. The fact that, with the exception of one experimental trial, a simple change of solution had such a large and consistent effect on

the reopening profile of each model proves how delicate the reopening profile of this channel is. It also indicates that pulmonary surfactant possesses a dynamic surface tension that helps to induce a symmetric reopening profile.

5.2 Limitations

While this study was a carefully controlled study, it, like all experiments, has limitations based upon design and fabrication constraints. These are some of the limitations we have identified:

1. The rigidity of the walls of the microchannels presents two problems. First, pulmonary airways are much more compliant than the walls in our model. Second, the elasticity of the walls allows for an unknown amount of wall buckling during interface propagation.

2. The microfabrication technique used allow for the creation of rectangular cross-sections. Also the channel depth is constant throughout the device. This is morphologically incorrect because all human airways are either circular or elliptical, there are no corners.

3. Angular variations are limited in this study due to the size of the observation window in our PIV system. In the human lung, the branching angle tends to change depending on the relative daughter channel size. For example the smaller of the two daughter channels with have a higher branching angle than the larger channel. This system is also limited in that all branching must be done on a flat

surface, so the space-filling three-dimensional branching found in the lungs cannot be explored.

4. Although surface modification efforts were made with Silane, the device does not precisely represent the wetting profile of the pulmonary airways.

5. Our experimental flow control utilized a constant flow-rate syringe pump that created a low differential pressure within the system that would pull the air interface into the "airway." Although this is how inspiration works, it does not model how ventilators push air into the closed airways. An alteration of our system to allow for volume or upstream volume or pressure driving flow control could present alternative findings.

Chapter 6: Conclusions

We have successfully designed and created a physiologically relevant asymmetric bifurcating network using soft lithography and PDMS replica molding. We were also successful in creating a standardized geometry, and then systematically changing three parameters in the transition zone (daughter channel width, carina tip location, and daughter channel length). Next, with a modified PIV system we examined the instantaneous bubble position throughout the bifurcation process.

This study successfully demonstrated how different asymmetries will affect the reopening profile with different solutions.

1. Infasurf can symmetrically reopen asymmetric bifurcations with daughter channels that have different lengths, observed with γC.

2. If $L_2 > 1.027 L_1$, Infasurf does not unify reopening process.

3. Infasurf was unable to symmetrically reopen both channels of the A models that have different channel widths.

4. Moving the carina tip location, however, can distribute enough surfactant to the more resistant channel and ultimately reopen both daughter channels.

The location of the carina tip proved to have significant effect on the reopening profile of all models. When the carina tip was below the centerline (A models), Channel 1 always opened first. However, once the carina tip was moved above the centerline of the parent channel (B models), Channel 2 opened first despite the fact that Channel 1 was less resistant to flow. Moving the carina tip allowed us to choose which daughter channel

would receive the accumulation of surfactant at the bubble tip. This, in turn, significantly lowered the surface tension in that channel and allowed it to open first. In model γB, this allowed Channel 2 to completely open before Channel 1. Finally, altering the length of the daughter channels (C models) did not cause the bubble tip to come to a halt in the more resistant Channel 2 as it did in the A and B models. In model γC the introduction of surfactant allowed both daughter channels to open at the same rate. We hypothesize that unlike SDS and DPBS, Infasurf has the ability to locally concentrate on the air-liquid interface and dynamically add additional resistance to the capillary pressure. These result can be seen again in Figure 55 and Figure 56.

Model γB
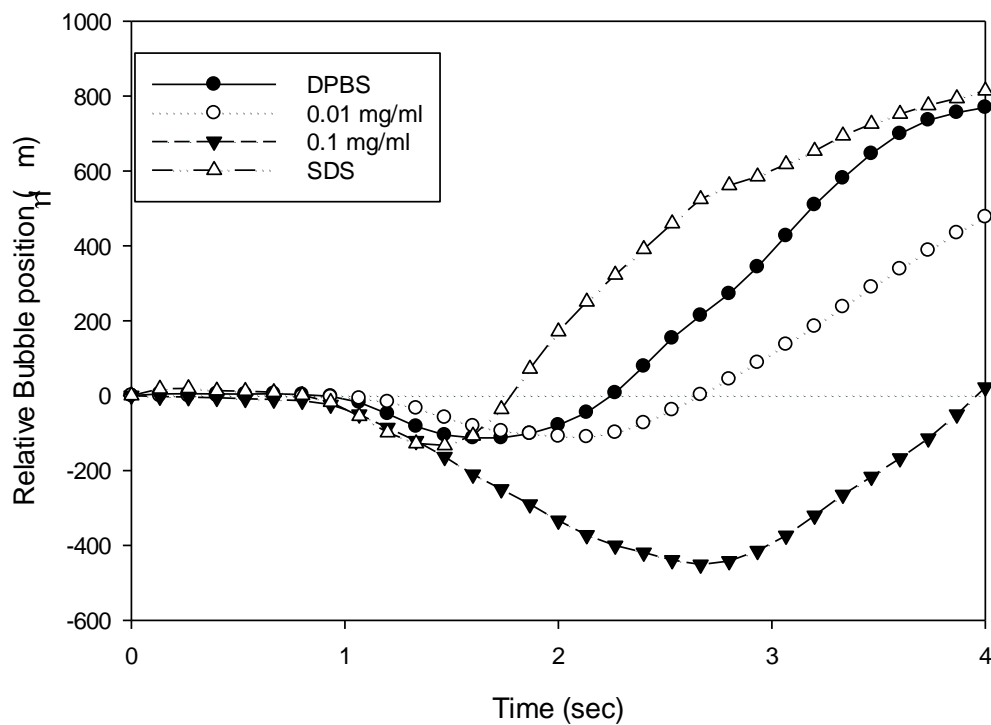
Figure 55 - Relative Bubble Position Difference for Model γB (different daughter channel widths, 152μm, 148μm, moved carina tip to 2μm above center of parent channel) for all solutions.

Model γC
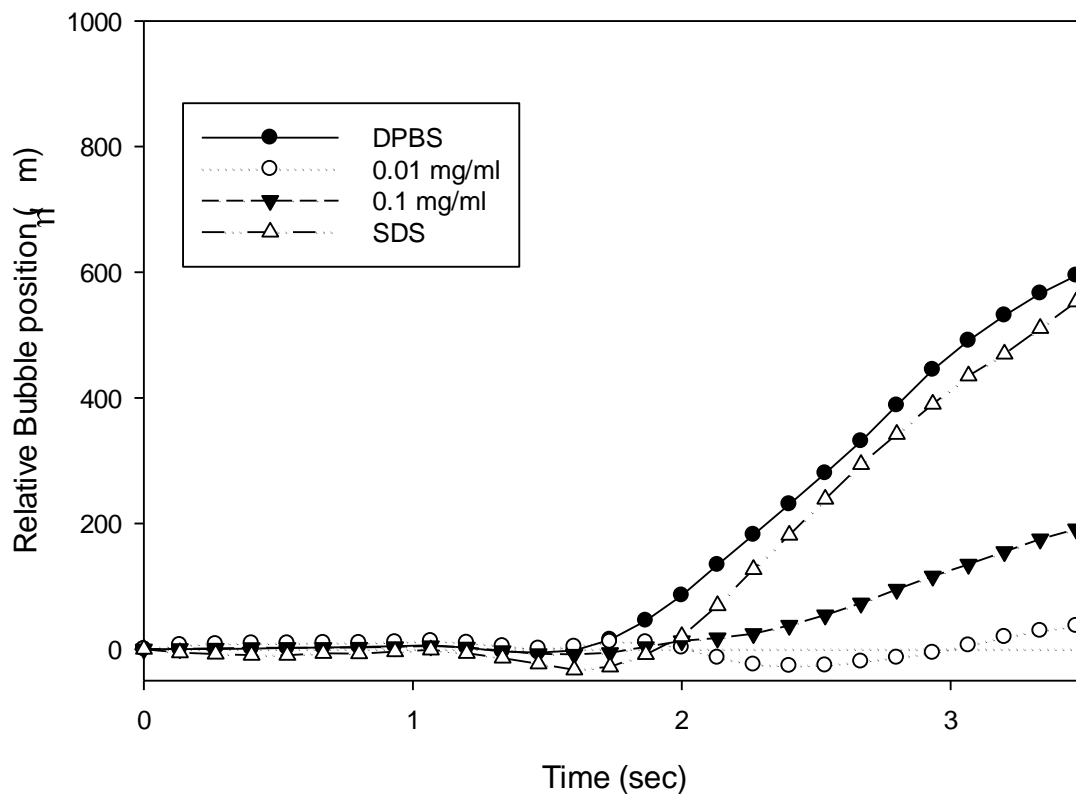
Figure 56 - Relative Bubble Position Difference for Model γC (same width, different length, $L_2=1.027L_1$).

The exact relationship between surface flow and molecular mobility has yet to be examined; however, it can be, using the apparatus, methodology, and analysis presented in this study by changing the flow parameters.

Future Work

In our study, we found evidence that surfactant accumulates on the surface differently depending on the speed of the bubble propagation. The next logical step,

therefore, is to examine how pulsatile flows will affect the reopening profile of these asymmetric models.

Another suggestion is that PDMS molding is limited by two dimensions. Since we are only capable of creating square channels with our current method, our model is not completely physiologically relevant. Finding another manufacturing method can potentially allow us to create a circular, 3-dimensional model would allow us to eliminate one of the major limitations of our study.

Finally, in vitro experiments with the methods and devices presented in our work but with seeded cells at the channel wall could allow us to determine the effect of the reopening of a bifurcation on these cells. A previous study done in our lab (Glindmeyer & Smith 2012) demonstrated the ability of pulsatile flows to reopen straight tubes lined with cells without damaging the cells. However, how these types of flows will affect cells at the carina tip, as well as at the channel wall of a bifurcating model is another possible direction for this study.

Bibliography

1. Abate, Adam, et al. "Glass Coating for PDMS Microfluidic Channels by Sol-Gel Methods." *Lab on a Chip* 8 (2008): 516-8. Print.

2. Adrian, R. J. "Twenty Years of Particle Image Velocimetry." *Experiments in Fluids* 39.2 (2005): 159,169-169. Print.

3. Bhattacharya, Shantanu, et al. "Studies on Surface Wettability of Poly(Dimethyl) Siloxane (PDMS) and Glass Under Oxygen-Plasma Treatment and Correlation with Bond Strength." *Journal of Micromechanical Systems* 14.3 (2005): 590. Print.

4. Binous, Housam. *Poisseuille Flow in a Rectangular Channel*. Mathworks.com:, 2007. Print.

5. Christensen, Andrew M., David Chang-Yeun, and Bruce Gale. "Characterization of Interconnects used in PDMS Microfluidic Systems." *Journal of Micromechanics and Microengineering* 15.5 (2005): 928. Print.

6. Coyne, K., et al. "Inspiratory Flow Rates during Hard Work when Breathing through Different Respirator Inhalation and Exhalation Resistances." *journal of occupational and environmental hygiene* 3.9 (2006): 490-500. Print.

7. Dearden, Marissa. "The Incoporation of Fluorescently Tagged Phosphatidylcholine into Ifasurf Solution." Undergraduate Tulane University, 2014. Print.

8. Derdak, Stephen, et al. "High-Frequency Oscillatory Ventilation for Acute Respiratory Distress Syndrome in Adults." *American Journal of Respiratory and Critical Care Medicine* 166.6 (2002): 801. Print.

9. Frijlink, H. W., and A. H. De Boer. "Dry Powder Inhalers for Pulmonary Drug Delivery." *Expert Opinion on Drug Delivery* 1.1 (2004): 67. Print.

10. Garbassi, F., et al. *Polymer Surfaces. from Physics to Technology.* New York: Wiley, 1994. Print.

11. Gaver III, Donald P., et al. "The Significance of Air-Liquid Interfacial Stresses on Low-Volume Ventilator-Induced Lung Injury." *Ventilator-Induced Lung Injury Lung Biology in Health and Disease.* Ed. D. Dreyfuss.Taylor & Francis, 2006. 157-203; 7. Print.

12. Gaver, D. P., R. W. Samsel, and J. Solway. "Effects of Surface Tension and Viscosity on Airway Reopening." *Journal of Applied Physiology* 69.1 (1990): 74-85. Print.

13. Gaver, Donald P., et al. "The Steady Motion of a Semi-Infinite Bubble through a Flexible-Walled Channel." *Journal of Fluid Mechanics* 319 (1996): 25-65. Print.

14. Giannetti, Matthew J. "A Microfluidic Model of Pulmonary Airway Reopning in Bifurcating Networks." Master Tulane University, 2013. Print.

15. Glindmeyer, H. W., and Bradford J. Smith. "In Situ Enhancement of Pulmonary Surfactant Function using Temporary Flow Reversal." *Journal of Applied Physiology* 112.1 (2012): 149-58. Print.

16. Hammersley, J. R., and D. E. Olson. "Physical Models of the Smaller Pulmonary Airways." *Journal of Applied Physiology* 72.6 (1992): 2402-14. Print.

17. Horsfield, K., and G. Cumming. "Angles of Branching and Diameters of Branches in the Human Bronchial Tree." *Bulletin of Mathematical Biology* 29.2 (1967): 245,259-259. Print.

18. Horsfield, K., et al. "Models of the Human Bronchial Tree." *Journal of Applied Physiology* 31.2 (1971): 207-17. Print.

19. Kandlikar, S., et al. *Heat Transfer and Fluid Flow in Minichannels and Microchannels*. 1st ed. Great Britain: Elsevier Ltd., 2006. Print.

20. Kandlikar, S., and W. Grande. "Evolution of Microchannel Flow Passages-- Thermohydraulic Performance and Fabrication Technology." *Heat Transfer Engineering* 24.1 (2003): 3-17. Print.

21. Kim, B., E. T. K. Peterson, and I. Papautsky. "Long-Term Stability of Plasma Oxidized PDMS Surfaces". *Engineering in Medicine and Biology Society, 2004. IEMBS '04. 26th Annual International Conference of the IEEE.* 1-5 Sept. 2004, 2004. 5013-5016. Print.

22. Kleinstreuer, Clement, Zhe Zhang, and Zheng Li. "Modeling Airflow and Particle transport/deposition in Pulmonary Airways." *Respiratory Physiology & Neurobiology* 163.1-3 (2008): 128-38. Print.

23. Krueger, Melissa A., and Donald P. Gaver III. "A Theoretical Model of Pulmonary Surfactant Multilayer Collapse Under Oscillating Area Conditions." *Journal of colloid and interface science* 229.2 (2000): 353-64. Print.

24. Lee, Dongyoub, et al. "Bifurcation Model for Characterization of Pulmonary Architecture." *The Anatomical Record: Advances in Integrative Anatomy and Evolutionary Biology* 291.4 (2008): 379-89. Print.

25. Liu, R. H., et al. "Passive Mixing in a Three-Dimensional Serpentine Microchannel." *Microelectromechanical Systems, Journal of* 9.2 (2000): 190-7. Print.

26. McDonald, J. Cooper, et al. "Fabrication of Microfluidic Systems in Poly(Dimethylsiloxane)." *Electrophoresis* 21.1 (2000): 27-40. Print.

27. Meinhart, C. D., S. T. Wereley, and J. G. Santiago. "PIV Measurements of a Microchannel." *Experiments in Fluids* 27.5 (1999): 414-419. Print.

28. Meyerhofer, Dietrich. "Characteristics of Resist Films Produced by Spinning." *Journal of Applied Physics* 49.7 (1978): 3993-7. Print.

29. Microchem. "SU-8 Permanent Epoxy Negative Photoresist." 2015.Web. <http://microchem.com/pdf/SU-8%203000%20Data%20Sheet.pdf>.

30. Ng, Jessamine M. K., et al. "Components for Integrated Poly(Dimethylsiloxane) Microfluidic Systems." *Electrophoresis* 23.20 (2002): 3461-73. Print.

31. Ntoumenopoulos, G., H. Shannon, and E. Main. "Do Commonly used Ventilator Settings for Mechanically Ventilated Adults have the Potential to Embed Secretions Or Promote Clearance?" *Respiratory Care* 56.12 (2011): 1887-92. Print.

32. Smith, B. J. "A Translating Stage System for Œº-PIV Measurements Surrounding the Tip of a Migrating Semi-Infinite Bubble." *Measurement Science and Technology* 21.1 (2009): 015401. Print.

33. Sui, Guodong, et al. "Solution-Phase Surface Modification in Intact Poly(Dimethylsiloxane) Microfluidic Channels." *Analytical Chemistry* 78.15 (2006): 9-5543. Print.

34. Voldman, Joel, Martha Gray, and Martin Schmidt. "Microfabrication in Biology and Medicine." *Annual review of biomedical engineering* 1 (1999): 401. Print.

35. Ware, Lorraine B., and Michael A. Matthay. "The Acute Respiratory Distress Syndrome." *New England Journal of Medicine* 342.18 (2000): 1334-49. Print.

36. Weibel, E. R. *Morphometry of the Human Lung*. Academic Press, 1963. Print.

37. Willson, Herbert G. "The Terminals of the Human Bronchiole." *American Journal of Anatomy* 30.3 (1922): 267-95. Print.

38. Xia, Younan, and George M. Whitesides. "Soft Lithography." *Annual Review of Materials Science* 28 (1998a): 153. Print.

39.Xia, Younan, and George M. Whitesides. "Soft Lithography." *Angewandte Chemie International Edition* 37.5 (1998b): 550-75. Print.

40.Yamaguchi, Eiichiro, Brad Smith, and Donald Gaver. "M-PIV for the Analysis of Flow Fileds Near a Propagating Air-Liquid Interface." *The Particle Image Velocitometry: Characteristics, Limits and Possible Applications.*, 2012. 261-282. Print.

41.Yamaguchi, Eiichiro, et al. "The Unusual Symmetric Reopening Effect Induced by Pulmonary Surfactant." *Journal of applied physiology* 116.6 (2014): 635-44. Web.

42.Yamaguchi, Eiichiro, Bradford J. Smith, and Donald P. Gaver III. *U-PIV for the Analysis of Flow Fields Near a Propagating Air-Liquid Interface*. Ed. Giovanna Cavazzini. InTech, 2012. Print.

43.Zasadzinski, Joseph A., et al. "Overcoming Rapid Inactivation of Lung Surfactant: Analogies between Competitive Adsorption and Colloid Stability." *Biochimica et Biophysica Acta (BBA) - Biomembranes* 1798.4 (2010): 801-28. Print.

Biography

Liam Nolan was born and raised in New Orleans, LA. Growing up, Liam's favorite pastime was soccer, a sport that he still plays on a regular basis. In 2005, after returning to New Orleans after evacuating for Hurricane Katrina, Liam began to attend De La Salle High School where he graduated as the Valedictorian in 2010. After graduating from high school, he began to attend Tulane University where he majored in Biomedical Engineering and minored in Mathematics. Ultimately, Liam decided to stay at Tulane for an additional year in order to achieve a Master's degree. Liam has no set path for what he will be doing once he graduates and is excited for what the future has in store for him.